CHALMERS

Comparison of Methods for Evaluating Stability Performance of Power System Stabilizers

Master's Thesis in Electric Power Engineering

JOAKIM HIRAMSSON

Comparison of Methods for Evaluating Stability Performance of Power System Stabilizers

JOAKIM HIRAMSSON

Comparison of Methods for Evaluating Stability Performance of Power
System Stabilizers
JOAKIM HIRAMSSON

Cover: Block diagram implemented in Matlab/Simulink that models a single-machine
infinite bus system where the effects of field circuit dynamics, an excitation system,
and a power system stabilizer are included.

Comparison of Methods for Evaluating Stability Performance of Power
System Stabilizers

JOAKIM HIRAMSSON
Department of Energy and Environment
Chalmers University of Technology

Abstract

Two methods are commonly used by transmission system operators to evaluate the stability performance of a power system stabilizer (PSS). However, cases have been encountered where the two evaluation methods do not agree. This is problematic since it may affect the stability of the power system. In this study it is investigated and suggested which of two evaluation methods that is better to use when evaluating the stability performance of a PSS. This study is based on dynamic simulations of the Nordic32-system where PSS2Bs are placed at different synchronous machines that are located at different buses in the power system; then, the impact of tuning the PSS2Bs according to the two evaluation methods is analyzed by the traditional method of eigenvalue analysis. The eigenvalue analysis shows that tuning of the PSS2Bs according to the evaluation method used by Statnett results in higher increases in the damping ratios of the complex eigenvalues with imaginary parts in the range of 0.6 - 6.3 rad/s compared with tuning of the PSS2Bs according to the evaluation method used by National Grid. Therefore, for the specific cases simulated, it is suggested that the evaluation method used by Statnett is better to use for purposes of evaluating the stability performance of a PSS.

Acknowledgments

Contents

List of Figures

List of Tables

List of Symbols

The subscript 0 denotes initial values of a parameter. The prefix Δ denotes small deviations from an initial value.

ω_m	Mechanical angular frequency.
ω_e	Electrical angular frequency.
p	Number of stator poles.
F_f	Excitation MMF.
F_a	Armature reaction MMF.
F_δ	Air-gap MMF.
X_a	Armature reaction reactance.
R_a	Armature phase winding resistance.
X_l	Leakage reactance.
V_t	Terminal voltage.
E_f	Internal steady state voltage of the SM.
I	Line current.
X_d	Synchronous reactance.
δ_r	Power angle.
δ	Rotor angle relative to the terminal voltage angle of the SM.
t_r	Rise time.
t_s	Settling time.
λ	Eigenvalue.
σ	Real part of a complex eigenvalue.
ω	Complex part of a complex eigenvalue.
ξ	Damping ratio of a complex eigenvalue.
J	Moment of inertia of the rotor and all shaft components.
K_D	Damping factor.
T_m	Mechanical torque.
T_e	Electrical air-gap torque.
E_B	Infinite bus voltage.
θ_t	Terminal voltage angle relative to the infinite bus voltage angle.
X_E	Equivalent reactance of all reactances external to the SM.
P_e	Electrical air-gap power.
δ_t	Rotor angle relative to the infinite bus voltage angle.
P_m	Mechanical power.
T_S	Synchronizing torque component.
T_D	Damping torque component.

$G_W(s)$	Transfer function of the washout filter.
T_W	Time constant of the washout filter.
ω_W	Break angular frequencies of the washout filter.
$G_{ll}(s)$	Transfer function of the lead-lag filter.
$T_{ll1} - T_{ll2}$	Time constants of the lead-lag filter.
N	Filter order.
M_m	Angular momentum.
ω_{sm}	Synthesized mechanical rotor angular frequency.
K_{S1}	Gain of the PSS2B.
$T_{W1} - T_{W4}$	Time constants of the washout filters of the PSS2B.
$T_8 - T_9$	Time constants of the ramp tracking filter of the PSS2B.
M_R	Constant of the ramp tracking filter of the PSS2B.
N_R	Constant of the ramp tracking filter of the PSS2B.
T_6	Time constant of the transducer of the PSS2B.
T_7	Time constant of the integrator approximation of the PSS2B.
K_{S2}	Synthetization constant of the PSS2B.
K_{S3}	Synthetization constant of the PSS2B.
$T_1 - T_4$	Time constants of the lead-lag filters of the PSS2B.
$T_{10} - T_{11}$	Time constants of the lead-lag filter of the PSS2B.
V_{SMAX}	Upper output limit of the PSS2B.
V_{SMIN}	Lower output limit of the PSS2B.
E_f'	Transient internal voltage.
X_f	Field winding reactance.
X_d'	Transient reactance.
X_T	Equivalent reactance between the transient internal voltage of the SM and the infinite bus voltage.
K_S	Synchronizing torque component.
H	Inertia constant.
S_{base}	Rated apparent power of the SM.
ω_{m0}	Rated mechanical angular frequency of the SM.
ω_0	Rated electrical angular frequency of the SM.
K_1	Change in electrical torque per change in rotor angle.
K_2	Change in electrical torque per change in air-gap flux linkage.
K_3	Change in air-gap flux linkage per change in field voltage.
K_4	Change in field voltage per change in rotor angle.
T_{fd}	Time constant of the field circuit.
Ψ_{fd}	Air-gap flux linkage.
E_{fd}	Field voltage.
K_5	Change in terminal voltage per change in rotor angle.
K_6	Change in terminal voltage per change in air-gap flux linkage.
$G_{vt}(s)$	Transfer function of the voltage transducer.
T_R	Time constant of the voltage transducer.
e_t	Voltage error signal.
V_{ref}	Voltage reference.
v_l	Output of the voltage transducer.
$G_{bex}(s)$	Transfer function of the ST1A brushless exciter.
T_{bex}	Time constant of the ST1A brushless exciter.

K_P	Gain of the PID-regulator AVR.
T_i	Time constant of the integrator of the PID-regulator AVR.
T_d	Time constant of the differentiator of the PID-regulator AVR.
K_d	Constant of the differentiator of the PID-regulator AVR.
$G_{AVR}(s)$	Transfer function of the PID-regulator AVR.
$G_{ex}(s)$	Transfer function of the excitation system.
$G_{PSS}(s)$	Transfer function of the simplified PSS2B.
$T_{e,PSS}$	Electrical air-gap torque contribution from the simplified PSS2B.
R_B	Short-circuit resistance of the infinite bus.
X_B	Short-circuit reactance of the infinite bus.
R_L	Resistance of the transmission line.
X_L	Reactance of the transmission line.
X_k	Short-circuit reactance of the step-up transformer.
K_A	Gain of the PI-regulator AVR.
T_I	Time constant of the integrator of the PI-regulator AVR.
T_A	Time constant of the transient reduction filter.
$G_{ll1}(s) - G_{ll3}(s)$	Transfer functions of the lead-lag filters of the simplified PSS2B.
$G_{pc}(s)$	Transfer function of the phase compensation block of the simplified PSS2B.
$\omega_1 - \omega_{11}$	Break angular frequencies of the lead-lag filters of the simplified PSS2B.
$r_1 - r_3$	Ratios of the time constants of the lead-lag filters of the simplified PSS2B.

1

Introduction

The demands on power quality are constantly increasing, and power system stability is important in order to comply with defined power quality limits. Power system stability is also important for the sustainable development worldwide. The traditional usage of fossil fuels in power generation is causing concerns for the environment, the climate and for the health of people [1], [2]. Renewable energy sources (RES) is a clean way of reducing the need for fossil fuels in power generation [2], [3]. However, the combination of factors such as increasing power flows and an increasing usage of RES is expected to reduce the ability of the power system to withstand outages as well as increase its vulnerability [2]–[5].

Power system stability can be divided into three categories: voltage-, frequency-, and rotor angle stability [6]. Rotor angle stability deals with the study of electro-mechanical oscillations present in the power system, and it can be enhanced by actively regulating the terminal voltages of the synchronous machines (SMs) in the power system. Terminal voltage regulation capability is provided by an automatic voltage regulator (AVR), and regulation is accomplished by controlling the excitation of the SM [7]–[9]. In addition to the AVR, a power system stabilizer (PSS) is typically utilized to provide damping to the electro-mechanical oscillations [8], [10].

There are two methods commonly used by transmission system operators (TSOs) to evaluate the stability performance of a PSS. The first evaluation method is to measure the response characteristic from the PSS input to the terminal voltage of the SM. The obtained response shall be within certain limits in terms of amplitude and phase for a certain range of angular frequencies [11]. In the second evaluation method, the amplitude response characteristic from the AVR input to the active power output from the SM is measured with both disconnected and connected PSS. For the PSS to provide damping, the amplitude response with connected PSS needs to be equal to or smaller than the amplitude response with PSS disconnected for a specific range of angular frequencies [12].

Solvina has encountered different cases where PSSs perform within given limits when evaluated with one of the two evaluation methods; however, when the same PSSs are evaluated with the other evaluation method they do not perform within given limits. This indicates that the two evaluation methods do not agree. The possible disagreement between the two evaluation methods is problematic since it may infer that some PSSs currently connected to the power system are improperly tuned; thus, these PSSs may compromise the stability of the power system. This

has not been addressed in recent research where focus is on research areas such as: optimal location of the PSS [13], [14]; PSS design and tuning using nonlinear and/or artificial intelligence based control theories [13]–[19]; and pricing of PSS services [20], [21].

1.1   Aim

Investigate and suggest which of the two evaluation methods that is better to use when evaluating the stability performance of a PSS.

1.2   Objectives

The aim is broken down into two main objectives where the first objective is to gain understanding about how changes in the response of the first evaluation method are reflected in the amplitude response of the second evaluation method. The second objective is to evaluate the performance of a PSS when it is tuned according to each evaluation method. The second objective comprises three parts: 1) verify the findings of the first objective, 2) simulate a multi-bus power system with the PSS at different locations, and 3) analyze the stability performance of the PSS.

1.3   Method

The first objective is accomplished through Matlab/Simulink simulations of a linearized model of a single-machine infinite bus (SMIB) system. The second objective is accomplished through dynamic simulations in Simpow. The first part of the second objective comprises dynamic simulations of an SMIB-system. The second part of the second objective comprises dynamic simulations of a multi-bus power system. For each location of the PSS, it is tuned so that it performs well according to each of the two evaluation methods for two different sets of tunings; hence, four sets of dynamic simulations are performed for each PSS location. In the third part of the second objective, the stability performance of the PSS is analyzed by the traditional method of eigenvalue analysis [22].

1.4   Scope

This is an example study where focus is on investigating the performance of the two evaluation methods when the power system is subjected to small-signal disturbances. Rotor angle stability problems related to large-signal disturbances are not considered. Stability problems related to deviating power system frequency or deviating bus voltages are not considered either.

The linearized model of the SMIB-system is valid for small-signal disturbances around an initial operating point. The model includes the effects of: the field circuit dynamics, the excitation system, and the PSS. The model only captures a certain

mode of oscillation; therefore, the results are not generalizable to larger power systems where other modes of oscillation exist [23]. The PSS considered is a PSS2B and it is assumed that the rotor angular frequency deviation input signal perfectly represents the true rotor angular frequency deviation. Therefore, only the rotor angular frequency deviation is utilized as the input signal to the PSS. The excitation system comprises a brushless exciter and an AVR of PID-regulator type. The effects of turbine and governor are not modeled since they do not affect the dynamics. The model is deemed sufficient for investigating basic concepts even though it does not include the effects of damper windings [9], [23], [24]. Moreover, no saturation effects are included when calculating model parameters since saturation data is unavailable. This affects the stability limits of the SMIB-system somewhat; however, this is not deemed critical.

The dynamic simulations of the SMIB-system and the multi-bus power system utilize an SM-model that includes the effects of: the field winding, one d-axis damper winding, two q-axis damper windings, and magnetic saturation. In addition, a turbine and a governor are modeled; however, they do not affect the dynamics. The excitation system is modeled as a PI-regulator. The PSS is a PSS2B and utilizes rotor angular frequency deviation and electrical power deviation as input signals.

The SMIB-system only captures a certain mode of oscillation. However, the multi-bus power system capture the effects of additional oscillation modes. The dynamic simulations of the multi-bus power system and the following eigenvalue analysis therefore provide a general picture of the performance of the PSS. This can in turn be used for evaluating the performance of the two evaluation methods.

1.5   Outline

The outline of the report is as follows: Chapter 2 introduces the fundamental concepts of small-signal rotor angle stability. Chapters 3 and 4 follow with the modeling of the different power systems. Chapters 5 and 6 presents the results from the linearized and dynamic simulations whereas Chapter 7 discusses these findings in a somewhat wider perspective. Chapter 8 concludes.

2

Small-Signal Rotor Angle Stability

Small-signal rotor angle stability deals with the study of electro-mechanical oscillations caused by small disturbances on the power system, such as small continuous changes in load and generation [25]. This chapter introduces the fundamental concepts of small-signal rotor angle stability and starts with reviewing some SM fundamentals. The following section introduces the nature of small-signal rotor angle oscillations. The last section of the chapter introduces the PSS and elaborates on its different components.

2.1   The Synchronous Machine

This section first reviews the working principle of the SM. In the following section is the relationship between the rotor angle and the electrical air-gap power established with the help of the steady state equivalent circuit and its corresponding phasor diagram. This section concludes with reviewing the role of the excitation system.

Fig. 2.1 shows the topology of a two-pole round-rotor SM. The armature phase windings are represented by the coils aa', bb' and cc'. The field winding is located in the rotor and is represented by the coil ff' [7], [25].
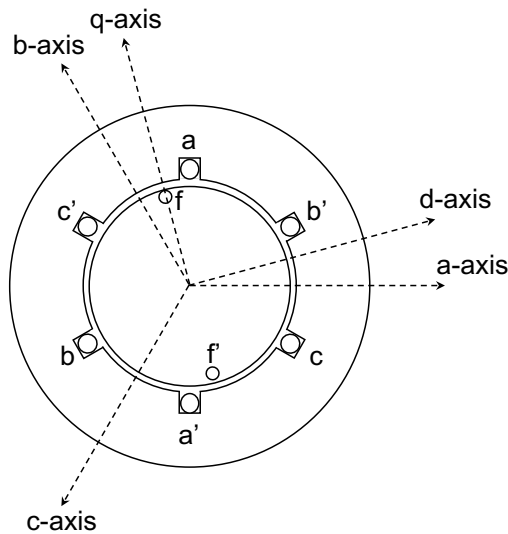
Fig. 2.1: Topology of a round-rotor SM.

In the figure, each of the armature phase windings has its own magnetic axis and these are the a-, b- and c-axes for the *aa′*, *bb′* and *cc′* coils, respectively. The magnetic axes that correspond to the armature phase windings are stationary since the armature phase windings are fixed in the stator. Furthermore, two magnetic axes are introduced for the field winding: the d-axis, and the q-axis. The q-axis leads the d-axis by 90 deg. The d- and q-axes comprise a rotating reference frame that rotates with the same mechanical angular frequency as the rotor and is equal to ω_m mechanical rad/s [26].

If the number of stator poles is larger than two, the mechanical angular frequency of the rotor does not equal the electrical angular frequency of the rotor. However, the angular frequency of the rotor can be converted from mechanical radians per second into electrical radians per second. The relation is:

$$\omega_e = \frac{p}{2}\omega_m \tag{2.1}$$

where ω_e is the electrical angular frequency and p is the number of stator poles [26].

2.1.1 Working Principle

The SM is excited by a direct current in the field winding that generates an excitation magneto-motive force (MMF) wave. The excitation MMF-wave is assumed to be sinusoidally distributed along the stator with its peak directed along the d-axis. Thus, the electrical angular frequency of the excitation MMF-wave is, after the possible conversion according to (2.1), equal to ω_e [26].

The armature phase currents generate an armature reaction MMF-wave, and it can be shown that the armature reaction MMF-wave is rotating with the same electrical angular frequency as the excitation MMF-wave [26, Ch. 3]. Thus, the excitation MMF-wave and armature reaction MMF-wave can be added together to form the resultant air-gap MMF-wave, which Fig. 2.2 illustrates [26].
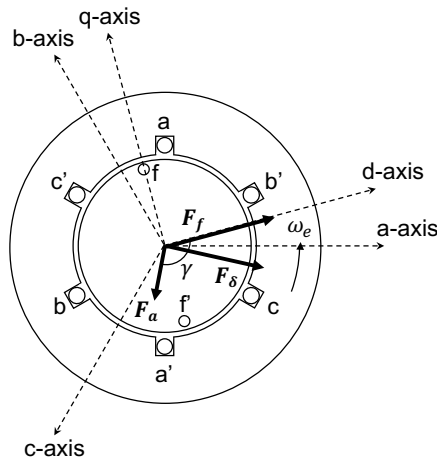
Fig. 2.2: The field MMF-wave ($\boldsymbol{F_f}$) and the armature reaction MMF-wave ($\boldsymbol{F_a}$) forms the resultant air-gap MMF-wave ($\boldsymbol{F_\delta}$).

2.1.2 Equivalent Circuit and Phasor Diagram

For purposes of steady state analysis, the SM is commonly represented by its equivalent circuit. The equivalent circuit of the SM in steady state is depicted in Fig. 2.3. In the figure, phasors are used to represent voltages and currents. In addition, the parameters of the SM, the voltages, and the line current are normalized and expressed in per unit [25].
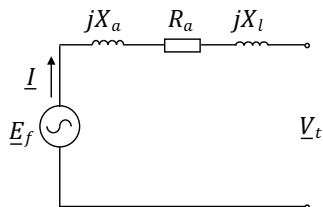
Fig. 2.3: Steady state equivalent circuit of the SM.

In the figure, X_a is the armature reaction reactance, R_a is the resistance of the armature phase winding, X_l is the leakage reactance, V_t is the terminal voltage, and E_f is the internal steady state voltage of the SM, and I is the line current [26]. The two reactances X_a and X_l are typically combined into a single reactance that is known as the synchronous reactance X_d [7].

Fig. 2.4 shows the phasor diagram of the SM that corresponds to the steady state equivalent circuit illustrated in Fig. 2.3 [7].
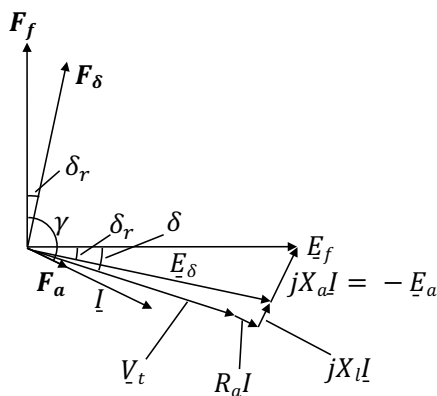
Fig. 2.4: Steady state phasor diagram of the SM.

In the figure, δ_r is known as the power angle of the SM since the electrical air-gap power generated by the SM is directly related to this angle [7]. The rotor angle is denoted δ, and in the figure it is the angle between the internal voltage and the terminal voltage. From the figure it can be seen that the rotor angle and the power angle are not equal. However, the leakage reactance is typically small in comparison to the armature reaction reactance and can therefore often be neglected. Consequently, it can be approximated that the rotor angle is equal to the power angle; hence, the electrical air-gap power generated by the SM can be expressed in terms of the rotor angle [7], [26].

2.1.3 The Excitation System

The main role of the excitation system is to generate the field current that provides excitation of the SM. By controlling the field current, the excitation system controls the voltage and reactive power flow from the SM. These are important control tasks from a power system stability perspective. Besides that, the excitation system also provides protective functions in order to avoid operation beyond the capability limits of the SM [25].

The excitation system consists of an exciter, a voltage transducer and an AVR. The role of the exciter is to provide the current to the field winding whereas the AVR provides the necessary control of the exciter. Fig. 2.5 presents the layout of a general excitation system that is connected to an SM where the protective functions of the excitation system are omitted [25].
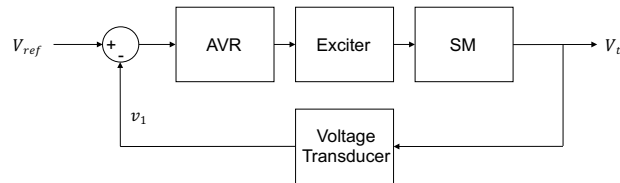
Fig. 2.5: General excitation system.

The input to the AVR is a voltage error signal. The voltage error signal is formed by comparing a voltage reference signal with a terminal voltage signal obtained via the voltage transducer. The AVR controls the output of the exciter block to be equal to the desired field voltage. This generates in turn the desired terminal voltage of the SM [27].

The small-signal performance of the excitation system is evaluated when the SM is in no-load. The performance evaluation is based on the response in the terminal voltage when a step in the voltage reference is applied. The relevant performance measures related to the step response are: rise time, settling time, and overshoot [28]. Table 2.1 shows the range of expected values inside which the step response performance measures are expected to be in order for the feedback control system to be considered good.

Table 2.1: Range of values of the excitation system performance measures, as defined in [28]

Performance Measure	Range of Values	Unit
Rise time (t_r)	0.025 - 2.5	s
Settling time (t_s)	0.2 - 10	s
Overshoot	0 - 40	%

2.2 Small-Signal Rotor Angle Oscillations

This section introduces the basics of small-signal rotor angle oscillations. First are the different types of oscillation modes introduced. The second, third, and fourth sections explain the tools of eigenvalue analysis, modal analysis, and participation factor analysis, respectively. The following section continues with reviewing the swing equation whereas the last section explains the central concepts of synchronizing and damping torques.

2.2.1 Modes of Oscillation

The interesting modes of oscillation are: local-, inter-plant-, inter-area-, torsional-, and control modes of oscillation [29], [30]. Local modes occur when SMs in one generating station oscillate against the rest of the power system. The angular frequencies of local modes are ranging from approximately 5 - 12.6 rad/s [31]. Inter-plant modes occur when SMs in the same plant oscillate against each other. The angular frequencies of the inter-plant modes are typically in the range of 9.4 - 15.7 rad/s [30]. Inter-area modes occur when SMs in one area of the power system oscillate against SMs in other areas of the power system. The angular frequencies of the inter-area modes are ranging from approximately 0.6 - 6.3 rad/s [30]. Torsional and control modes are associated with oscillations stemming from turbine shaft components and improperly tuned controllers that are located in the power system, respectively. The angular frequencies of torsional modes typically exceed 50.3 rad/s [10], [32].

2.2.2 Eigenvalue Analysis

The modes of oscillation and their influence on the stability of the power system can be investigated by expressing the power system on state-space form with the following calculation of the eigenvalues of the power system. An eigenvalue can be either real or complex conjugated, and the both types of eigenvalues give the damping of the modes that are associated with the eigenvalues. Complex eigenvalues also give the angular oscillating frequencies of the oscillation modes that are associated with the complex eigenvalues [25].

A real eigenvalue represents a mode with non-oscillatory behavior in the time domain. A certain mode i that is associated with a certain real eigenvalue λ_i has a time domain characteristic given by $exp[\lambda_i t]$. Therefore, in order for the mode to show a stable time domain characteristic it is necessary that the eigenvalue is negative; consequently, its time domain characteristic represents a decaying exponential function. The amplitude of the eigenvalue determines the quickness of the decay where an eigenvalue with large amplitude gives a quickly decaying mode, and vice versa [25].

A mode i with complex eigenvalue $\lambda_i = \sigma_i \pm j\omega_i$ is associated with an oscillatory time domain characteristic since its time domain characteristic is given by $exp[\sigma_i t] \cdot \sin(\omega_i t + \theta)$. The complex part of λ_i represents the angular oscillating

frequency whereas the real part represents the damping. To show a stable time domain characteristic the real part needs to be negative [25]. The damping ratio of the mode is

$$\xi_i = \frac{-\sigma_i}{\sqrt{(\sigma_i^2 + \omega_i^2)}} \tag{2.2}$$

where a large value of the damping ratio represents a quickly decaying mode [25].

2.2.3 Modal Analysis

For a complex eigenvalue, modal analysis gives information about the amplitude and phase of the contributions from the different SMs to the oscillation mode associated with the specific complex eigenvalue. However, the information about the amplitude can be misleading since the amplitude is dependent on the units of the state variables [25], [30]. Therefore, the modal analysis is only used to give an indication of the amplitude of the contributions from the different SMs to the oscillation mode.

2.2.4 Participation Factor Analysis

Due to the fact that the modal analysis can be misleading in terms of the amplitude of the contributions, it needs to be complemented by participation factor analysis. The participation factor analysis gives accurate information about to what extent the different SMs and their state variables are contributing to a certain oscillation mode [30]. Thus, by combining the modal analysis with the participation factor analysis, it can be established what type of oscillation mode a certain complex eigenvalue represents. It is also possible to decide whether the mode associated with the specific complex eigenvalue represents an electro-mechanical oscillation.

2.2.5 The Swing Equation

The effect of an imbalance between the mechanical driving torque, provided by the prime mover, and the breaking electrical air-gap torque generated by the SM is dictated by [25]:

$$J\frac{d\omega_m}{dt} = T_m - T_e - K_D\omega_m. \tag{2.3}$$

Where J is the moment of inertia of the rotor also including all devices connected to the rotor shaft, K_D is the damping factor, T_m and T_e are the mechanical and the electrical air-gap torques, respectively [25].

2.2.6 Synchronizing Torque and Damping Torque

Consider an SM that is connected to an infinite bus via a transformer and two parallel transmission lines in a simple SMIB-system configuration. Such an SMIB-system is depicted in Fig. 2.6. Phasors are used to represent steady state voltages as well as the line current. The infinite bus voltage E_B is taken as reference.
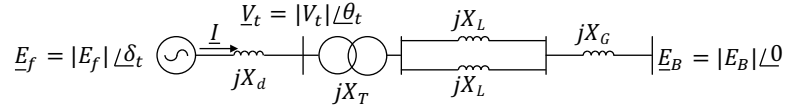
Fig. 2.6: SMIB-system considered for illustrating the synchronizing and the damping torque components.

In the figure, θ_t is the angle of the terminal voltage relative to the angle of the infinite bus voltage. The total equivalent reactance external to the SM is equal to X_E. The active electrical power transferred from the SM to the infinite bus in steady state is equal to the electrical air-gap power since there are no active power losses in the considered power system. The electrical air-gap power is

$$P_e = 3 \cdot \frac{|E_f| \cdot |E_B|}{X_E + X_d} \sin \delta_t \tag{2.4}$$

where δ_t is the rotor angle now expressed relative to the angle of the infinite bus voltage [30], [33]. The power-angle relationship given by (2.4) is represented by curve one in Fig. 2.7 where the peak of the electrical air-gap power occurs at $\delta_t = \pi/2$ rad and is equal to $P_{e,max}$. In steady state, the rotor angle is fixed at $\delta_t = \delta_{t,0}$ and the electrical air-gap power is equal to the mechanical power P_m.
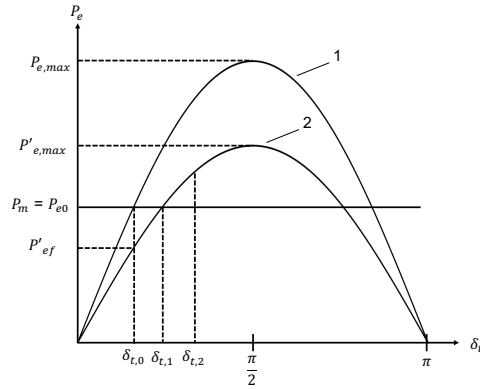
Fig. 2.7: Power-angle curves.

In a situation where the transferred electrical power is reduced there is a corresponding decrease in the electrical air-gap power of the SM. This can be seen in Fig 2.7 where a reduction in the electrical air-gap power is represented by curve two. Upon reduction of the transferred electrical power the rotor angle equals its initial value $\delta_{t,0}$ and the electrical air-gap power drops to P'_{ef}. However, the driving mechanical power supplied by the prime mover still remains at P_m. Hence, there is an imbalance between the mechanical power and the electrical air-gap power.

Due to the imbalance between the mechanical and the electrical air-gap powers, the rotor of the SM starts to accelerate. The rotor accelerates until the electrical air-gap power becomes equal to the mechanical power, which corresponds to a rotor angle equal to $\delta_{t,1}$. At this point, the rotor starts to decelerate. However, the rotor angle is still increasing until the rotor angle reaches $\delta_{t,2}$ where it starts to decrease.

The rotor angle decreases until it gets close to its original value $\delta_{t,0}$, where it again starts to increase. The rotor angle continues to oscillate in this way until it finally settles at a new value $\delta_{t,1}$ where the electrical air-gap power equals the mechanical power [30].

A deviation in rotor angle away from its initial value results in a change in the electrical air-gap power and is also associated with a change in the electrical air-gap torque. The change in electrical air-gap torque can be expressed as the sum of two components, as follows [25]:

$$\Delta T_e = T_S \Delta \delta_t + T_D \Delta \omega_e. \tag{2.5}$$

Where T_s is the synchronizing torque component and T_D is the damping torque component [25]. The two terms $T_S \Delta \delta_t$ and $T_D \Delta \omega$ in (2.5) show that the synchronizing and damping torque components each generates an electrical air-gap torque component in phase with the deviations in rotor angle and rotor angular frequency, respectively [25], [34].

Both the synchronizing and the damping torque components are important from a small-signal rotor angle stability perspective. The electrical air-gap torque component that is generated in phase with the rotor angle deviation maintains the synchronism of the SM; thus, aperiodic drift in the rotor angle can be avoided [30], [35]. However, with only synchronizing torque present, small-signal rotor angle stability problems may arise due to rotor angle oscillations with increasing amplitude. Thus, for the rotor angle to end up at a new operating value there is a need to generate sufficient damping torque in addition to the synchronizing torque. Synchronizing torque is generated by the AVR and damping torque is generated by the PSS. Small-signal rotor angle stability problems are typically caused by the lack of damping torque [8], [25], [32].

The quickness of the excitation system affects both the synchronizing and the damping torque components. During operating conditions where the output power from the SM is high, the effects of increasing the quickness of the excitation system is to increase the synchronizing torque component whereas the damping torque component is reduced. During operating conditions where the output power from the SM is low, the effects of increasing the excitation system quickness are the opposite in terms of changes in the synchronizing and the damping torque components [25].

2.3 The Power System Stabilizer

This section starts with the introduction of a general PSS structure where the individual blocks that comprise the general PSS structure are explained. The first section also elaborates on the functionality of these blocks. The following section gives a brief overview over the different PSS models defined by IEEE. The last section introduces the two evaluation methods.

The main objective of the PSS is to add damping to local and interarea modes of oscillation; however, at the same time, the PSS should not reduce damping of other oscillation modes present in the power system [31]. The PSS is part of the excitation system as illustrated in Fig. 2.8 where the output from the PSS is normally added to the voltage reference signal that is fed as an input to the AVR [25]; thus, this configuration allows for generating the damping torque component by additional excitation control [36].
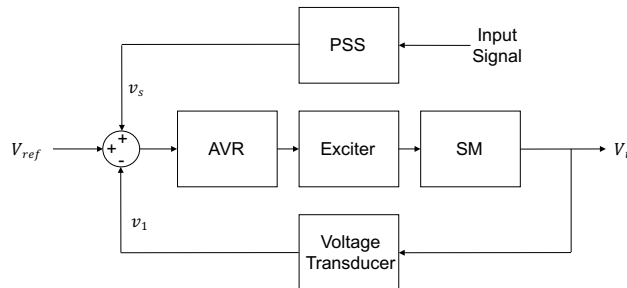
Fig. 2.8: General excitation system also including the PSS.

2.3.1 Representation of a General Power System Stabilizer

If the response characteristic from the AVR input to the electrical air-gap torque exhibits a pure gain characteristic, then the rotor angular frequency deviation can be used directly to generate the damping torque component. However, the PSS needs to provide a certain amount of phase lead compensation since the response characteristic from the AVR input to the electrical air-gap torque does not show pure gain characteristic; rather, the response characteristic from the AVR input to the electrical air-gap torque shows a phase lagging characteristic. The phase compensation needs to be provided over a certain range of angular frequencies. It should also be pointed out that the phase characteristic from the AVR input to the electrical air-gap torque changes as the operating condition changes [24], [25], [37].

Based on the previously described functions provided by the PSS, it is possible to construct a general PSS structure. The general PSS structure is illustrated in Fig. 2.9 [25], [26], [38] where it should be recognized that different PSS models relies on different input signals in order to generate its stabilizing signal. The different PSS models that are available realize this PSS structure in different ways.
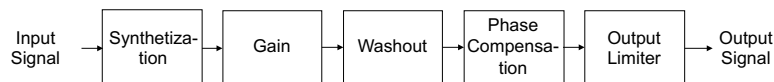
Fig. 2.9: General PSS structure.

The figure illustrates that the structure of any PSS can be considered to consist of a series of blocks, namely: a synthetization block, a gain block, a washout block, a phase compensation block, and an output limiter block. The rest of this section explains the functionality of each of the different blocks that comprise this general PSS structure.

Synthetization Block

The synthetization block generates the stabilizing signal based on one or multiple input signals.

Gain Block

The gain block consists of a gain, and it determines the amount of damping provided by the PSS [25].

Washout Block

The washout block consists of one or several washout filters, and the washout block provides filtering of dc components present in the input signal whereas components of higher angular frequency are passed [39]. Without the presence of the washout filter in the PSS, the terminal voltage would be affected by steady increases in the rotor angular frequency [37].

The transfer function of a single general washout filter is

$$G_W(s) = \left(\frac{T_W s}{1 + T_W s} \right)^N \tag{2.6}$$

where the washout filter is characterized by the time constant T_W and N denotes the order of the filter [25], [30]. Fig. 2.10 shows the response of a first-order washout filter for different values of the time constant. The values of the time constant are typical for PSS applications [25].
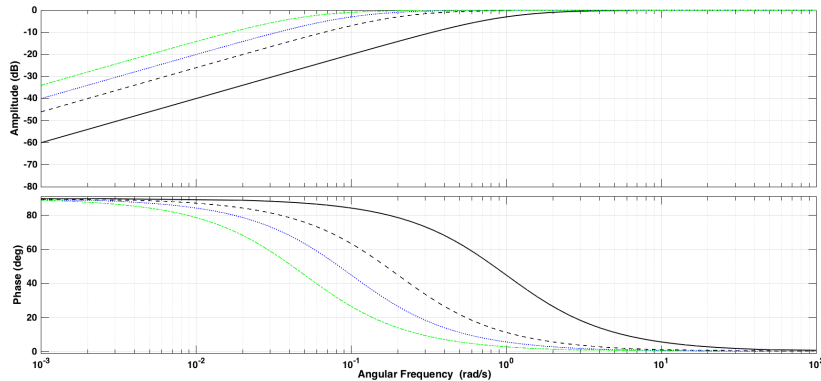
Fig. 2.10: Response of the washout filter with varying time constant. Solid: $T_W = 1$ s, dashed: $T_W = 5$ s, blue dotted: $T_W = 10$ s, and green dash-dotted: $T_W = 20$ s.

From the figure, it is clear that the washout filter attenuates angular frequencies up to the break angular frequency, which is approximately given by $\omega_W = 1/T_W$ rad/s. The washout filter generates phase lead compensation equal to 90 deg for angular frequencies below approximately $\omega_W/10$ rad/s. The phase lead decreases and equals zero at an angular frequency equal to approximately $10\omega_W$ rad/s [40]. The figure also shows how variations in T_W shift the response along the x-axis.

Fig. 2.11 illustrates the effects of varying the order of the washout filter in terms of the response of the washout filter.
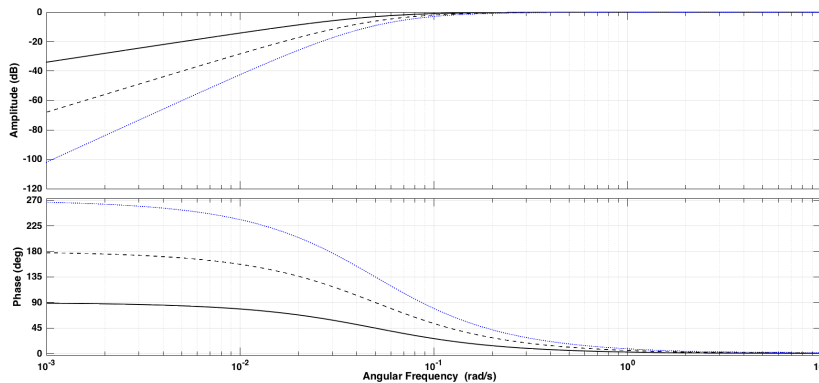
Fig. 2.11: Response of the washout filter with varying filter order. Solid: $N = 1$, dashed: $N = 2$, and blue dotted: $N = 3$.

As can be seen in the figure, increasing the order of the washout filter increases the slope of the amplitude characteristic. The slope of the amplitude characteristic is equal to $N \cdot 20$ dB/decade in the linear region. Increasing the order of the washout filter also increases the phase lead compensation provided at low angular frequencies. The phase lead compensation provided by the washout filter at low angular frequencies is equal to $N \cdot 90$ deg.

Phase Compensation Block
The fourth block in Fig. 2.9 is the phase compensation block. The phase compensation block consists of one or several lead-lag filters where the time constants of the lead-lag filters can be set independently. This flexibility allows for tuning the different parts of the response of the phase compensation block independently. This freedom is used in order to provide the desired amplitude and phase characteristics of the response of the PSS.

The transfer function of a single general lead-lag filter is

$$G_{ll}(s) = \left(\frac{1 + T_{ll1}s}{1 + T_{ll2}s} \right)^{N} \tag{2.7}$$

where T_{ll1} and T_{ll2} are the time constants of the filter and N denotes the order of the filter [24], [27].

Fig. 2.12 shows the response of a first-order lead-lag filter that provides phase lead compensation.

15
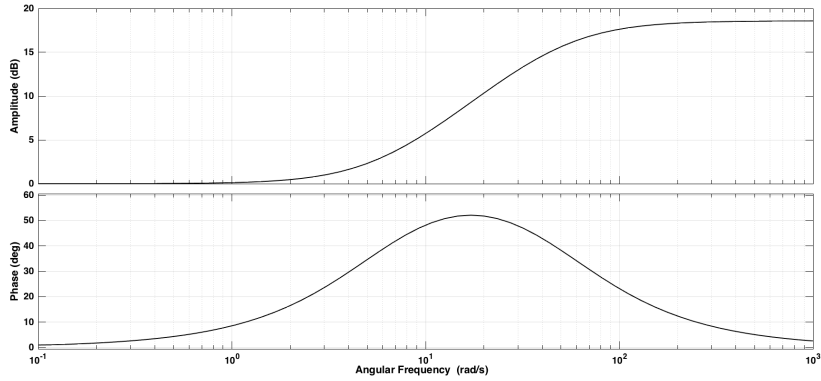
Fig. 2.12: Response of the lead-lag filter with $T_{ll1} = 0.17$ s and $T_{ll2} = 0.02$ s.

It is illustrated that phase lead compensation is provided when T_{ll1} is larger than T_{ll2} since the break angular frequency associated with the zero is lower than the break angular frequency associated with the pole. On the other hand, phase lag compensation can be provided when T_{ll1} is smaller than T_{ll2}; consequently, making the break angular frequency associated with the pole smaller than the break angular frequency associated with the zero [40], [41]. In the case of phase lag compensation, both amplitude and phase characteristics are mirrored around the x-axis.

Fig. 2.13 illustrates the effects of varying the ratio of T_{ll1} to T_{ll2} when the lead-lag filter provides phase lead compensation.
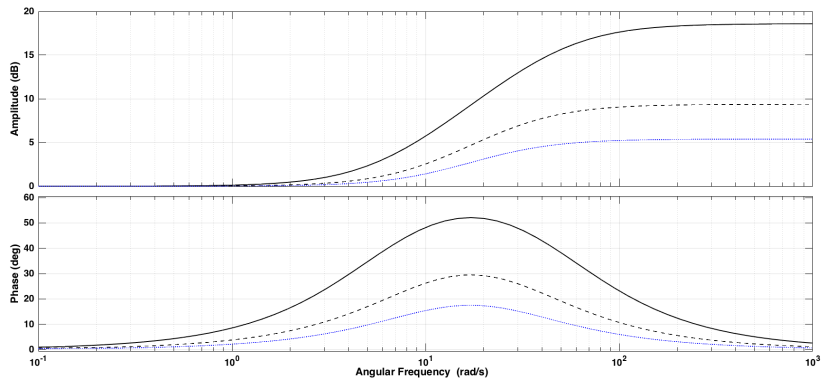
Fig. 2.13: Response of the lead-lag filter with varying ratio of T_{ll1} to T_{ll2}. Solid: $T_{ll1}/T_{ll2} = 8.5$; dashed: $T_{ll1}/T_{ll2} = 2.94$; and blue dotted: $T_{ll1}/T_{ll2} = 1.86$.

From the figure, it is clear that the amplitude characteristic decreases as the ratio of T_{ll1} to T_{ll2} decreases. In addition, decreasing the ratio of T_{ll1} to T_{ll2} decreases both the height and the width of the phase characteristic. Furthermore, a given response can be shifted along the x-axis by changing the values of T_{ll1} and T_{ll2} but keeping the ratio of T_{ll1} to T_{ll2} constant. The effect of varying the ratio of T_{ll2} to T_{ll1} are similar for a lead-lag filter that provides phase lag compensation.

Fig. 2.14 illustrates the effects of increasing the order of the lead-lag filter. It is shown that increasing the filter order increases the amplitude characteristic, and increasing the filter order also increases the height and width of the phase characteristic. The effects are the similar for a lead-lag filter that provides phase lag compensation.
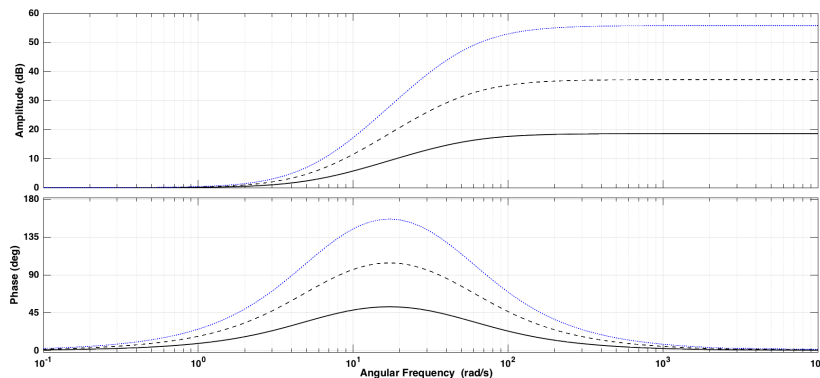
Fig. 2.14: Response of the lead-lag filter with varying filter order. Solid: $N = 1$, dashed: $N = 2$, and blue dotted: $N = 3$.

Output Limiter Block
The last block in Fig. 2.9 consists of a limiter that keeps the output from the PSS within certain limits. This block is needed in order to avoid large fluctuations in the terminal voltage during the transient state [31].

2.3.2   IEEE Power System Stabilizer Model Definitions

This section provides a brief overview of the different IEEE PSS model definitions. The section focuses especially on the basis on which each PSS model generates its stabilizing signal.

PSS1A Model
The PSS1A model utilizes a single input signal that typically is rotor angular frequency. This signal is easy accessible and represents the easiest way of generating the electrical air-gap torque component in phase with the rotor angular frequency deviation [27]. On the other hand, the deviation in rotor angular frequency is to a large extent reflected in the frequency of the terminal voltage; therefore, the PSS1A model can also utilize the terminal voltage frequency as the input signal [30].

Measuring the deviation in electric power is a third way of obtaining the stabilizing signal. Rewriting (2.3), neglecting damping effects and with the following linearization of the resulting equation yields

$$M_m \frac{d\Delta\omega_{sm}}{dt} = \Delta P_m - \Delta P_e \tag{2.8}$$

17

where M_m is the angular momentum and ω_{sm} is a synthesized mechanical rotor angular frequency signal that is used as the stabilizing signal. The synthesized mechanical rotor angular frequency deviation signal can be obtained from (2.8) by considering the deviation in mechanical power to be zero. Hence, integration of (2.8) yields the stabilizing signal [30]:

$$\Delta\omega_{sm} = -\frac{1}{M_m}\int \Delta P_e. \tag{2.9}$$

The drawback of the PSS1A is related to its input signal. The PSS1A that utilizes the rotor angular frequency or the frequency of the terminal voltage as input signal may be affected by torsional oscillations. In terms of the PSS1A that is based on generating a stabilizing signal through the deviation in electrical power, from (2.9) it can be seen that a non-zero deviation in mechanical power will affect the stabilizing signal since it is assumed that the deviation in mechanical power is zero [10].

PSS2B Model

The PSS2B model utilizes two input signals in order to generate a synthesized signal that represents mechanical rotor angular frequency deviation, and this signal is used as stabilizing signal. The generation of this signal can be based on a wide selection of input signals: the rotor angular frequency deviation, the terminal voltage frequency, the electrical power deviation, the accelerating power of SM, the terminal voltage of the SM, and the derivative of the terminal voltage of the SM [42].

A detailed sketch of a PSS2B that utilizes rotor angular frequency deviation and electrical power deviation as input signals is provided in Fig. 2.15 [38].
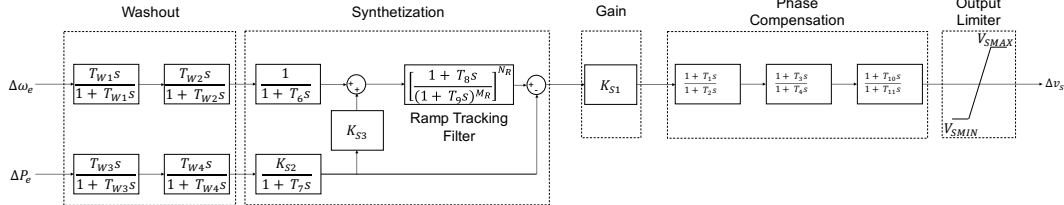
Fig. 2.15: Detailed sketch of a PSS2B.

In the figure it is possible to identify each of the blocks introduced in Fig. 2.9. The gain of the PSS2B is given by the constant K_{S1}. There are two washout filters associated with each of the two input signals, and the washout filters are characterized by the time constants T_{W1} - T_{W4}.

The synthetization block comprises a ramp tracking filter, a transducer filter and an integrator. The ramp tracking filter is characterized by the time constants T_8 and T_9 as well as the constants M_R and N_R. The ramp tracking filter is basically a low-pass filter that filters out torsional oscillation components in its input signal, and the ramp tracking filter should generate zero steady state error when its input signal is a ramp signal [42], [43]. The transducer filter is characterized by the time constant T_6 and the integrator is approximated by the low-pass filter with time constant T_7.

The two constants K_{S2} and K_{S3} govern the contribution from each of the two input signals. For more information on the procedure of generating the synthesized mechanical rotor angular frequency deviation signal, the reader is referred to [30, Ch. 8],[42].

The phase compensation block consists of three lead-lag filters that are characterized by the time constants T_1 - T_4 and T_{10} - T_{11}. The output limiter is a voltage limiter that keeps the output voltage within V_{SMAX} and V_{SMIN}.

PSS3B Model
The PSS3B model utilize two input signals, namely: the rotor angular frequency deviation and the electrical power. The two input signals are used to obtain an equivalent mechanical power signal. The obtained equivalent mechanical power signal is used in combination with the electrical power signal to generate a signal that represents the accelerating power of the SM that is used as stabilizing signal [38].

PSS4B Model
The PSS4B model is based on two input signals that generate two stabilizing signals. The input signals are the rotor angular frequency deviation and the electrical power deviation. The first stabilizing signal is obtained by the appropriate filtering of the rotor angular frequency signal, and it is fed to both a low-frequency band and a medium-frequency band. The electrical power deviation input signal is used to generate a synthesized rotor angular frequency signal comprising its high-frequency components. This synthesized signal is the second stabilizing signal and is fed to a high-frequency band. The outputs from the low-, medium-, and high-frequency bands are then summed into a signal that forms the output of the PSS4B.

The low-, medium-, and high-frequency bands are tuned in order to provide damping to oscillation modes with low-, medium-, and high oscillating angular frequencies, respectively. Thus, the advantage of the PSS4B compared with previous PSS models is that it provides damping over a larger range of angular oscillating frequencies [27], [38], [44].

2.3.3   Evaluation Methods for Power System Stabilizers

This section introduces the two evaluation methods commonly used by TSOs for purposes of evaluating the performance of PSSs. For each evaluation method, the section presents the measurement points utilized to obtain the response. The conditions that needs to be satisfied in order for the PSS to be considered properly tuned according to each evaluation method are also presented.

First Evaluation Method
Fig. 2.16 shows the measurement points of the first evaluation method where the response is taken from the PSS input to the terminal voltage of the SM. The response is obtained when the SM is in offline operation. This means that it is in no-load operation as well as disconnected from the grid [11].
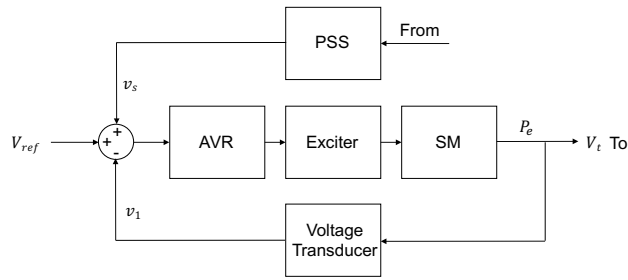
Fig. 2.16: Measurement points of the first evaluation method.

The obtained response is evaluated in terms of some predefined amplitude and phase limits. Fig. 2.17 illustrates both present and proposed limits as used by the Norwegian TSO Statnett. The limits in the figure are presented in [11] and from now on, the first evaluation method is referred to as the FIKS-method. It should be pointed out that other TSOs may use other limits that are not considered.
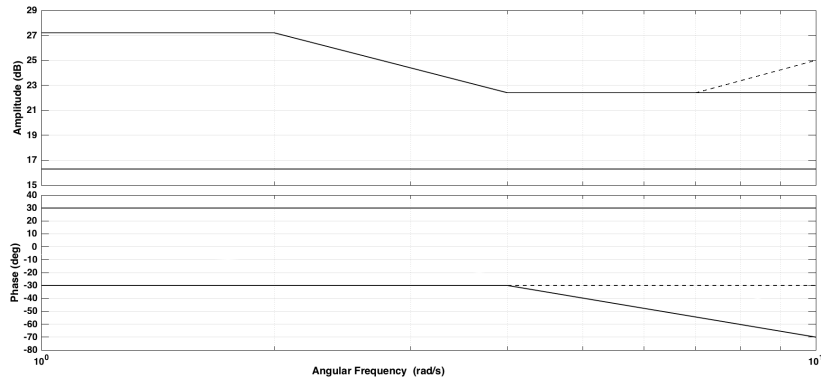
Fig. 2.17: Amplitude and phase limits of the FIKS-method. Solid: present limits and dashed: proposed limits.

Second Evaluation Method

The second evaluation method considers the amplitude response from the voltage reference to the electrical air-gap power output from the SM [12]. The measurement points are illustrated in Fig. 2.18.
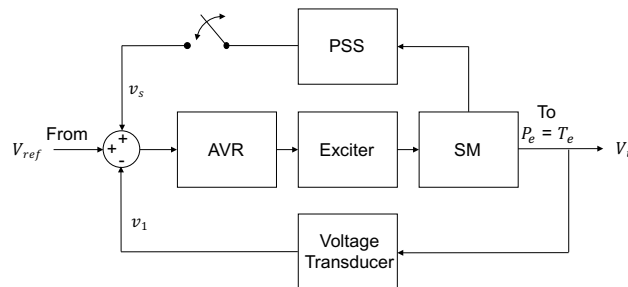
Fig. 2.18: Measurement points of the second evaluation method.

The figure shows that the amplitude response is obtained with PSS both connected and disconnected [12]. The figure also illustrates that the electrical air-gap torque is utilized as the output point instead of the electrical air-gap power. This is possible if normalization according to the per unit system is used since per unit torque and per unit power are numerically equal [25].

For the PSS to be properly tuned according to the second evaluation method, the amplitude response obtained with PSS connected needs to be lower than or equal to the amplitude response obtained with PSS disconnected. In the evaluation of the amplitude responses, the British TSO National Grid considers angular frequencies ranging between 1.26 - 18.85 rad/s [12]. From now on, the second evaluation method is referred to as the NG-method. Fig. 2.19 provides an example where the PSS is properly tuned and one example where the PSS is improperly tuned when it is evaluated with the NG-method.
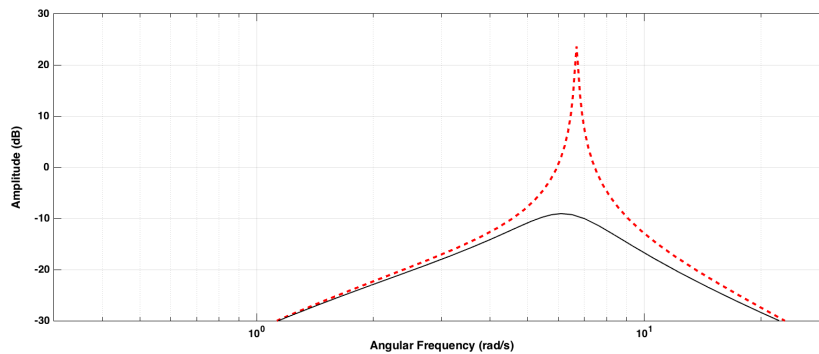
(a)
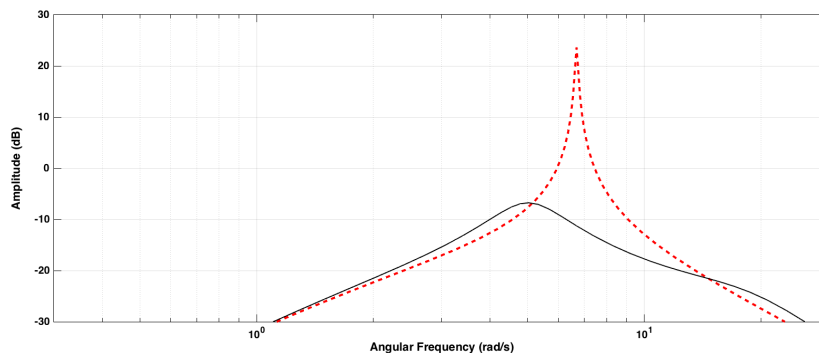
(b)

Fig. 2.19: Example responses obtained by the NG-method. Solid: PSS connected and red dashed: PSS disconnected. *(a)* Properly tuned PSS. *(b)* Improperly tuned PSS.

3

Modeling of Linearized Power System

This chapter first introduces the SMIB-system considered in the first objective, and this is followed by the modeling and implementation of this SMIB-system into Matlab/Simulink by the use of the classical model. The classical model is extended in the second section to account for the effect of field circuit dynamics. The third and fourth sections extend the model further to account for the effects of an excitation system and a PSS, respectively.

3.1 The Single-Machine Infinite Bus System

The power system comprises an SM that is operating towards an infinite bus via a transmission line. The SM is generating 0.695 p.u. of active power and 0.1745 p.u. of reactive power. The power system frequency is 50 Hz, and the SMIB-system is illustrated in Fig. 3.1.

$P_e = 0.695\,p.u.$
$Q_e = 0.1745\,p.u.$

Bus 1   Bus 2

I

jX_E
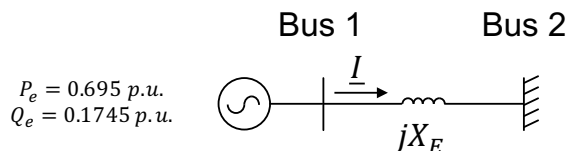
Fig. 3.1: SMIB-system considered in the first objective.

The SMIB-system is set up to be similar to the SMIB-systems considered in [25, Fig. E12.6] and in [10]. In cases where needed SM parameters are missing, standard values are assumed based on [35, Table 2.2]. Complete lists of values of the parameters are provided in Tables A.1 and A.2 in Appendix A.

3.2 The Classical Model

For purposes of small-signal analysis of the SMIB-system, the SM is represented by its transient model that is depicted in Fig. 3.2. The transient SM-model assumes constant d-axis flux linkages [23], [25].
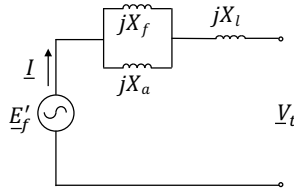
Fig. 3.2: Transient SM-model.

In the figure, E_f' is the internal transient voltage and X_f is the field winding reactance [6], [25]. The equivalent reactance of X_f, X_a and X_l gives the transient reactance and is expressed as follows [6]:

$$X_d' = X_l + \frac{1}{\frac{1}{X_a} + \frac{1}{X_f}} \tag{3.1}$$

Replacing the SM in Fig. 3.2 with its transient model yields the model of the SMIB-system that is depicted in Fig. 3.3. The infinite bus voltage is taken as reference and the rotor angle δ_t is expressed relative to the infinite bus voltage angle.
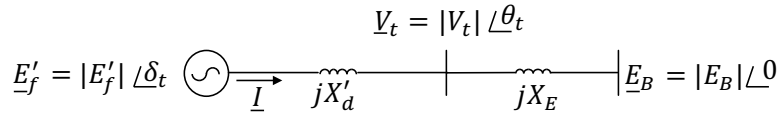
Fig. 3.3: Model of the SMIB-system considered in the first objective.

Introducing $X_T = X_d' + X_E$ as the total reactance between the internal transient voltage and the infinite bus voltage in Fig. 3.3; subsequently, the per unit electrical air-gap power supplied by the SM is [25]:

$$P_e = \frac{|E_f'| \cdot |E_B|}{X_T} \sin(\delta_t). \tag{3.2}$$

Eq. (3.2) also gives the per unit electrical air-gap torque since the per unit electrical air gap torque is numerically equal to the per unit electrical air-gap power. Linearization of (3.2) around an initial operating point $\delta_{t,0}$ yields

$$\Delta T_e = \frac{|E_f'| \cdot |E_B|}{X_T} \cos(\delta_{t,0}) \cdot \Delta \delta_t \tag{3.3}$$

where (3.3) represents an electrical air-gap torque component in phase with the rotor angle deviation [25]. According to (2.5), (3.3) can be expressed in terms of a synchronizing torque component K_S as follows [25]:

$$\Delta T_e = K_S \Delta \delta_t. \tag{3.4}$$

The effect of an imbalance between the driving mechanical torque and the breaking electrical air-gap torque is given by (2.3). For purposes of small-signal rotor angle stability studies, (2.3) is expressed in per unit and linearized, yielding

$$2H\frac{d\Delta\omega_e}{dt} = \Delta T_m - \Delta T_e - K_D\Delta\omega_e \tag{3.5}$$

where H is the per unit inertia constant. The per unit inertia constant is given by

$$H = \frac{1}{2}\frac{J \cdot \omega_{m0}^2}{S_{base}} \tag{3.6}$$

where S_{base} is the volt-ampere rating of the SM and ω_{m0} is the rated mechanical angular frequency of the SM [25].

The per unit deviation in electrical angular frequency is

$$\Delta\omega_e = \frac{1}{\omega_0} \cdot \frac{\Delta d\delta_t}{dt} \tag{3.7}$$

where ω_0 is the rated electrical angular frequency of the SM [25]. Substituting (3.4) and (3.7) into (3.5) and taking the Laplace transform of the resulting equation by assuming all initial conditions to be zero yields [25]:

$$\Delta\delta_t = \frac{\omega_0}{s}\left[\frac{1}{2Hs}\Big(\Delta T_m - K_S\Delta\delta_t - K_D\Delta\omega_e\Big)\right]. \tag{3.8}$$

Eq. (3.8) describes the small-signal behavior of the SMIB-system defined in Fig. 3.1 when the SM is modeled by its transient model. Fig. 3.4 shows the block diagram that represents (3.8) [25].
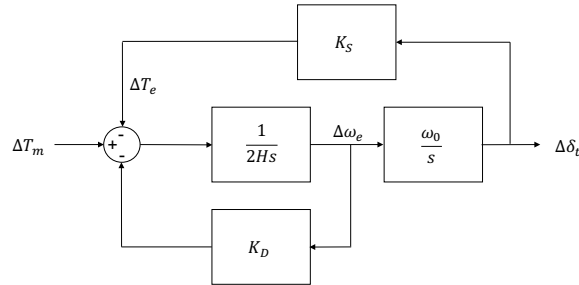
Fig. 3.4: Block diagram of the model of the SMIB-system considered in the first objective.

Table 3.1 gives the values of the parameters of the block diagram in Fig. 3.4. The values of the parameters are used when implementing the model into Matlab/Simulink.

Table 3.1: Values of the parameters of the block diagram in Fig. 3.4

Parameter	Value	Unit
ω_0	314.159	electrical rad/s
H	2.600	(MW $\cdot$ s)/MVA
K_S	0.872	p.u. torque/dev. elect. rad
K_D	0.000	p.u. torque/p.u. dev. ang. freq.

3.3 Including Field Circuit Dynamics

The field circuit dynamics cause variations in the flux linkage [23]. Fig. 3.4 is therefore modified by introducing a field circuit block as is shown in Fig. 3.5 [25].
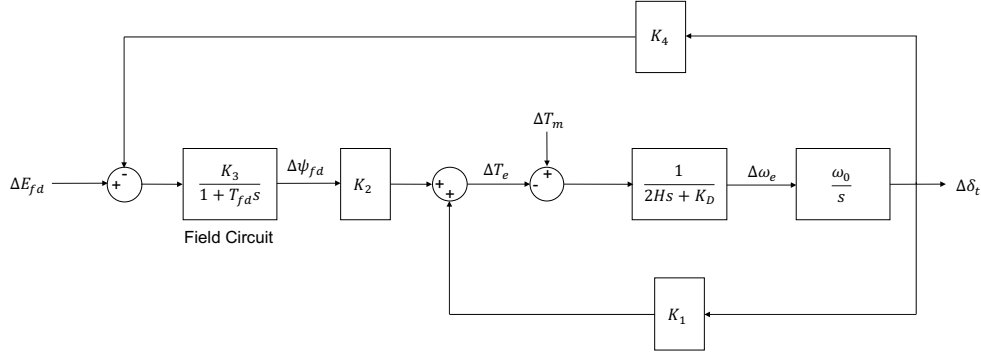
Fig. 3.5: Block diagram of the model of the SMIB-system also including the field circuit dynamics.

In the figure, the coefficient K_1 gives the change in electrical air-gap torque per change in rotor angle and K_2 gives the change in electrical air-gap torque per change in air-gap flux linkage. The coefficient K_3 gives the change in air-gap flux linkage per change in field voltage and the coefficient K_4 gives the change in equivalent field voltage per change in rotor angle [34]. T_{fd} is the field circuit time constant [23].

The coefficients $K_1, \ldots, K_4$ and the field circuit time constant T_{fd} are dependent on the operating condition of the SMIB-system and the parameter values of the SM [23]. The values of the coefficients and the time constant are provided in Table 3.2, and the procedure of calculating them is presented in Appendix B.

Table 3.2: Values of the coefficients $K_1, \ldots, K_4$ and the field circuit time constant T_{fd}

Parameter	Value	Unit
K_1	0.752	p.u. torque/p.u. rot. ang.
K_2	0.769	p.u. torque/p.u. air-gap flux link.
K_3	0.610	p.u. air-gap flux link./p.u. field volt.
K_4	0.734	p.u. field volt./p.u. rot. ang.
T_{fd}	4.267	s

From Fig. 3.5, the change in electrical air-gap torque can be expressed as

$$\Delta T_e = K_1 \Delta \delta_t + K_2 \Delta \Psi_{fd} \tag{3.9}$$

where Ψ_{fd} is the air-gap flux linkage [45]. The change in air-gap flux linkage is given by

$$\Delta \Psi_{fd} = \frac{K_3}{1 + T_{fd}s}(\Delta E_{fd} - K_4 \Delta \delta) \tag{3.10}$$

where E_{fd} is the field voltage [23]. Assuming manual control puts ΔE_{fd} in (3.10) equal to zero and allows for expressing (3.9) in terms of the change in the rotor angle, as follows [25]:

$$\Delta T_e = K_1 \Delta \delta_t - \frac{K_2 K_3 K_4}{1 + T_{fd}s} \Delta \delta_t. \tag{3.11}$$

In (3.11), the part of the change in electrical air-gap torque due to the change in the rotor angle that is fed back through the coefficient K_4 represents demagnetization of the SM due to armature reaction [25].

Eq. (3.11) can be simplified by substituting $s = j\omega_e$. Furthermore, assuming that the angular oscillating frequency is higher than $1/T_{fd}$ yields

$$\Delta T_e = K_1 \Delta \delta_t + \frac{K_2 K_3 K_4}{T_{fd}\omega_e} j \Delta \delta_t \tag{3.12}$$

and is on the form introduced by (2.5) since $j\Delta \delta_t = \Delta \omega_e$ [25]. The angular oscillating frequency of the local mode is 6.28 rad/s. Thus, (3.12) is reduced to:

$$\Delta T_e = 0.7565 \Delta \delta_t + 0.0128 \Delta \omega_e. \tag{3.13}$$

From (3.12) it can be recognized that the effect of accounting for the field circuit dynamics is to introduce a positive damping torque component as long as $K_2 K_3 K_4$ is positive.

3.4 Including Excitation System

The excitation system is included into the model in Fig. 3.1 by introducing the blocks of the exciter, AVR, and the voltage transducer as is shown in Fig. 3.6. In addition, the coefficients K_5 and K_6 are added to provide the necessary relations between the excitation system and the rest of the model [23], [25].
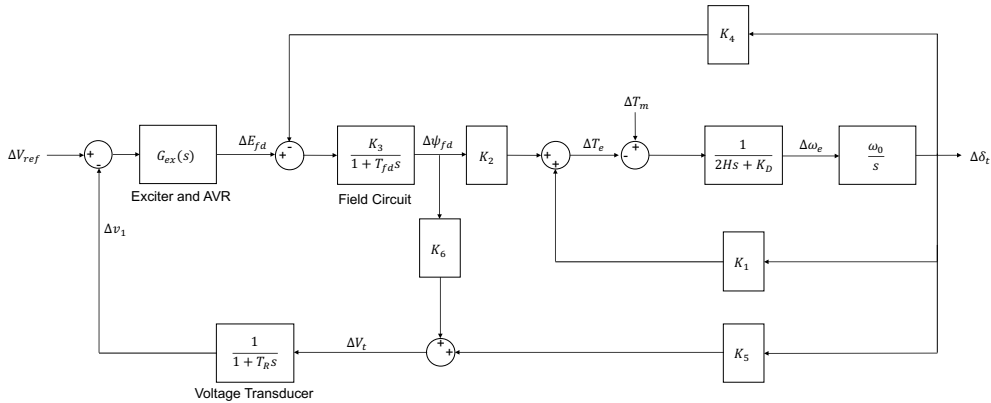
Fig. 3.6: Block diagram of the model of the SMIB-system also including the excitation system.

The coefficients K_5 and K_6 gives the change in terminal voltage per change in rotor angle and the change in terminal voltage per change in air-gap flux linkage, respectively [34]. As for the coefficients $K_1, \ldots, K_4$ and the field cirucit time constant, the values of the coefficients K_5 and K_6 are dependent on the operating condition of the SMIB-system as well as the parameter values of the SM. The values of the coefficients are calculated according to the procedure presented in Appendix B, and the values of the coefficients are provided in Table 3.3.

Table 3.3: Values of the coefficients K_5 and K_6

Parameter	Value	Unit
K_5	-0.070	p.u. term. volt./p.u. rot. ang.
K_6	0.510	p.u. term. volt./p.u. air-gap flux link.

The voltage transducer in Fig. 3.6 senses and filters the terminal voltage signal [25]. The transfer function of the voltage transducer is

$$G_{vt}(s) = \frac{1}{1 + T_R s} \tag{3.14}$$

where T_R is the voltage transducer time constant, and it is set to 0.02 s, which is a typical value [25].

Fig. 3.7 shows the exciter and AVR block introduced in Fig. 3.6, and it comprises a brushless exciter and a PID-regulator AVR. The input is the error signal formed by $\Delta e_t = \Delta V_{ref} - \Delta v_l$ where V_{ref} is the voltage reference and v_l is the output from the voltage transducer.
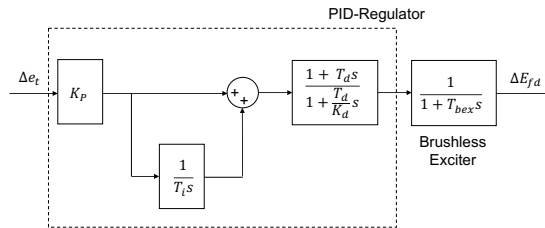
Fig. 3.7: Block diagram of the exciter and PID-regulator AVR.

Similar to [10], a brushless exciter of type ST1A [38] is implemented. The transfer function of the brushless exciter is

$$G_{bex}(s) = \frac{1}{1 + T_{bex} s} \tag{3.15}$$

where T_{bex} is the brushless exciter time constant and is set to 0.3 s [10].

The AVR consists of three blocks: a gain block with gain K_P; an integrator block with integrator time constant T_i; and a differentiator block with differentiator time constant T_d and differentiator constant K_d [10]. From the block diagram in Fig. 3.7, the transfer function of the PID-regulator is

$$G_{AVR}(s) = K_P\left(1 + \frac{1}{T_i s}\right)\frac{1 + T_d s}{1 + \frac{T_d}{K_d}s}. \tag{3.16}$$

The values of the parameters of the PID-regulator AVR are given in Table 3.4. The values are the same as in [10].

Table 3.4: Values of the parameters of the PID-regulator AVR

Parameter	Value	Unit
K_P	15	p.u./p.u.
T_i	5	s
T_d	0.3	s
K_d	3	p.u./p.u.

The transfer function from Δe_t to ΔE_{fd} is equal to the multiplication of the transfer functions of the brushless exciter and AVR. With T_{bex} and T_d numerically equal the transfer function from Δe_t to ΔE_{fd} becomes:

$$G_{ex}(s) = K_P\left(1 + \frac{1}{T_i s}\right)\frac{1}{1 + \frac{T_d}{K_d}s}. \tag{3.17}$$

The investigation of the effects caused by the excitation system in terms of the change in electrical air-gap torque can be based on (3.9). The equation for $\Delta\Psi_{fd}$ can be obtained from Fig. 3.6, and it is

$$\Delta\Psi_{fd} = \frac{K_3}{1 + T_{fd}s}\left[-\frac{G_{ex}(s)}{1 + T_R s}(K_6\Delta\Psi_{fd} + K_5\Delta\delta_t) - K_4\Delta\delta_t\right] \tag{3.18}$$

when manual control is assumed [25]. The term $\Delta\Psi_{fd}$ is present on both left and right hand sides in (3.18); hence, the change in electrical air-gap torque can be obtained by rewriting (3.18) into the form $\Delta\Psi_{fd} = P(s)\Delta\delta_t$. Inserting $\Delta\Psi_{fd} = P(s)\Delta\delta_t$ into (3.9) yields [25]:

$$\Delta T_e = K_1\Delta\delta_t + \frac{-K_2 K_3\left(K_4(1 + T_R s) + K_5 G_{ex}(s)\right)}{T_R T_{fd}s^2 + (T_R + T_{fd})s + 1 + K_3 K_6 G_{ex}(s)}\Delta\delta_t. \tag{3.19}$$

Substituting for $G_{ex}(s)$ as given by (3.17) in (3.19) yields

$$\Delta T_e = K_1\Delta\delta_t + \frac{a_1 s^4 + a_2 s^3 + a_3 s^2 + a_4 s + a_5}{b_1 s^5 + b_2 s^4 + b_3 s^3 + b_4 s^2 + b_5 s + b_6}\Delta\delta_t \tag{3.20}$$

where the equations for $a_1,\ldots,a_5$ and $b_1,\ldots,b_6$ are provided in Appendix B.

For the previously considered local mode of oscillation, (3.20) becomes

$$\Delta T_e = 0.7403\Delta\delta_t - 0.0005\Delta\omega_e \tag{3.21}$$

and represents a small decrease in the synchronizing torque component compared to (3.13). Eq. (3.21) also represents a negative damping torque component; therefore, without the presence of any other damping in the SMIB-system the rotor angle would oscillate with an increasing amplitude after a disturbance on the SMIB-system.

3.4.1 Small-Signal Performance of Excitation System

The SM is put into no-load operation by setting the coefficients K_3 and K_6 to one whereas the coefficients K_1, K_2, K_4 and K_5 are put to zero. These are typical no-load values of the coefficients. The field circuit time constant remains at the value presented in Table 3.2.

Fig. 3.8 shows the terminal voltage deviation step response when the voltage reference deviation is stepped to 0.03 p.u. at $t = 0$ s.
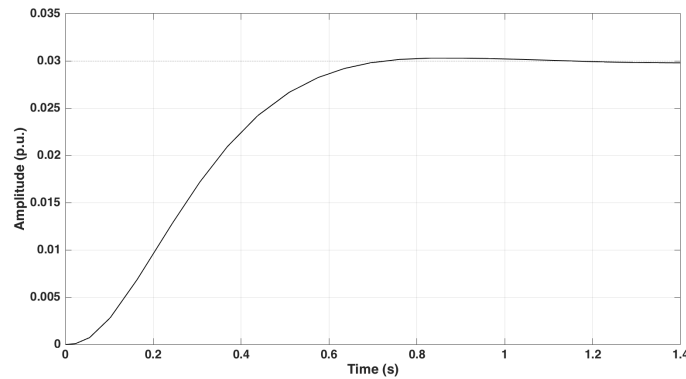
Fig. 3.8: Terminal voltage deviation response when a 0.03 p.u. step is applied to the voltage reference deviation at $t = 0$ s.

The values of the excitation system performance measures are shown in Table 3.5. From the table, it is clear that the values are well within the range of expected values defined in Table 2.1. Thus, the chosen values of the parameters of the PID-regulator AVR presented in Table 3.4 does not need to be modified.

Table 3.5: Values of the excitation system performance measures

Performance Measure	Value	Unit
Rise time (t_r)	0.41	s
Settling time (t_s)	0.63	s
Overshoot	1.31	%

3.5 Including Power System Stabilizer

The block diagram in Fig. 3.6 with field circuit dynamics, exciter, AVR, and voltage transducer showed a negative damping torque component that may cause instability after a disturbance on the SMIB-system. Hence, the model in Fig. 3.6 is further extended by introducing a PSS. Fig. 3.9 shows how the PSS is implemented into the model of the SMIB-system [25].
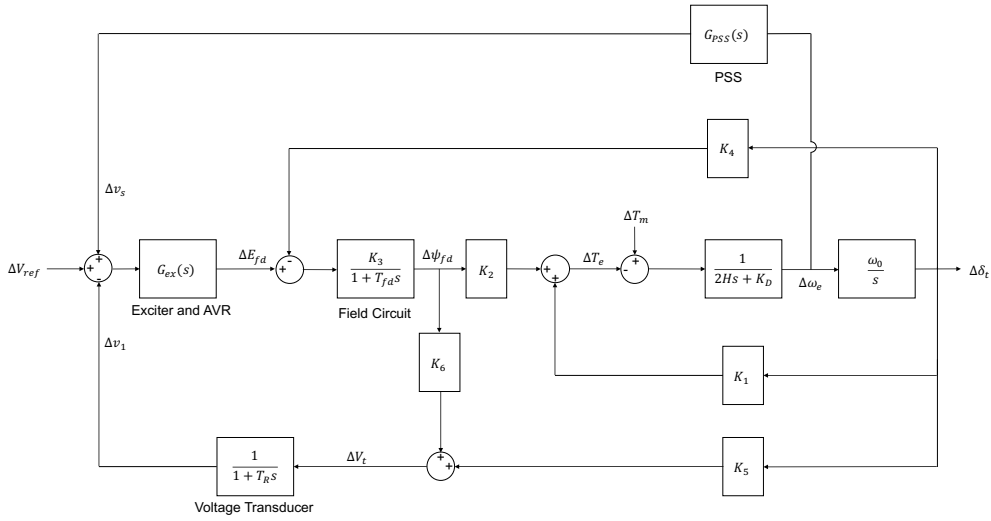
Fig. 3.9: Block diagram of the model of the SMIB-system also including the PSS.

The implemented PSS is a PSS2B where it is assumed that the rotor angular frequency deviation signal perfectly represents the rotor angular frequency deviation. Hence, the PSS utilizes one input signal rather than two input signals. The synthetization block is therefore omitted. In addition, the output limiter block is omitted since it is unnecessary when considering small-signal disturbances [25]. The output of the PSS is fed as an input to the summation block that yields the input to the exciter and AVR block.

Fig. 3.10 depicts the block diagram of the simplified PSS2B that is implemented into the PSS block [38].
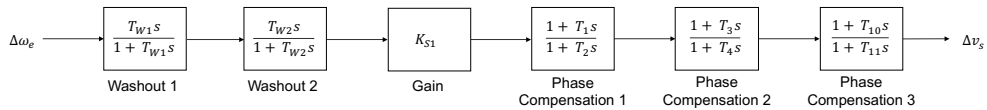
Fig. 3.10: Block diagram of the simplified PSS2B.

The simplified PSS2B comprises two first-order washout filters with time constants T_{W1} and T_{W2}, a gain K_{S1} and three first-order lead-lag filters with time constants T_1 - T_4, T_{10} and T_{11}. The transfer function of the simplified PSS2B is

$$G_{PSS}(s) = K_{S1} \frac{T_{W1}s}{1 + T_{W1}s} \frac{T_{W2}s}{1 + T_{W2}s} \frac{1 + T_1 s}{1 + T_2 s} \frac{1 + T_3 s}{1 + T_4 s} \frac{1 + T_{10}s}{1 + T_{11}s} \tag{3.22}$$

where the gain and the time constants can be used to tune the response of the PSS. The values of the parameters of the simplified PSS2B that are used for implementation of the PSS into Matlab/Simulink are given by Table 3.6.

31

Table 3.6: Values of the parameters of the simplified PSS2B

Parameter	Value	Unit
K_{S1}	10	p.u./p.u.
T_{w1}	7	s
T_{w2}	7	s
T_1	0.1	s
T_2	0.034	s
T_3	0.15	s
T_4	0.051	s
T_{10}	0.15	s
T_{11}	0.051	s

The simplified PSS2B contributes to the total change in electrical air-gap torque. From the block diagram in Fig. 3.9 the contribution from the simplified PSS2B to the total change in electrical air-gap torque is

$$
\begin{aligned}
\Delta T_{e,PSS} = {} & \frac{K_2 K_3 (1 + T_R s)}{(1 + T_3 s)(1 + T_R s) + K_3 K_6} \\
& \cdot \frac{K_{S1} T_{W1} T_{W2} s^2 (1 + T_1 s)(1 + T_3 s)(1 + T_{10} s)}{(1 + T_{W1} s)(1 + T_{W2} s)(1 + T_2 s)(1 + T_4 s)(1 + T_{11} s)} \\
& \cdot \frac{K_P K_d T_i T_d s^2 + (K_P K_d T_i + K_P K_d T_d)s + K_P K_d}{T_d T_{bex} T_i s^3 + (K_d T_{bex} T_i + T_i T_d)s^2 + K_d T_i s} \Delta \omega_e.
\end{aligned}
\tag{3.23}
$$

For the previously considered local mode of oscillation, (3.23) becomes:

$$
\Delta T_{e,PSS} = 2.9723 \Delta \omega_e - j3.2337 \Delta \omega_e.
\tag{3.24}
$$

With $j\Delta\omega_e = js\Delta\delta_t/\omega_0$, (3.24) can be rewritten into the form introduced by (2.5) [25]. Thus, the contribution to the total change in electrical air-gap torque provided by the simplified PSS2B is

$$
\Delta T_{e,PSS} = 0.0647 \Delta \delta_t + 2.9723 \Delta \omega_e
\tag{3.25}
$$

and represents a small positive synchronizing torque component. In addition, the simplified PSS2B contributes with a positive damping torque component. Adding the change in electrical air-gap torque provided by the simplified PSS2B to the change in electrical air-gap torque given by (3.21) yields the total change in electrical air-gap torque [25]. The total change in electrical air-gap torque is:

$$
\Delta T_e = 0.8050 \Delta \delta_t + 2.9718 \Delta \omega_e.
\tag{3.26}
$$

From (3.26) it is clear that the effect of introducing the PSS is to provide additional damping torque; thus, significantly improving the damping of the SMIB-system.

4

Modeling of Dynamic Power Systems

The first section of this chapter explains the modeling of the SMIB-system that is used in the first part of the second objective. The second section explains the modeling of the multi-bus power system that is used in the second and third parts of the second objective.

4.1 The Single-Machine Infinite Bus System

The considered SMIB-system comprises a 120 MVA SM that is connected to an infinite bus via a step-up transformer and a transmission line. The SM is supplying a local load of 80 MW that is located on the high-voltage side of the step-up transformer. The considered SMIB-system is depicted in Fig. 4.1.
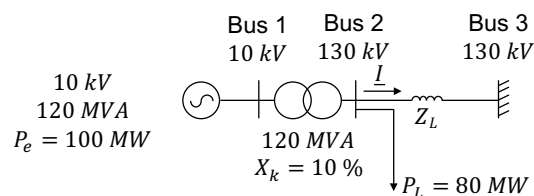
Fig. 4.1: SMIB-system considered in the first part of the second objective.

The SMIB-system is set up in order to represent a general SMIB-system. The values of the parameters of the SM-model are selected to be similar to the values of the parameters of the transient SM-model implemented in Section 3.2. In cases where parameters of the SM-model are undefined in the transient SM-model, standard values are assumed based on [35]. Complete lists of parameter values are provided in Tables A.3 - A.6 in Appendix A. The power system frequency is 50 Hz.

4.1.1 Modeling of Single-Machine Infinite Bus System

For the implementation in Simpow, bus 1 is defined as a PV-bus whereas bus 3 is defined as a swing bus. The infinite bus is modeled as an ideal voltage source behind a short-circuit impedance, and it acts as the reference voltage. The short-circuit impedance that corresponds to the infinite bus is calculated based on an

assumed short-circuit capacity of 7500 MVA and an assumed ratio $X_B/R_B = 10$. The transmission line resistance is $R_L = 0.0001$ p.u./km and the transmission line reactance is $X_L = 0.01$ p.u./km. The length of the transmission line is 60 km. The transformer is modeled as a short-circuit reactance X_k that is equal to 0.1 p.u. The local load is modeled as a symmetrical non-converted constant current load.

4.1.2 Modeling of Synchronous Machine

The dynamic model of the SM includes a field winding, one damper winding in the d-axis direction and two damper windings in the q-axis direction. The SM-model also includes the effects of magnetic saturation [46]. Furthermore, the SM-model includes a turbine and a governor. However, the turbine and governor models are of no significant importance since they do not affect the dynamics due to their comparatively slow response times.

4.1.3 Modeling of Excitation System

The excitation system comprises a PI-regulator AVR, a voltage transducer, and a transient reduction filter. The excitation system is depicted in Fig. 4.2.
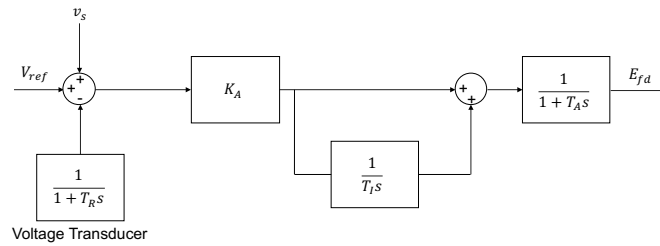
Fig. 4.2: Block diagram of the excitation system.

The PI-regulator AVR is characterized by a gain K_A and an integrator time constant T_I. The voltage transducer is characterized by the time constant T_R whereas the transient reduction filter is characterized by a time constant T_A. The values of the parameters of the excitation system are shown in Table 4.1.

Table 4.1: Values of the parameters of the excitation system

Parameter	Value	Unit
K_A	30	p.u./p.u.
T_A	0.005	s
T_i	1	s
T_R	0.01	s

The small-signal performance of the excitation system is evaluated based on the terminal voltage step response taken during offline operation. Fig. 4.3 shows the terminal voltage response after stepping the reference voltage from 1 p.u. to 1.03 p.u. at $t = 0$ s.
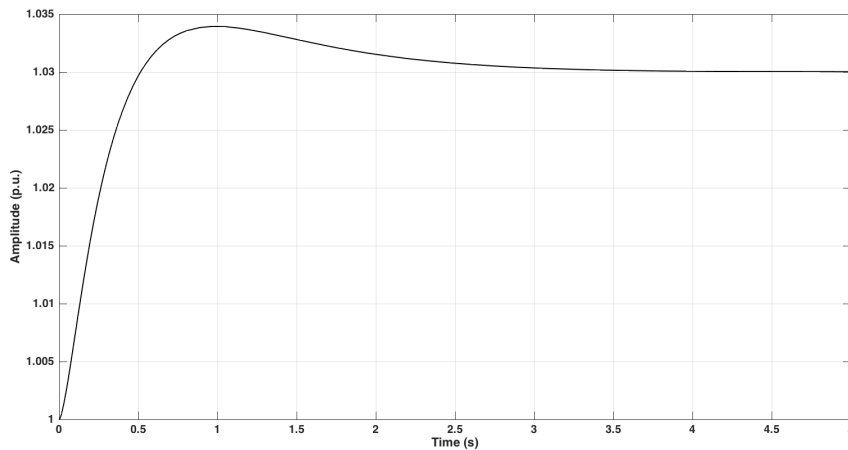
Fig. 4.3: Terminal voltage response when a 0.03 p.u. voltage reference step is applied at $t = 0$ s.

The values of the excitation system performance measures that corresponds to Fig. 4.3 are presented in Table 4.2. From the table it is clear that the values of the performance measures are well within the range of expected values presented in Table 2.1. The table also shows that the excitation system is comparable to the excitation system implemented in Section 3.4 in terms of rise time.

Table 4.2: Values of the excitation system performance measures

Performance Measure	Value	Unit
Rise time (t_r)	0.36	s
Settling time (t_s)	3.66	s
Overshoot	13.13	%

4.1.4 Modeling of Power System Stabilizer

The SM-model includes a PSS2B, and it is depicted in detail in Fig. 2.15. The PSS2B utilizes both rotor angular frequency deviation and electrical power deviation as input signals; however, the constant K_{S2} and the time constants T_8 and T_9 are selected to so that only the rotor angular frequency deviation input signal is used by the PSS. Thus, the constant K_{S2} is set to zero in order to turn off the electric power deviation input signal. Moreover, the time constants T_8 and T_9 are set close to zero in order to eliminate the influence of the ramp-tracking filter. The values of the gain, the time constants of the washout filters, and the time constants of the lead-lag filters are selected so that the PSS2B is properly tuned according to the FIKS-method. A complete list of the values of the parameters of the PSS2B are provided in Table 4.3.

Table 4.3: Values of the parameters of the PSS2B

Parameter	Value	Unit
K_{S1}	8	p.u./p.u.
K_{S2}	0	p.u./p.u.
K_{S3}	1	p.u./p.u.
T_{W1}	7	s
T_{W2}	7	s
T_{W3}	7	s
T_{W4}	7	s
T_1	0.08	s
T_2	0.05	s
T_3	0.22	s
T_4	0.075	s
T_6	0.01	s
T_7	1	s
T_8	0.001	s
T_9	0.001	s
T_{10}	0.22	s
T_{11}	0.075	s
V_{SMAX}	0.05	p.u.
V_{SMIN}	-0.05	p.u.
M_R	5	-
N_R	1	-

4.2 The Multi-Bus Power System

The multi-bus power system considered is the Nordic32-system, and it comprises four main areas, namely: Southwest, Central, North, and External. The four areas are connected through a 400 kV transmission network. Besides the 400 kV transmission network, the Nordic32-system also comprises a 220 kV network and a 130 kV network. The Nordic32-system is characterized by long transmission distances between the major generation sites that are located in the North area and the major load sites that are located in the Central area.

The generation in the North area is stemming from hydro power plants. Besides being the major load area, the Central area also has some generation that stems from thermal power plants. Moreover, the Central area is equipped with a synchronous compensator. The Southwest area is characterized by a low amount of generation and some amount of load whereas the External area is characterized by some generation and some load. Power in the External and Southwest areas are generated in hydro and thermal power plants, respectively [47]. The frequency of the Nordic32-system is 50 Hz. The layout of the Nordic32-system as implemented in Simpow is shown in Fig. 4.4.
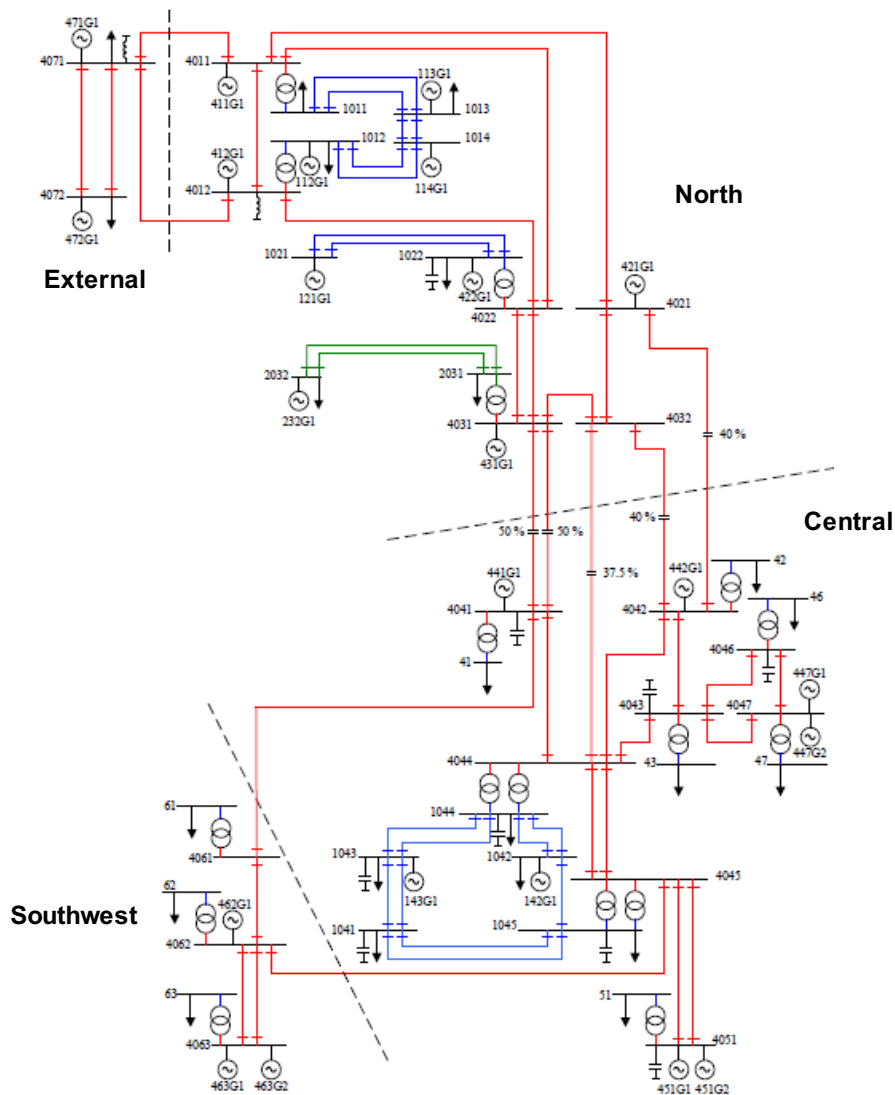
Fig. 4.4: Layout of the Nordic32-system. Red: 400 kV, green: 220 kV, and blue: 130 kV. (Published with courtesy of Joachim Andersson).

The model of the Nordic32-system is provided by Solvina. For complete lists of the values of the parameters of the Nordic32-system the reader is referred to [47], and the reader is also referred to [47] for further details on the Nordic32-system.

The next section describes some of the modeling of the Nordic32-system. In the two following sections are the process of identifying potential PSS locations described as well as the process of replacing the existing SM- and PSS-models at the identified PSS locations. The section concludes with the modeling of the PSS.

4.2.1 Modeling of Nordic32-System

For the modeling of the Nordic32-system, the base MVA is set to 100 MVA and the nominal bus voltages are selected as base voltages. The models of the hydro power plants and the model of the synchronous compensator include the effects of one

field winding, one d-axis damper winding, and one q-axis damper winding; however, the models does not include the effects of magnetic saturation. The models of the thermal power plants include the effects of: one field winding, one d-axis damper winding, two q-axis damper windings, and magnetic saturation [46]. Furthermore, the models of the thermal power plants, the models of the hydro power plants, and the model of the synchronous compensator include the effects of an excitation system, a turbine, a governor, and a PSS. For detailed descriptions of these models the reader is referred to [47].

The loads of the Nordic32-system are modeled as symmetrical non-converted constant impedance loads. For the load modeling, the frequency exponents are 0.75 and 0 for the active and reactive powers, respectively. For further description of the load modeling, the reader is referred to [47]. The transformers are modeled as short-circuit reactances, and the reactance values are found in [47].

4.2.2 Identifying Power System Stabilizer Locations

Eigenvalue calculation of the Nordic32-system reveal that there are 386 non-zero eigenvalues, and all eigenvalues are located strictly in the left half of the complex plane. Only the complex eigenvalues are relevant in the following investigation since they represent modes of oscillation. Sorting out the real eigenvalues leaves 160 complex eigenvalues.

The complex eigenvalues with real parts smaller than -4 are from now on omitted from the investigation since the absolute value of the real parts are turning large in comparison to the imaginary part. Thus, the damping ratios of these complex eigenvalues are high according to (2.2). Fig 4.5 shows the remaining complex eigenvalues after omitting the complex eigenvalues with real parts smaller than -4.
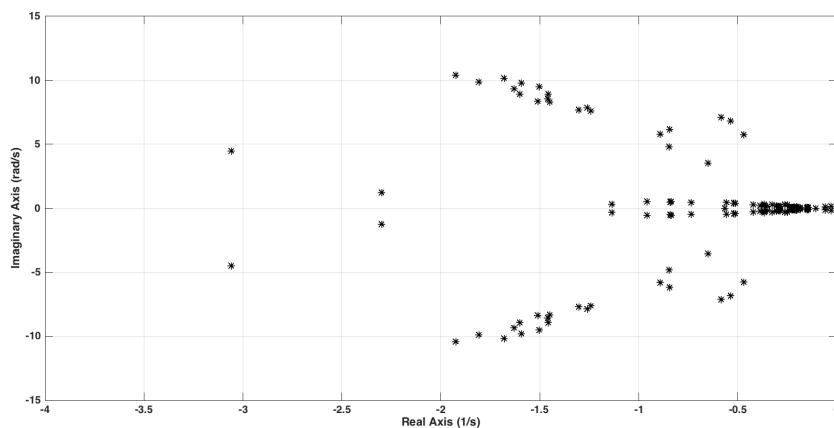
Fig. 4.5: Remaining complex eigenvalues.

To further reduce the number of complex eigenvalues considered, the complex eigenvalues are sorted based on the values of their imaginary parts. Only inter-area modes of oscillation are relevant; thus, only the complex eigenvalues with imaginary parts

in the range of 0.6 - 6.3 rad/s are from now on considered. Table 4.4 shows the remaining complex eigenvalues that are lightly damped and has imaginary parts in the range of 0.6 - 6.3 rad/s.

Table 4.4: Lightly damped complex eigenvalues with imaginary parts in the range of 0.6 - 6.3 rad/s

ID	σ (1/s)	ω (rad/s)	ξ
O1	-0.843	$\pm$6.183	0.135
O2	-0.892	$\pm$5.783	0.152
O3	-0.470	$\pm$5.780	0.081
O4	-0.845	$\pm$4.811	0.173
O5	-0.648	$\pm$3.520	0.181

To give an indication of the type of oscillation mode associated with each of the complex eigenvalues in the table, a modal analysis is performed. As an example, Fig. 4.6 shows the mode shape of the oscillation mode associated with the complex eigenvalue O5. It should be pointed out that only the largest contributions to the oscillation mode are shown in the figure; thus, contributions from several SMs are omitted. This is done in order to increase the readability of the figure.
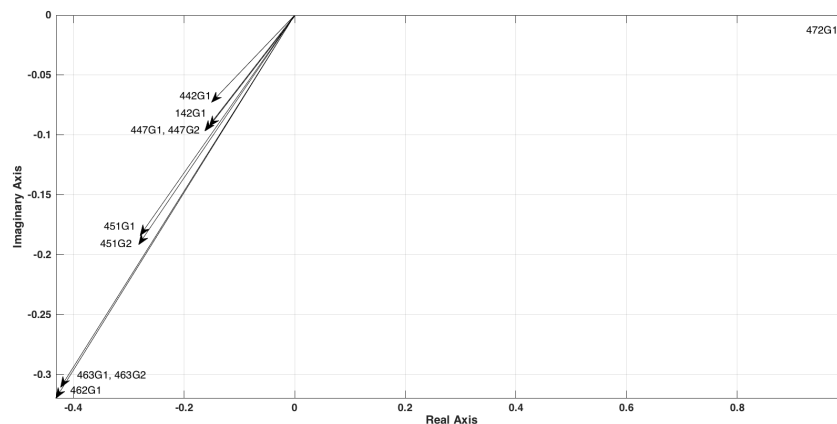
Fig. 4.6: Mode shape of the oscillation mode associated with the complex eigenvalue O5.

From the figure, it is indicated that 472G1 is oscillating against 462G1, 463G1 and 463G2. In addition, the mode shape also indicates that 451G1, 451G2, 447G1, and 447G2 are oscillating against 472G1. However, they are not as involved in the oscillation as 462G1, 463G1 and 463G2. To verify this, the participation factors are calculated.

Table 4.5 shows the largest contributors to the oscillation mode associated with the complex eigenvalue O5. The table shows the largest contributions from the SMs in the Nordic32-system as well as the contributions from their state variables.

Table 4.5: Largest participation factors of the oscillation mode associated with the complex eigenvalue O5

	463G1	**463G2**	**472G1**
δ_t	0.110	0.110	0.164
ω_e	0.108	0.108	0.164
Field winding	0.052	0.052	0.037
d-axis damper winding	0.007	0.007	0.003

The table shows two things regarding the contributions to the O5 oscillation mode: 1) the rotor angle and the angular frequency are the largest contributors among the state variables, and 2) that 472G1, 463G1, and 463G2 are the largest contributors to the oscillation mode among the SMs in the Nordic32-system. The former reveals that the oscillation mode is an electro-mechanical mode of oscillation. The latter reveals that the oscillation mode is an inter-area mode of oscillation since 472G1 is located in the North area whereas 463G1 and 463G2 are located in the Southwest area.

The same analysis is performed on the remaining complex eigenvalues in Table 4.4. The result from the analysis shows that most of the oscillation modes associated with the complex eigenvalues are inter-area modes of oscillation. However, the complex eigenvalue O2 is a local mode of oscillation. The result from the analysis is summarized in Table 4.6.

Table 4.6: Types of oscillation modes associated with the lightly damped complex eigenvalues with imaginary parts in the range of 0.6 - 6.3 rad/s

ID	σ	ω	ξ	Type
O1	-0.843	±6.183	0.135	Inter-area
O2	-0.892	±5.783	0.152	Local
O3	-0.470	±5.780	0.081	Inter-area
O4	-0.845	±4.811	0.173	Inter-area
O5	-0.648	±3.520	0.181	Inter-area

The above calculation of the participation factors reveals that, in addition to 472G1; 463G1; and 463G2, other SMs that are contributing to the inter-area modes of oscillation in Table 4.6 are: 462G1, 451G1, 451G2, 447G1, and 447G2. This suggests that possible PSS locations may be buses 4072, 4063, 4062, 4051, and 4047. However, it is not reasonable to place the PSS2B at bus 4072 since the rated power of 472G1 is very large in comparison to the rated power of all other SMs. To decide whether buses 4063, 4062, 4051, and 4047 are suitable PSS locations, the amplitude response of the NG-method with PSS disconnected is taken at these buses. The amplitude responses taken at buses 4062, 4051, and 4047 show similar characteristics with PSS disconnected; therefore, out of buses 4062 4051, and 4047 only bus 4062 is selected as PSS location. This infers that buses 4063 and 4062 are identified as locations where the PSS2B is to be placed in the Nordic32-system.

4.2.3 Replacing Synchronous Machines at Buses 4063 and 4062

For purposes of analyzing the performance of the two evaluation methods, the existing SM-models at buses 4063 and 4062 are replaced with the SM-model utilized in the dynamic simulations of the SMIB-system. This is done for each of the PSS locations one at a time. In cases where there are two SMs connected to the bus, both SMs are replaced simultaneously. This is the case when replacing the SM-models at bus 4063.

When replacing the existing SM-models at buses 4063 and 4062, the existing models of the excitation systems and the PSSs are also replaced with the models of the excitation system and PSS2B utilized in the dynamic simulations of the SMIB-system. However, the existing turbine and governor models are not replaced with the turbine and governor models utilized in the dynamic simulations of the SMIB-system. The reason for this is that the turbine and governor does not affect the dynamics due to their comparatively slow response times.

Upon replacement of the existing SM-models, the replacing SM-model is scaled in terms of its rated power and rated voltage. Consequently, when replacing the existing SM-models at bus 4063, the rated power of the replacing SM-model is increased to 600 MVA. When the SM-model replaces the existing SM-model at bus 4062 the rated power of the replacing SM-model is increased to 700 MVA. By doing this, the same steady state power flow solution is obtained as with the originally existing SM-models. It is enough to only scale the SM-model in terms of its rated power since all parameters of the SM-model are normalized and given in per unit.

4.2.4 Modeling of Power System Stabilizer

For each PSS location, the PSS2B is tuned so that it is properly tuned according to both evaluation methods. Besides, for each of the two evaluation methods, two different tunings of the PSS2B are tested. Thus, this yields four sets of values of the parameters of the PSS2B where only the gain, the time constants of the washout filters, and the time constants of the lead-lag filters are used to tune the PSS2B. Tables A.7 and A.8 in Appendix A show the values of the parameters of the PSS2B for each of the PSS locations for both tunings. The values of K_{S2}, K_{S3}, T_6, T_7, T_8, T_9, V_{SMAX}, V_{SMIN}, M_R, and N_R do not change since the PSS2B only utilizes the angular frequency deviation input signal. Thus, the values of these parameters are the same as in Table 4.3. Therefore, presentation of the values of these parameters are omitted from Tables A.7 and A.8 in Appendix A.

5

Linearized Simulations

This chapter first establishes the reference responses of the two evaluation methods. The chapter then investigates how variations in the values of the parameters of the simplified PSS2B affect the responses obtained by the two evaluation methods. This is done by first varying a certain parameter of the PSS2B; then, the new responses are obtained with both evaluation methods. These new responses are then compared with the reference responses established in the first section of the chapter. The chapter concludes with an overview of the tested combinations.

5.1 Reference Responses

This section establishes the reference responses of the two evaluation methods. The reference responses are the responses obtained by the two evaluation methods when the values of the parameters of the simplified PSS2B are as given by Table 3.6.

5.1.1 Reference Response of FIKS-Method

Fig. 5.1 shows the response from the output of the PSS2B to the terminal voltage deviation for three operation conditions of the SM: offline, loaded ($P_e = 0.695$ p.u. and $Q_e = 0.1745$ p.u.), and lightly loaded ($P_e = 0.003$ p.u. and $Q_e = 0.1235$ p.u.).
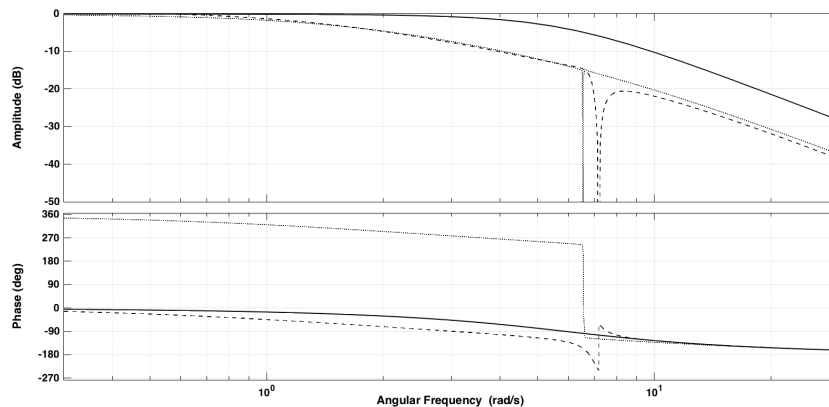
Fig. 5.1: Response from the PSS output to the terminal voltage deviation for different operating conditions of the SM. Solid: offline, dashed: loaded, and dotted: lightly loaded.

The first thing to notice in Fig. 5.1 is the decline in amplitude and phase characteristics that occurs for all responses at high angular frequencies. The second thing to notice is that the amplitude and phase characteristics are reduced as the SM turns from offline to loaded operation. The large peaks in both amplitude and phase characteristics when the SM is in loaded operation can be attributed to the fact that the electro-mechanical oscillations are lightly damped without the PSS.

The FIKS-method considers the response from the PSS input to the terminal voltage when the SM is operating offline. Thus, the coefficients in Fig. 3.9 are set to their appropriate no-load values: $K_3 = K_6 = 1$ and $K_1 = K_2 = K_4 = K_5 = 0$. The value of the field circuit time constant is kept at its original value. Consequently, the block diagram in Fig. 3.9 can be reduced to the block diagram shown in Fig. 5.2. From Fig. 5.2, it can be seen that the response obtained by the FIKS-method represents an open-loop response. It should be stressed that the block diagram in the figure only applies to offline operation of the SM.
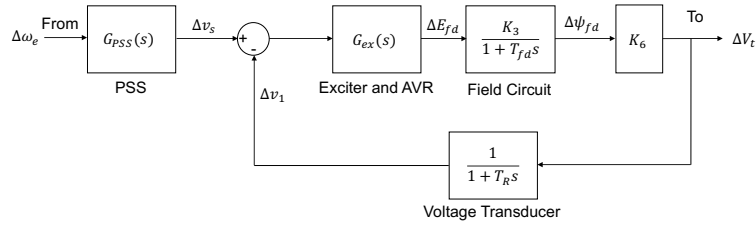
Fig. 5.2: Input and output points of the FIKS-method.

Fig. 5.3 shows the reference response of the FIKS-method, and the figure also shows the responses obtained by the FIKS-method when the SM is operating under the same loaded conditions as in Fig. 5.1.
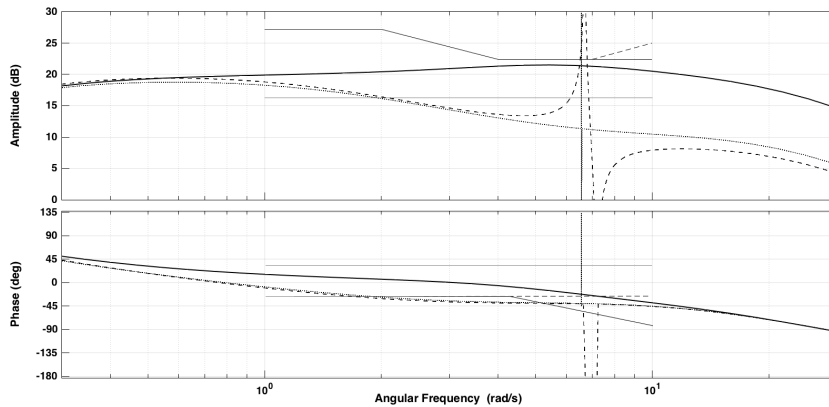
Fig. 5.3: Response obtained by the FIKS-method for different operating conditions of the SM. Solid: reference response (offline), dashed: loaded, and dotted: lightly loaded.

From the figure, it is obvious that the amplitude and phase characteristics are significantly reduced when the SM is in loaded operation compared with offline operation.

Moreover, it is clear that the reference response of the FIKS-method is inside the limits; thus, the PSS is able to compensate for the decline in the amplitude and phase characteristics caused by the exciter and AVR. However, this is not the case when the SM is in either of the two cases of loaded operation.

5.1.2   Reference Amplitude Response of NG-Method

Fig. 5.4 illustrates the input and output points of the NG-method. The amplitude response obtained with the NG-method is a closed-loop amplitude response.
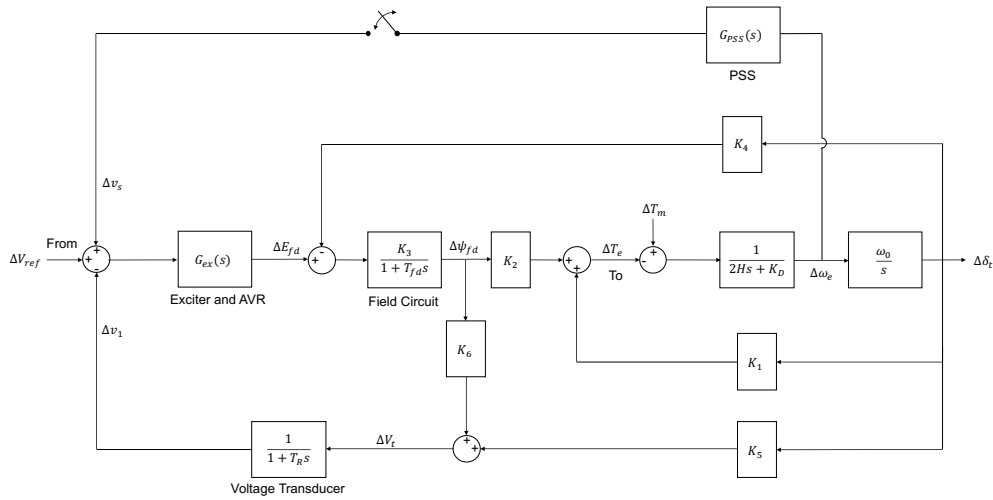
Fig. 5.4: Input and output points of the NG-method.

Fig. 5.5 shows the reference amplitude response of the NG-method. From the figure, it is clear that the PSS is improperly tuned since the amplitude response with PSS connected is partly above the amplitude response with PSS disconnected. The crossing of the amplitude responses occurs at 7.11 rad/s and is inside the range 1.26 - 18.85 rad/s.
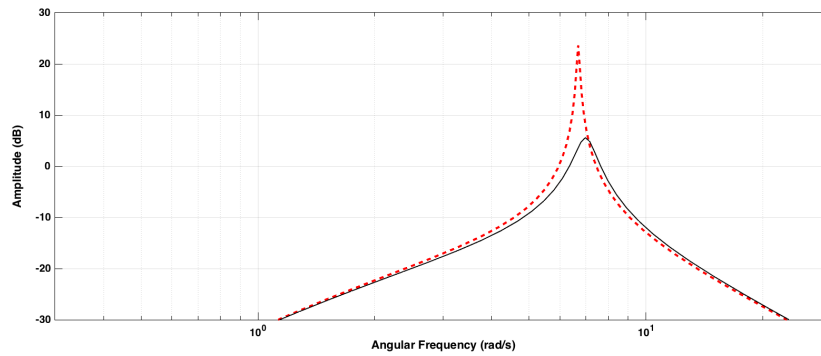
Fig. 5.5: Reference amplitude response obtained by the NG-method. Solid: PSS connected and red dashed: PSS disconnected.

5.2 Varying Gain

Fig. 5.6 shows the effects of varying the gain of the simplified PSS2B in terms of the response obtained by the FIKS-method. The figure also shows the effects of varying the gain in terms of the amplitude response obtained by the NG-method.
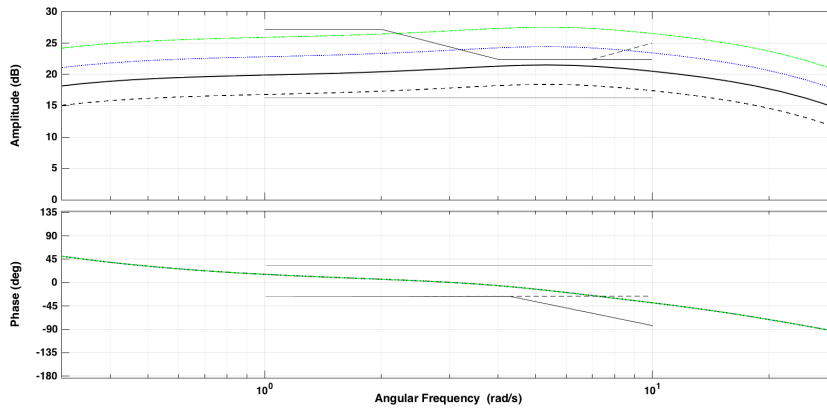
(a)
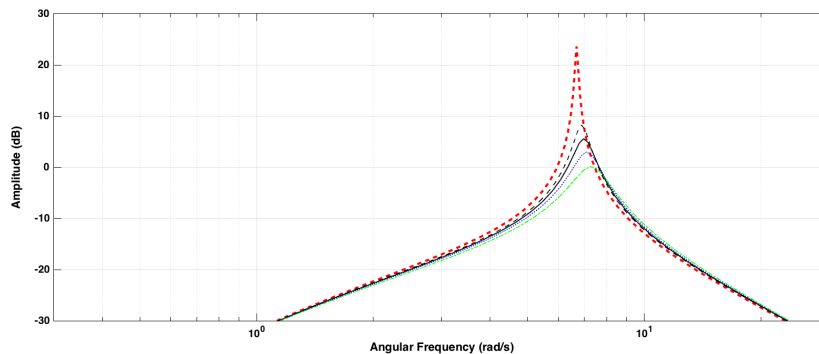
(b)

Fig. 5.6: Varying K_{S1}. Solid: $K_{S1} = 10$; dashed: $K_{S1} = 7$; blue dotted: $K_{S1} = 14$; and green dash-dotted: $K_{S1} = 20$. *(a)* FIKS-method. *(b)* NG-method. Red dashed: PSS disconnected.

In Fig. 5.6.(a), the effect of varying the gain is to shift the amplitude characteristic along the y-axis whereas the phase characteristic remains unaffected. The way in which the gain variations affect the response is attributed to the fact that the response obtained by the FIKS-method is an open-loop response. By referring to Fig. 5.2, the response of the FIKS-method can be decomposed into the responses from all the individual blocks of the PSS as well as the response of an imagined block representing the system from the PSS output to the terminal voltage deviation. Thus, only the response of the gain block is affected by the gain variation. The phase associated with a pure gain is zero and a gain variation therefore only affects the amplitude characteristic.

In terms of the amplitude response of the NG-method, Fig. 5.6.(b) shows that varying the gain affects the amplitude response around the resonance peak. An increase in gain corresponds to a reduction in the amplitude response around the resonance peak whereas a decrease in gain has the opposite effect. Thus, increasing the PSS gain provides a way of improving the performance of the PSS according to the NG-method. This is not the case in terms of the response of the FIKS-method where, for the values of the parameters of the PSS considered, the PSS remains properly tuned only for small variations in the gain.

The NG-method yields a closed-loop amplitude response, and this makes the investigation of the reasons behind the changes in its amplitude response more complex compared with the investigation of the reasons behind the changes in the response of the FIKS-method. This is due to the fact that the approach of decomposing the response into its individual components cannot be utilized. Nevertheless, the reasons behind the changes in the amplitude response of the NG-method can be investigated by studying an appropriate open-loop response.

The appropriate open-loop response can be obtained by breaking up the closed-loop system at the PSS output; subsequently, the open-loop response from the voltage reference deviation to the PSS output is taken. The input and output points of this open-loop system are depicted in Fig. 5.7. This open-loop response should not be confused with the response of the FIKS-method.
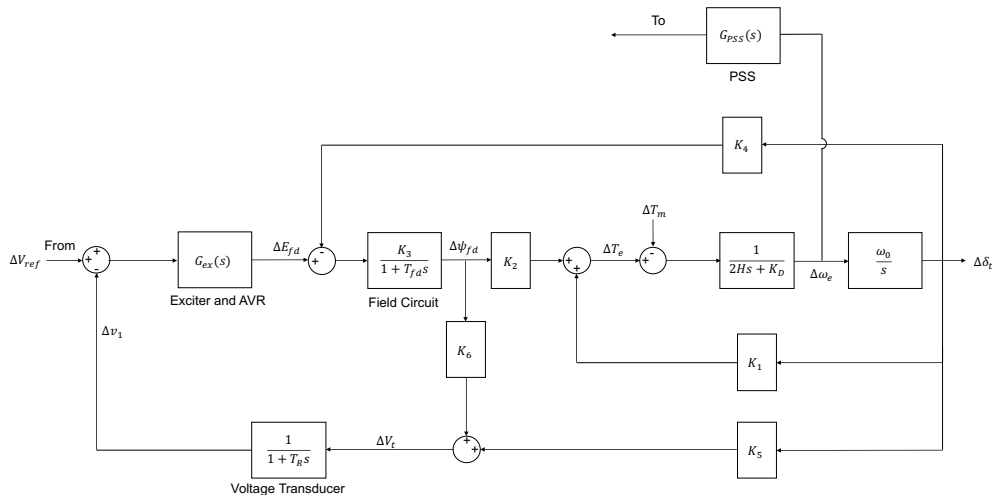
Fig. 5.7: Input and output points utilized to obtain the open-loop response from the voltage reference deviation to the PSS output.

From the amplitude and phase characteristics of the open-loop response, the resulting damping of the corresponding closed-loop system can be determined. Hence, the reasons behind the changes in the amplitude response of the NG-method can be attributed to the combination of the changes in the open-loop amplitude and phase characteristics. The open-loop response that corresponds to the reference amplitude response of the NG-method acts as the open-loop reference response.

Fig. 5.8 shows the open-loop response obtained from the voltage reference deviation to the PSS output. The figure gives the open-loop responses that correspond to each of the amplitude responses in Fig. 5.6.(b). However, the case where the PSS is disconnected is omitted. The solid response in Fig. 5.8 is the open-loop reference response.
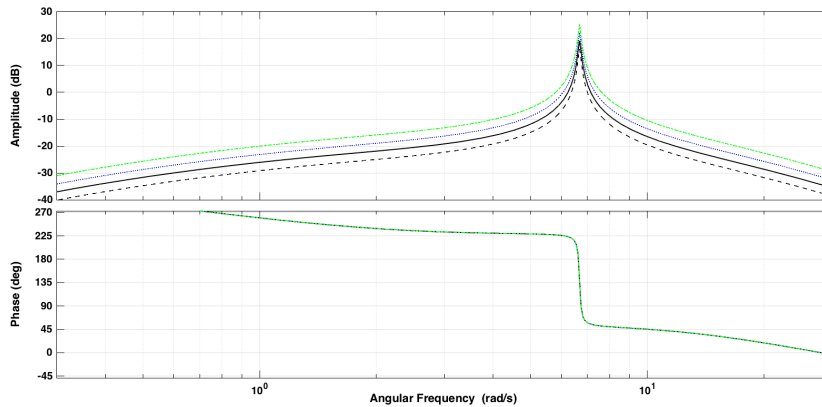
Fig. 5.8: Open-loop response from the voltage reference deviation to the PSS output for different values of K_{S1}. Solid: $K_{S1} = 10$; dashed: $K_{S1} = 7$; blue dotted: $K_{S1} = 14$; and green dash-dotted: $K_{S1} = 20$.

The closed-loop system considered by the NG-method exhibits positive feedback; therefore, it is desirable that the open-loop phase characteristic is equal to 180 deg in order for the closed-loop system to be well damped. For a fixed value of the open-loop phase that is inside the range of 180 ± 90 deg at a specific angular frequency, an increase in the open-loop amplitude results in a reduction in the amplitude response of the NG-method at the considered angular frequency. On the other hand, considering a specific angular frequency and keeping the open-loop amplitude fixed and letting the value of the open-loop phase deviate from 180 deg increases the amplitude response of the NG-method at that specific angular frequency. Letting the value of the open-loop phase increase beyond 270 deg or below 90 deg for a specific angular frequency with fixed open-loop amplitude, yields a heavy increase in the amplitude response of the NG-method at that angular frequency. As the open-loop phase approaches 360 deg or 0 deg at a specific angular frequency, the amplitude of the NG-method at that angular frequency increases almost infinitely. This is true unless the open-loop amplitude is very high or very low at that specific angular frequency.

Varying the PSS gain only affects the open-loop amplitude characteristic in Fig. 5.8; therefore, the change in the amplitude response of the NG-method is caused by the change in the open-loop amplitude characteristic. This can be seen by comparing the new open-loop amplitude characteristics with the reference open-loop amplitude characteristic. For angular frequencies where the open-loop phase characteristic in Fig. 5.8 is inside 180 ± 90 deg, increased open-loop amplitude is directly reflected

as a reduction in the amplitude response of the NG-method in Fig. 5.6.(b). Consequently, decreased open-loop amplitude is reflected as an increase in the amplitude response of the NG-method for the range of angular frequencies where the open-loop phase characteristic is inside 180 ± 90 deg. This is illustrated by comparing how the changes represented by the green dash-dotted and the dashed responses away from the solid response in Fig. 5.8 are reflected in Fig. 5.6.(b), for angular frequencies below approximately 6.5 rad/s.

5.3 Varying Time Constants of the Washout Filters

Fig. 5.9 illustrates the effects of varying the time constants of the washout filters in terms of the responses of the two evaluation methods. The values of the time constants of the washout filters are varied in the range of 2 - 14 s, which are typical values for PSS applications [25].
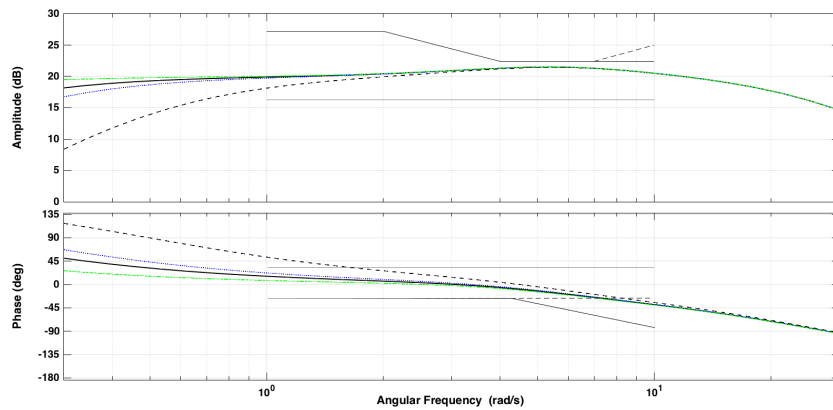
(a)
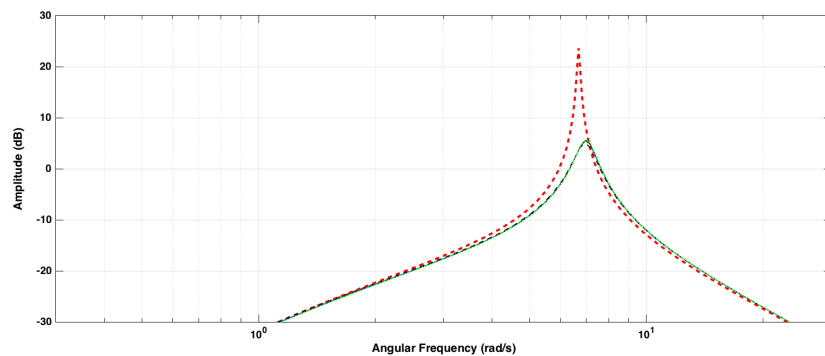
(b)

Fig. 5.9: Varying T_{W1} and T_{W2}. Solid: $T_{W1} = T_{W2} = 7$ s; dashed: $T_{W1} = T_{W2} = 2$ s; blue dotted: $T_{W1} = T_{W2} = 5$ s; and green dash-dotted: $T_{W1} = T_{W2} = 14$ s. *(a)* FIKS-method. *(b)* NG-method. Red dashed: PSS disconnected.

Fig. 5.9.(a) illustrates the effects of varying the time constants of the washout filters in terms of the response of the FIKS-method. In the range of 1 - 10 rad/s, the variations of the time constants primarily affect the phase characteristic; thus, providing a way of tuning the response at angular frequencies in the lower end of 1 - 10 rad/s. Increased values of the time constants yields a reduced phase lead at low angular frequencies whereas the opposite is true for a reduction in the time constants. From the figure it is clear that the new responses stay within the limits given by the FIKS-method except in the case represented by the dashed response where the time constants equal 2 s.

Varying the time constants of the washout filters show no effect on the amplitude response of the NG-method, and this can be seen by studying Fig. 5.9.(b). The absence of any effects in terms of the amplitude response of the NG-method can be attributed to the open-loop response from the voltage reference deviation to the PSS output. The change in the open-loop phase characteristic occurs where the open-loop amplitude characteristic is low; hence, the amplitude response of the NG-method is unaffected.

5.4 Varying Time Constants of the Lead-Lag Filters

The transfer functions of the lead-lag filters of the phase compensation block in Fig. 3.10 are from now on denoted $G_{ll1}(s)$, $G_{ll2}(s)$, and $G_{ll3}(s)$ for the first, second and third lead-lag filters, respectively. The transfer function of the phase compensation block is denoted $G_{pc}(s)$ and is equal to $G_{pc}(s) = G_{ll1}(s) \cdot G_{ll2}(s) \cdot G_{ll3}(s)$.

The initial values of the time constants are provided in Table 3.6, and they are repeated in Table 5.1 for purposes of convenience. The table also shows the initial values of the break angular frequencies associated with the time constants of the lead-lag filters.

Table 5.1: Initial values of the time constants of the lead-lag filters of the simplified PSS2B and their associated break angular frequencies

Time Constant			Break Angular Frequency		
Parameter	Value	Unit	Parameter	Value	Unit
$T_{1,0}$	0.1	s	$\omega_{1,0}$	10	rad/s
$T_{2,0}$	0.034	s	$\omega_{2,0}$	29.41	rad/s
$T_{3,0}$	0.15	s	$\omega_{3,0}$	6.67	rad/s
$T_{4,0}$	0.051	s	$\omega_{4,0}$	19.61	rad/s
$T_{10,0}$	0.15	s	$\omega_{10,0}$	6.67	rad/s
$T_{11,0}$	0.051	s	$\omega_{11,0}$	19.61	rad/s

This section investigates how variations in the time constants of the lead-lag filters affect the responses obtained by the two evaluation methods. The effects of varying the ratios of the time constants of the lead-lag filters in different combinations are investigated rather than varying each time constant independently. Thus, the following ratios are introduced: $r_1 = T_1/T_2$, $r_2 = T_3/T_4$ and $r_3 = T_{10}/T_{11}$, for $G_{ll1}(s)$, $G_{ll2}(s)$, and $G_{ll3}(s)$, respectively. In cases where $r_1 = r_2 = r_3$, r is used to denote the ratios for purposes of simplification. The initial values of the ratios are calculated by the use of the initial values of the time constants of the lead-lag filters provided in Table 5.1. The initial values of the ratios are: $r_{1,0} = r_{2,0} = r_{3,0} = 2.941 = r_0$.

Fig. 5.10 shows the effects of varying r in terms of the response obtained by the FIKS-method. The figure also shows the effects of varying r in terms of the amplitude response of the NG-method. The values of the time constants of the lead-lag filters are provided in Table C.1 in Appendix C.
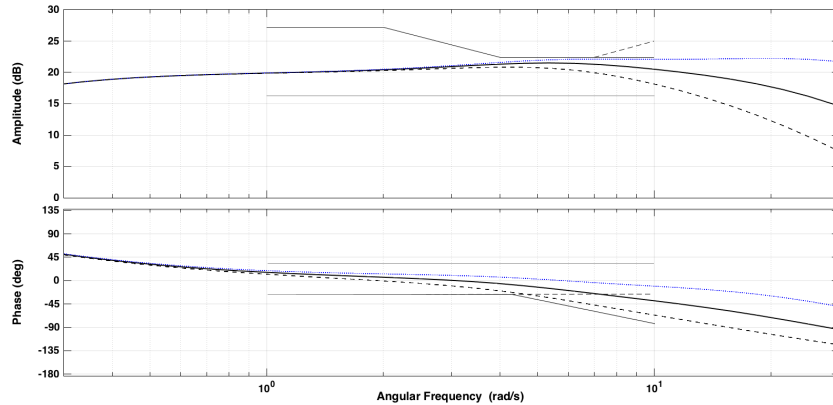
(a)
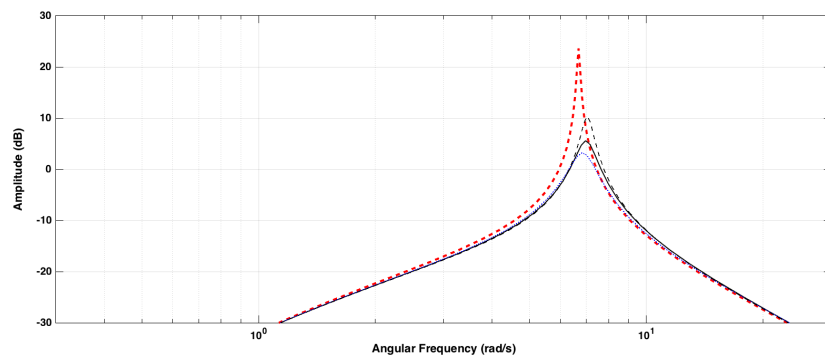
(b)

Fig. 5.10: Varying r. Solid: $r_0 = 2.941$; dashed: $r = 2$; and blue dotted: $r = 5$. *(a)* FIKS-method. *(b)* NG-method. Red dashed: PSS disconnected.

In Fig. 5.10.(a), increasing r above 2.941 increases both the amplitude and the phase characteristics of the FIKS-method at higher angular frequencies. The effect is the opposite if r is decreased below 2.941. The decomposition of the response of the FIKS-method into the responses of the individual blocks in Fig. 5.2 allows for isolating the effects of varying r to the response of $G_{pc}(s)$ only. Increasing r above 2.941 results in an increase in the response of $G_{pc}(s)$ compared with the response of $G_{pc}(s)$ when $r = 2.941$. The opposite is true when r is decreased below 2.941. Adding the response of $G_{pc}(s)$ to the responses of all other individual blocks in Fig. 5.2 yields the response of the FIKS-method. The changes in the response of $G_{pc}(s)$ are directly seen in the response of the FIKS-method since the responses of the other individual blocks in Fig. 5.2 are unaffected by the variations in r.

In terms of the amplitude response of the NG-method, the effects of varying r is to influence the amplitude response around the resonance peak, as illustrated in Fig. 5.10.(b). An increase in r compared with 2.941 results in reduced amplitude response around the resonance peak whereas the opposite holds for a decrease in r compared with 2.941. Even though the amplitude response is reduced so that it is below the red dashed amplitude response for angular frequencies around the resonance peak, the PSS is not properly tuned according to the NG-method. This is due to the blue dotted amplitude response being slightly above the red dashed amplitude response for angular frequencies above approximately 8 rad/s.

The reasons behind the way in which the variations in r affect the amplitude response of the NG-method can be explained based on the open-loop response from the voltage reference deviation to the PSS output. The open-loop responses are illustrated in Fig. 5.11 for the same values of r as considered in Fig. 5.10.
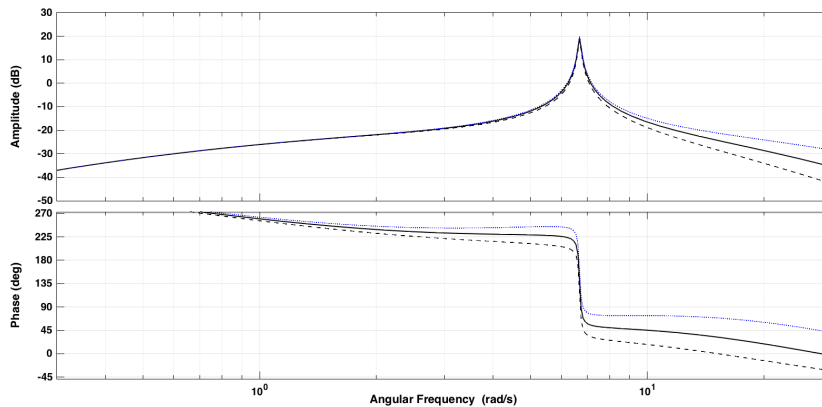
Fig. 5.11: Open-loop response from the voltage reference deviation to the PSS output for different values of r. Solid: $r_0 = 2.941$; dashed: $r = 2$; and blue dotted: $r = 5$.

Considering the blue dotted open-loop response that represents the case when r is increased from 2.941 to 5 at angular frequencies above approximately 6.5 rad/s, the improved open-loop phase characteristic in Fig. 5.11 yields reduced amplitude

response in Fig. 5.10.(b). This can be seen by comparing the blue dotted amplitude response with the solid amplitude response in Fig. 5.10.(b). The effect is the opposite when considering the case where r is decreased from 2.941 to 2 for angular frequencies above 6.5 rad/s. The same reasoning applies for angular frequencies below 6.5 rad/s.

Fig. 5.12 shows the effect of varying r after the break angular frequencies associated with $G_{ll1}(s)$, $G_{ll2}(s)$, and $G_{ll3}(s)$ are halved compared with their initial values; thus, shifting the response of G_{pc} to the left along the x-axis. The values of the time constants of the lead-lag filters are provided in Table C.2 in Appendix C.
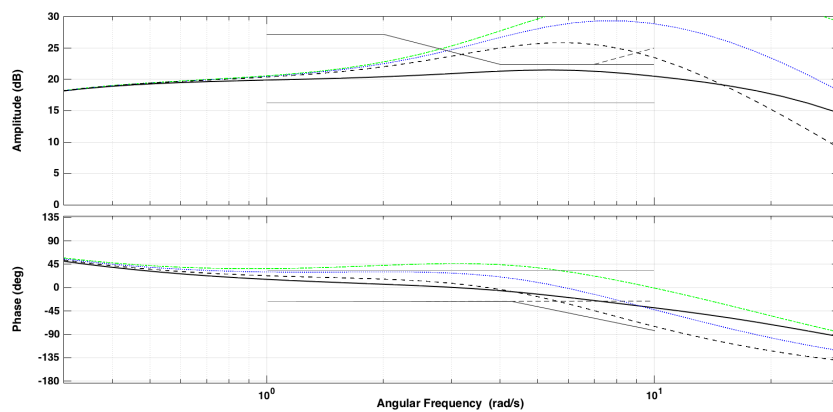
(a)
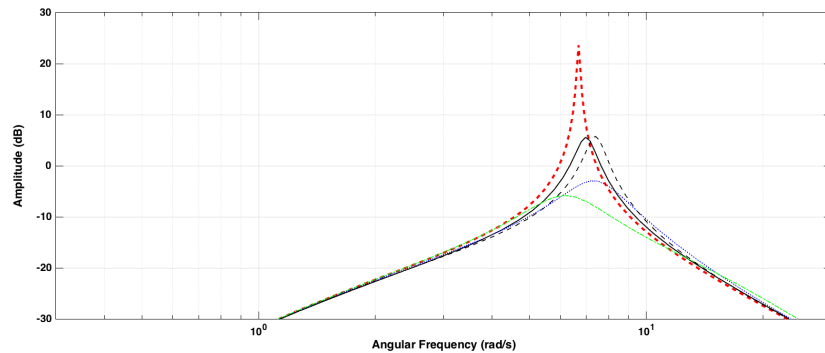
(b)

Fig. 5.12: Varying r after the initial halving of the break angular frequencies of $G_{ll1}(s)$, $G_{ll2}(s)$, and $G_{ll3}(s)$. Solid: $r_0 = 2.941$; dashed: $r = 2$; blue dotted: $r = 2.941$; and green dash-dotted: $r = 5$. *(a)* FIKS-method. *(b)* NG-method. Red dashed: PSS disconnected.

Shifting the response of G_{pc} to the left along the x-axis results in an improperly tuned PSS according to the FIKS-method. This holds for all values of r, as illustrated in Fig. 5.12.(a). The effects of halving the break angular frequencies with the following variation in r can again be explained by studying the response of $G_{pc}(s)$.

The shifting of the response of $G_{pc}(s)$ to the left along the x-axis causes the contribution from $G_{pc}(s)$ to the response of the FIKS-method to be shifted towards lower angular frequencies. Thus, the response of the FIKS-method becomes over compensated, and the over compensation is further increased if r is increased above 2.941. Reducing r below 2.941 reduces the amount of over compensation; however, the response provided by the FIKS-method is still exceeding its limits.

In Fig. 5.12.(b), the initial shifting of the response of $G_{pc}(s)$ to the left along the x-axis yields reduced amplitude response around the resonance peak. In opposite to the FIKS-method, the initial halving of the break angular frequencies of the lead-lag filters partly improves the performance of the PSS according to the NG-method. Increasing r from 2.941 to 5 further reduces the amplitude response of the NG-method around the resonance peak as well as reduces the resonance angular frequency. This is illustrated by the blue dotted and green dash-dotted amplitude responses. However, for angular frequencies above approximately 15 rad/s, the green dash-dotted amplitude response is just above the amplitude response obtained with the PSS being disconnected.

The reasons behind the changes in the amplitude response of the NG-method are again investigated by taking the open-loop response from the voltage reference deviation the the PSS output. The resulting open-loop response is shown in Fig. 5.13 where r is varied in the same way as in Fig. 5.12.
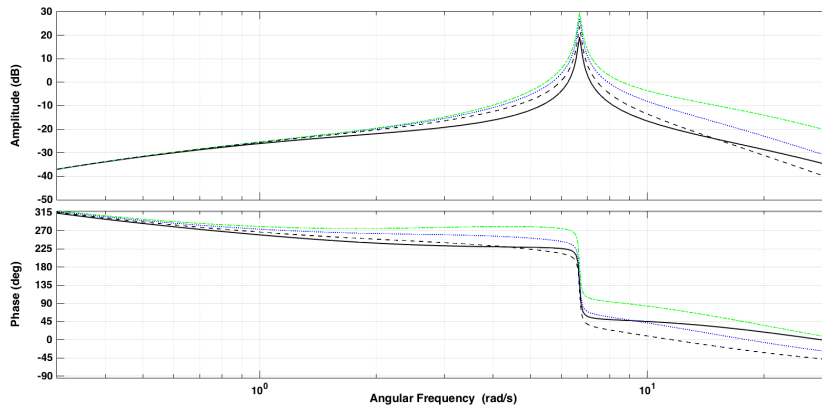
Fig. 5.13: Open-loop response from the voltage reference deviation to the PSS output for different values of r after the initial halving of the break angular frequencies of $G_{ll1}(s)$, $G_{ll2}(s)$, and $G_{ll3}(s)$. Solid: $r_0 = 2.941$; dashed: $r = 2$; blue dotted: $r = 2.941$; and green dash-dotted: $r = 5$.

The green dash-dotted amplitude response in Fig. 5.12 represents a reduction in the amplitude response around the resonance peak compared with the reference amplitude response. This is largely due to the combination of increased open-loop amplitude characteristic and improved open-loop phase characteristic. This can be seen by comparing the green dash-dotted and solid responses in Fig. 5.13 for angular frequencies above 6.5 rad/s. For angular frequencies below 6.5 rad/s, the increase in

the open-loop amplitude characteristic does not compensate for the worsened open-loop phase characteristic. Thus, the green dash-dotted amplitude response increases above the solid amplitude response in Fig. 5.12.(b).

Fig. 5.14 shows the effect of varying r after the break angular frequencies associated with $G_{ll1}(s)$, $G_{ll2}(s)$, and $G_{ll3}(s)$ are doubled compared with their initial values. This generates a shift in the response of $G_{pc}(s)$ to the right along the x-axis. The detailed values of the time constants can be found in Table C.3 in Appendix C.
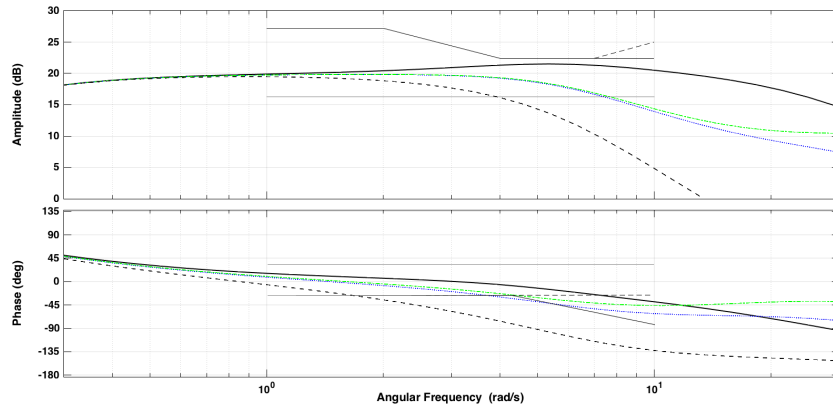
(a)
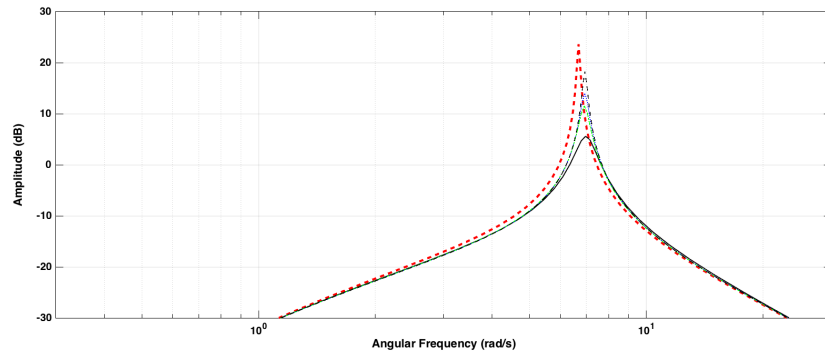
(b)

Fig. 5.14: Varying r after the initial doubling of the break angular frequencies of $G_{ll1}(s)$, $G_{ll2}(s)$, and $G_{ll3}(s)$. Solid: $r_0 = 2.941$; dashed: $r = 2$; blue dotted: $r = 2.941$; and green dash-dotted: $r = 5$. *(a)* FIKS-method. *(b)* NG-method. Red dashed: PSS disconnected.

In Fig. 5.14.(a), the PSS is improperly tuned for all values of r considered. The figure shows that the PSS is unable to compensate for the strong decline in the amplitude and phase characteristics caused by the AVR. This occurs because the response of $G_{pc}(s)$ primarily contributes to the response of the FIKS-method at high angular frequencies.

In Fig. 5.14.(b), the amplitude response around the resonance peak is increased as the break angular frequencies are initially doubled. Varying r then yields more or less increase in the amplitude response. This can again be explained based on the open-loop response from the voltage reference deviation to the PSS output. As the response of $G_{pc}(s)$ is shifted into higher angular frequencies, the open-loop amplitude characteristic is largely decreased; therefore, generating the increased amplitude response around the resonance peak for all values of r.

Fig. 5.15 investigates the effects of varying r after the break angular frequencies of $G_{ll1}(s)$ are initially doubled compared with their initial values. In addition, the break angular frequencies of $G_{ll3}(s)$ are initially halved compared with their initial values. Thus, the responses of $G_{ll1}(s)$, $G_{ll2}(s)$, and $G_{ll3}(s)$ contributes to the response of $G_{pc}(s) = G_{ll1}(s) \cdot G_{ll2}(s) \cdot G_{ll3}(s)$ at high-, middle-, and low angular frequencies, respectively. The values of the time constants of the lead-lag filters are provided in Table C.4 in Appendix C.
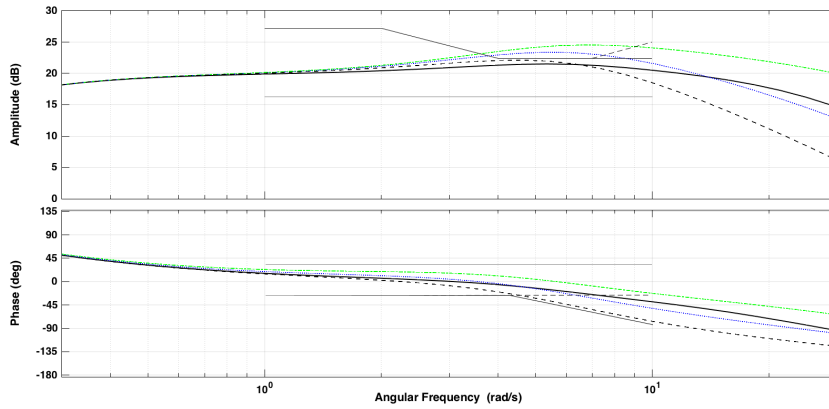
(a)
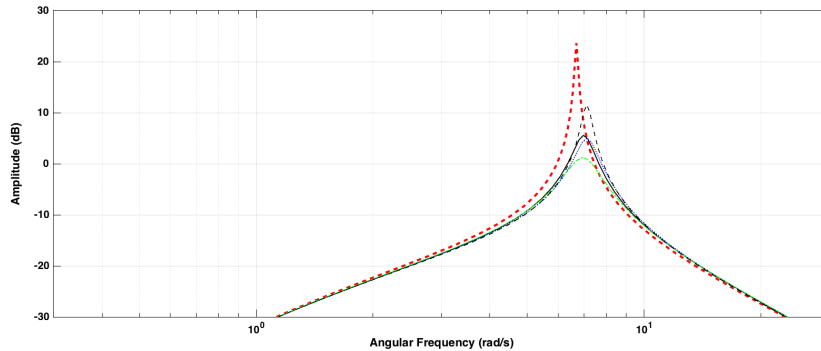
(b)

Fig. 5.15: Varying r after the break angular frequencies of $G_{ll1}(s)$ and $G_{ll3}(s)$ are initially doubled and halved, respectively. Solid: $r_0 = 2.941$; dashed: $r = 2$; blue dotted: $r = 2.941$; and green dash-dotted: $r = 5$. *(a)* FIKS-method. *(b)* NG-method. Red dashed: PSS disconnected.

In Fig. 5.15.(a), the initial effect of doubling the break angular frequencies of $G_{ll1}(s)$ and halving the break angular frequencies of $G_{ll3}(s)$ is to increase the amplitude characteristic partly beyond the upper amplitude limit. The effect becomes more pronounced as r is increased and less pronounced as r is decreased. The effects are again attributed to the fact that the response of the FIKS-method is an open-loop response. Thus, changes in the response of $G_{pc}(s)$ directly affect the response obtained by the FIKS-method.

In terms of the NG-method, comparing the solid and dotted curves in Fig. 5.15.(b) shows that the initial effect of doubling and halving the break angular frequencies of $G_{pc1}(s)$ and $G_{pc3}(s)$, respectively, is small in terms of the amplitude response around the resonance peak. However, as r is varied above 2.941 the amplitude response around the resonance peak is decreased. The effect of decreased amplitude response is mainly related to an improved open-loop phase characteristic that is associated with an increase in r above 2.941. As r is reduced below 2.941, the amplitude response around the resonance peak increases. The effect of increased amplitude response around the resonance peak for r below 2.941 is mainly caused by a worsening of the open-loop phase characteristic.

Fig. 5.16 illustrates the effects of varying r_3 after the break angular frequencies associated with $G_{ll3}(s)$ are initially halved compared with their initial values. Moreover, the break angular frequencies associated with $G_{ll1}(s)$ are doubled compared with their initial values, but the value of r_1 remains unaffected. Thus, r_3 is varied while $r_1 = 2.941$ and $r_2 = 2.941$. This allows for varying the response of $G_{ll3}(s)$ while keeping the responses of $G_{ll1}(s)$ and $G_{ll2}(s)$ unaffected. Thus, the effect of varying the response of $G_{pc}(s) = G_{ll1}(s) \cdot G_{ll2}(s) \cdot G_{ll3}(s)$ at low angular frequencies can be investigated. The values of the time constants are provided in Table C.5 in Appendix C.

Varying r_3 shows some effects on the responses obtained by both evaluation methods. In terms of the FIKS-method, Fig. 5.16.(a) shows that the amplitude limit is exceeded in the initial case where the break angular frequencies associated with $G_{ll3}(s)$ and $G_{ll1}(s)$ are halved and doubled, respectively. This is illustrated by the blue dotted response in Fig. 5.16.(a). If r_3 is increased to 5, the amplitude characteristic is further increased beyond the amplitude limit. The phase characteristic is also affected by the variation in r_3, but it remains inside the phase limits for all values of r_3. When r_3 is varied, the response of $G_{pc}(s)$ is affected at low angular frequencies. Thus, the response of the FIKS-method is directly affected by the variations in r_3.

In terms of the amplitude response obtained by the NG-method, the variations in r_3 affects the amplitude response around the resonance peak. An increase in r_3 from 2.941 to 5 yields reduced amplitude and is illustrated in Fig. 5.16.(b). The opposite is true for a reduction from 2.941 to 2. The main reason for the decreased amplitude response around the resonance peak when r_3 is increased from 2.941 to 5 is mainly due to an increase in the open-loop amplitude characteristic of the re-

sponse taken from the voltage reference deviation to the PSS output. On the other hand, the increase in amplitude response around the resonance peak when r_3 is decreased from 2.941 to 2 is mainly caused by a worsening of the open-loop phase characteristic.
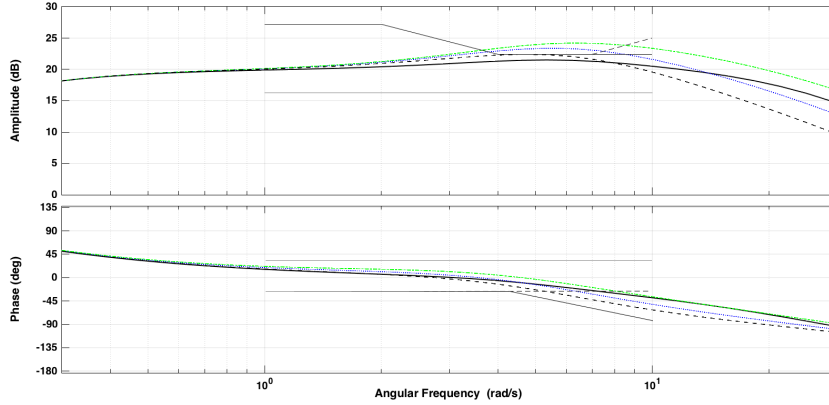
(a)
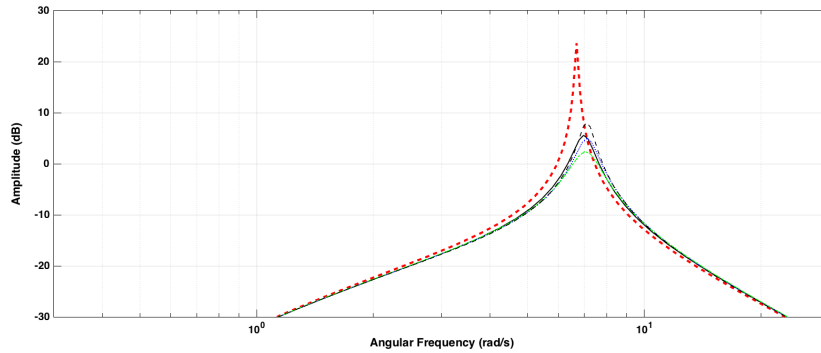
(b)

Fig. 5.16: Varying r_3 while keeping $r_1 = 2.941$ and $r_2 = 2.941$. Solid: $r_0 = 2.941$; dashed: $r_3 = 2$; blue dotted: $r_3 = 2.941$; and green dash-dotted: $r_3 = 5$. *(a)* FIKS-method. *(b)* NG-method. Red dashed: PSS disconnected.

5.5 Relations Between Responses of FIKS- and NG-Methods

This section investigates how changes in the response of the FIKS-method are reflected in the amplitude response obtained by the NG-method. Fig. 5.17 investigates the amplitude response obtained by the NG-method when the values of the parameters of the simplified PSS2B are varied to yield new phase characteristics of the FIKS-method that are below the reference phase characteristic. The values of the parameters of the simplified PSS2B are provided in Table C.6 in Appendix C.
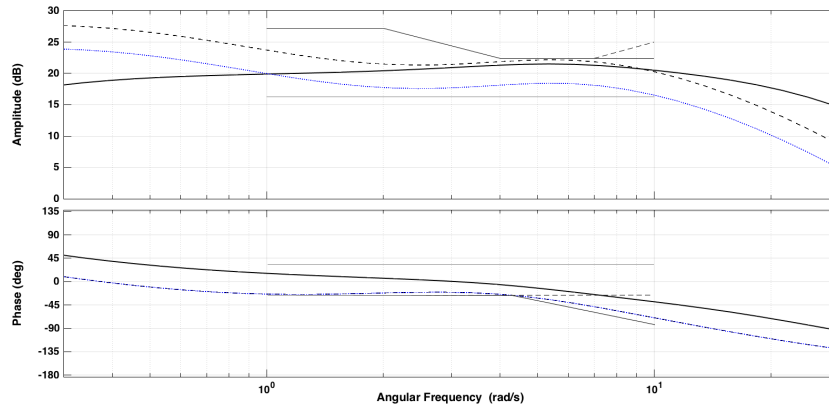
(a)
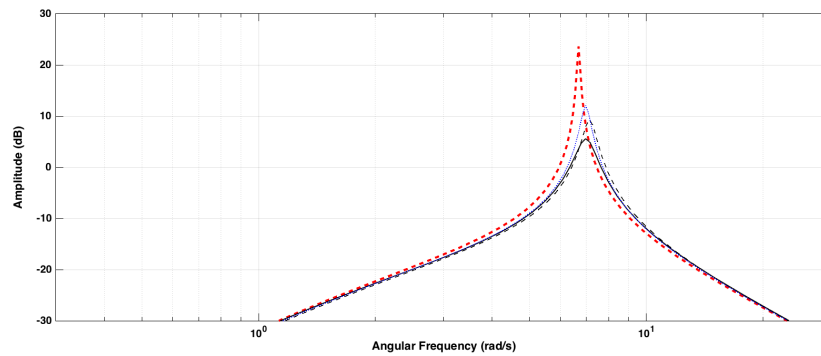
(b)

Fig. 5.17: New phase characteristics of the FIKS-method are below the reference phase characteristic. Solid: reference response; dashed: high amplitude characteristic; and blue dotted: low amplitude characteristic. *(a)* FIKS-method. *(b)* NG-method. Red dashed: PSS disconnected.

From Fig. 5.17, a new phase characteristic that is below the reference phase characteristic yields an increase in the amplitude response of the NG-method around the resonance peak. Furthermore, it can be seen that the amplitude characteristic affects the increase in the amplitude response of the NG-method around the resonance peak.

Fig. 5.18 investigates the amplitude response of the NG-method when the values of the parameters of the simplified PSS2B are varied in order to yield new phase characteristics of the FIKS-method that are above the reference phase characteristic. The values of the parameters of the simplified PSS2B are provided in Table C.7 in Appendix C.

The figure shows that in most cases where the new phase characteristics are above the reference phase characteristic result in a decrease in the amplitude responses of the NG-method around the resonance peak. It can also be seen that the amplitude characteristic of the FIKS-method affects the resulting amplitude response of the

NG-method around the resonance peak. In Fig. 5.18.(a), the blue dotted response corresponds to a slightly increased amplitude response in Fig. 5.18.(b). In Fig. 5.18.(b), the peak of the blue dotted amplitude response is slightly above the peak of the reference amplitude response even though the blue dotted phase characteristic is above the reference phase characteristic in Fig. 5.18.(a).
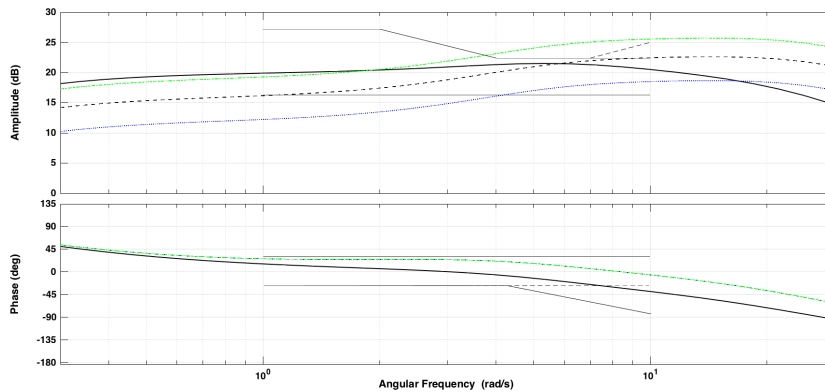
(a)
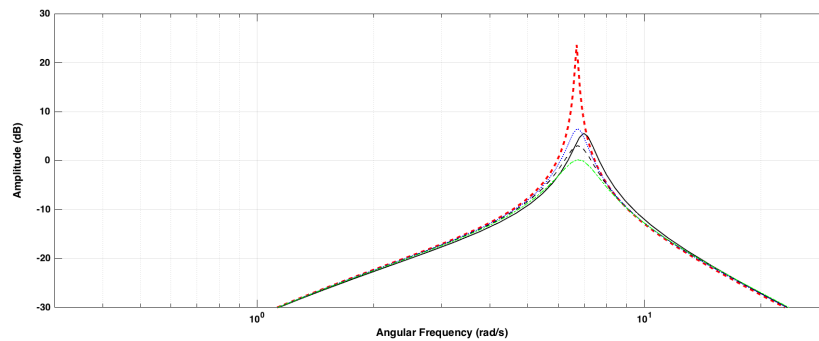
(b)

Fig. 5.18: New phase characteristics of the FIKS-method are above the reference phase characteristic. Solid: reference response; dashed: medium amplitude characteristic; blue dotted: low amplitude characteristic; and green dash-dotted: high amplitude characteristic. *(a)* FIKS-method. *(b)* NG-method. Red dashed: PSS disconnected.

5.6 Overview of Tested Combinations

Fig. 5.19 shows an overview of the combinations that are tested in the previous sections of this chapter. The figure shows the values of the amplitude and phase characteristics of the response of the FIKS-method for a specific angular frequency. This specific angular frequency is 6.689 rad/s and is equal to the angular frequency where the resonance peak with PSS disconnected occurs in Fig. 5.5.
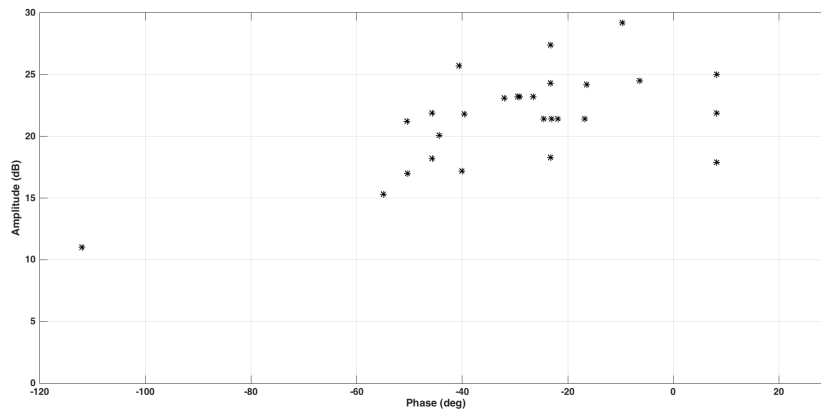
Fig. 5.19: Overview of the tested combinations.

From the figure it can be seen that the tested combinations are mostly located within 15 - 30 dB in terms of amplitude and within -55 - 10 deg in terms of phase.

6

Dynamic Simulations

The first section presents the results needed to verify the results from the linearized simulations. The second section presents the results from the dynamic simulations of the multi-bus power system. The stability performance of the PSS is also analyzed in connection to this.

6.1 Verification of Linearized Simulations

First, this section establishes the reference responses of the two evaluation methods. The second section verifies how changes in the response of the FIKS-method are reflected in the amplitude response of the NG-method.

6.1.1 Reference Responses

This section establishes the reference responses of the FIKS- and the NG-methods. The reference responses are the responses obtained by the two evaluation methods when the values of the parameters of the PSS2B are as given in Table 4.3.

Reference Response of FIKS-Method
Fig. 6.1 shows the response from the PSS output to the terminal voltage for offline-, loaded- ($P_e = 80$ MW), and lightly loaded operation of the SM ($P_e = 0.35$ MW).
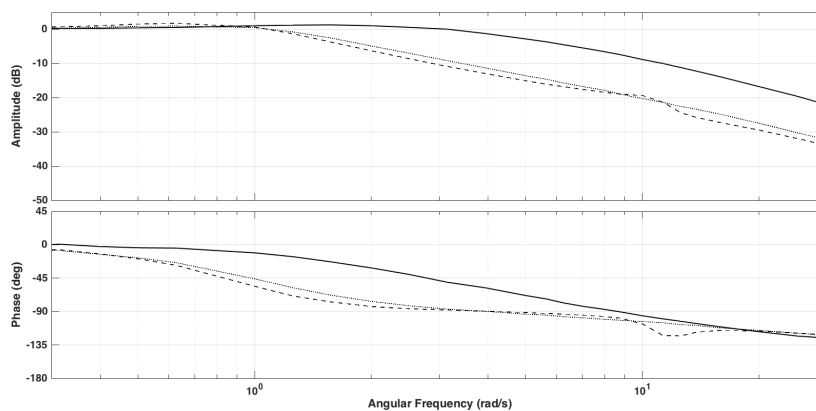
Fig. 6.1: Response from the PSS output to the terminal voltage for different operating conditions of the SM. Solid: offline, dashed: loaded, and dotted: lightly loaded.

Two things can be noticed in the figure: 1) the amplitude and phase characteristics are reduced as the SM turns from offline operation to loaded operation, and 2) the absence of the large peaks in the amplitude and the phase characteristics, as are visible in Fig. 5.1. Overall, the amplitude and phase characteristics in Fig. 6.1 are comparable to the amplitude and phase characteristics in Fig. 5.1.

Fig. 6.2 illustrates the reference response of the FIKS-method that corresponds to offline operation of the SM. For purposes of comparison, the figure also gives the responses obtained by the FIKS-method when the SM is operating under the same loaded conditions as in Fig. 6.1.
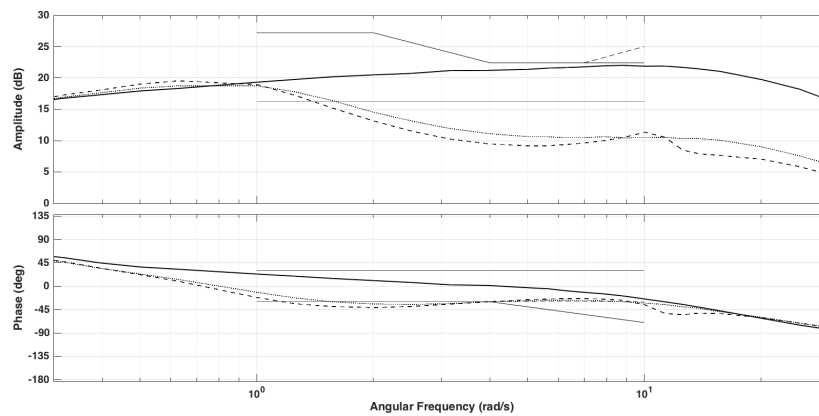
Fig. 6.2: Response obtained by the FIKS-method for different operating conditions of the SM. Solid: reference response (offline), dashed: loaded, and dotted: lightly loaded.

Reference Amplitude Response of NG-Method

Fig. 6.3 illustrates the reference amplitude response obtained by the NG-method. The figure also shows the amplitude response with the PSS disconnected.
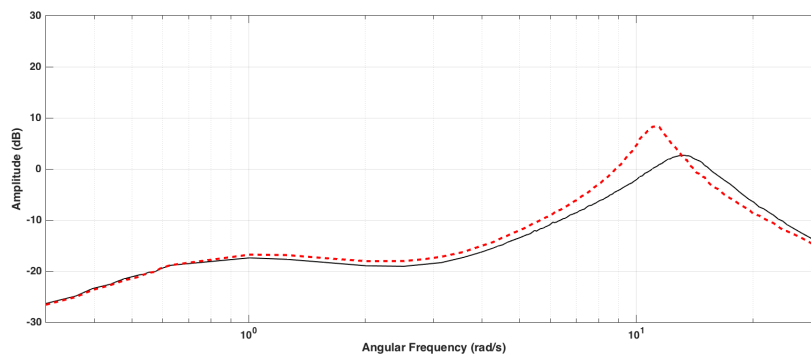
Fig. 6.3: Reference amplitude response obtained by the NG-method. Solid: PSS connected and red dashed: PSS disconnected.

The amplitude responses obtained by the NG-method in Fig. 6.3 show similar characteristics as the amplitude responses obtained by the NG-method in Fig. 5.5. However, two significant differences can be noticed in the comparison of the amplitude responses: 1) the angular frequencies where the resonance peaks occur differ in the two figures, and 2) the peaks values of the amplitude responses with PSS disconnected are significantly different in the two figures.

6.1.2 Relations Between Responses of FIKS- and NG-Methods

Fig. 6.4 shows the change in the amplitude response of the NG-method when the values of the parameters of the PSS2B are varied in order to yield new phase characteristics obtained by the FIKS-method that are below the reference phase characteristic of the FIKS-method. The values of the parameters of the PSS2B are given in Table C.8 in Appendix C.
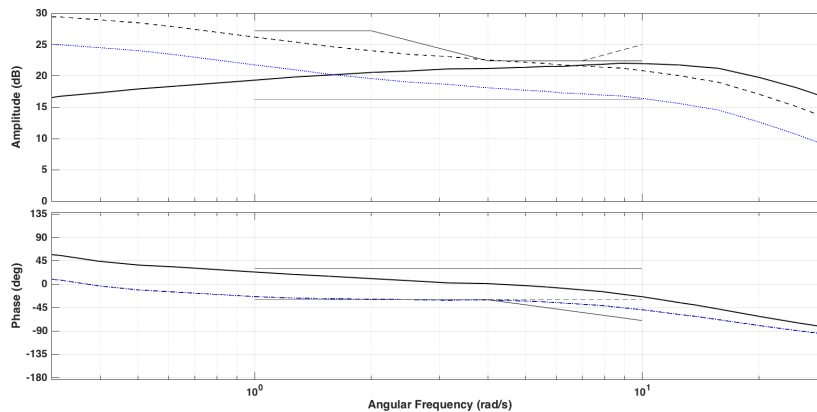

(a)
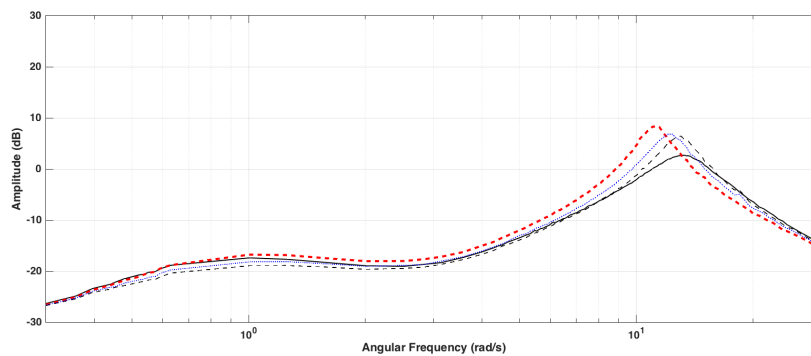
(b)

Fig. 6.4: New phase characteristics of the FIKS-method are below the reference phase characteristic. Solid: reference response; dashed: high amplitude characteristic; and blue dotted: low amplitude characteristic. *(a)* FIKS-method. *(b)* NG-method. Red dashed: PSS disconnected.

65

Fig. 6.4 shows that the amplitude response of the NG-method is increased around the resonance peak. Besides that, the amplitude characteristic of the FIKS-method affects the amount of increase in the amplitude response of the NG-method. The effects found in Fig. 6.4 are the same as the effects found in Fig. 5.17.

Fig. 6.5 shows how the amplitude response of the NG-method is changed when the values of the parameters of the PSS2B are varied so that the new phase characteristics of the FIKS-method are above its reference phase characteristic. The values of the parameters of the PSS2B are given in Table C.9 in Appendix C.
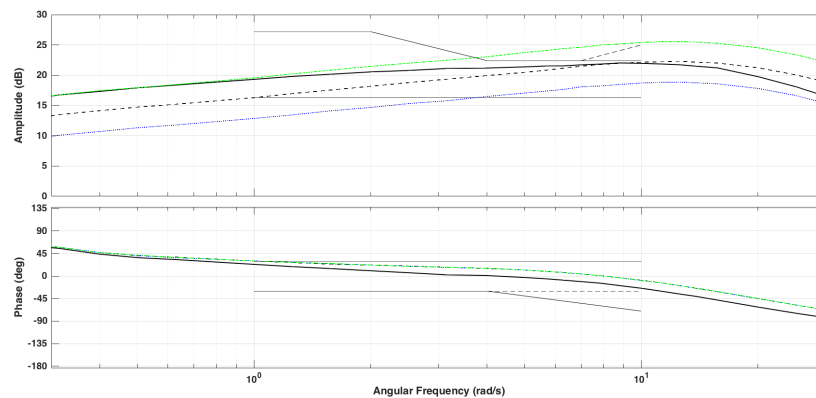
(a)
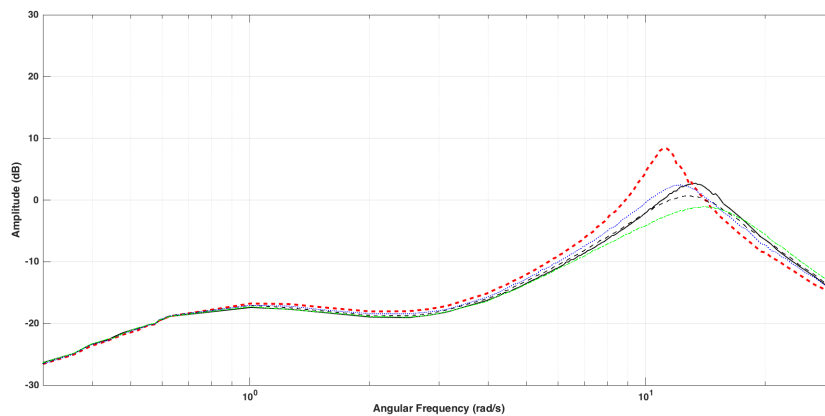
(b)

Fig. 6.5: New phase characteristics of the FIKS-method are above the reference phase characteristic. Solid: reference response; dashed: medium amplitude characteristic; blue dotted: low amplitude characteristic; and green dashdotted: high amplitude characteristic. *(a)* FIKS-method. *(b)* NG-method. Red dashed: PSS disconnected.

In the figure, the amplitude responses of the NG-method are reduced around the resonance peak. The decrease in the amplitude response is further affected by the amplitude characteristic of the FIKS-method. Thus, the effects seen in the figure are in large similar to the effects seen in Fig. 5.18. However, the peak of the blue

dotted response in Fig. 6.5.(b) is slightly below the peak of the reference amplitude response. This represents a difference compared with the case in Fig. 5.18.(b).

Fig. 6.6 shows the amplitude response of the NG-method when the new phase characteristics of the FIKS-method are significantly above the reference phase characteristic. The values of the parameters of the PSS2B are given in Table C.10 in Appendix C. The figure illustrates the same effects as found in Fig. 6.5; thus, the effects are in large similar to the effects seen in Fig. 5.18.
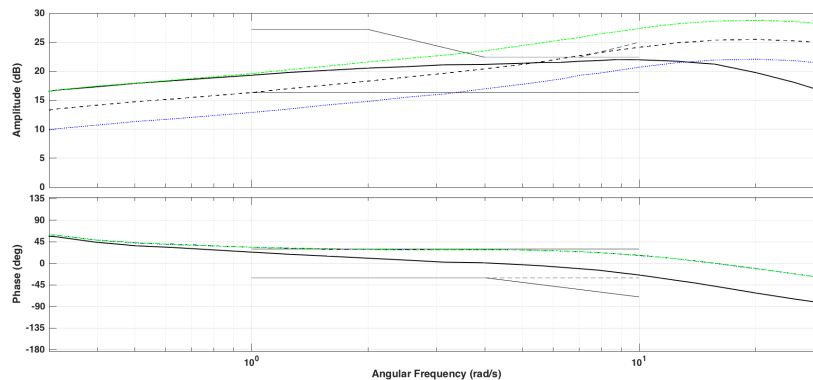

(a)
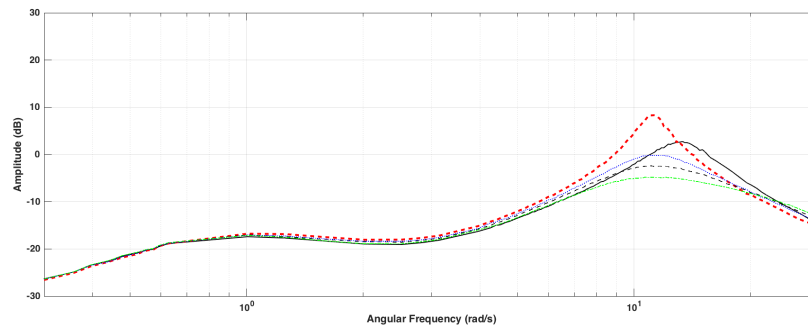
(b)

Fig. 6.6: New phase characteristics of the FIKS-method are significantly above the reference phase characteristic. Solid: reference response; dashed: medium amplitude characteristic; blue dotted: low amplitude characteristic; and green dash-dotted: high amplitude characteristic. *(a)* FIKS-method. *(b)* NG-method. Red dashed: PSS disconnected.

6.2 Multi-Bus Power System Simulations

This section presents the results from the dynamic simulations of the multi-bus power system where the PSS2Bs are tuned according to both evaluation methods. This is done with two different sets of tunings with different characteristics that are

referred to as tunings A and B. The motivation for doing this is that there are many ways in which a PSS2B can be tuned so that it is performing within the limits given by the two evaluation methods.

6.2.1 Replacing Synchronous Machines at Bus 4063

This section considers the case when the existing SM- and PSS-models at bus 4063 are replaced. It comprises two parts: one for each of tunings A and B.

Tuning the Power System Stabilizers with Tuning A
Fig. 6.7 shows the response of the FIKS-method when the PSS2Bs are tuned according to the FIKS-method. The figure also shows the amplitude response of the NG-method when the PSS2Bs are tuned according to the FIKS-method. The values of the parameters of the PSS2Bs are shown in Table A.7 in Appendix A.
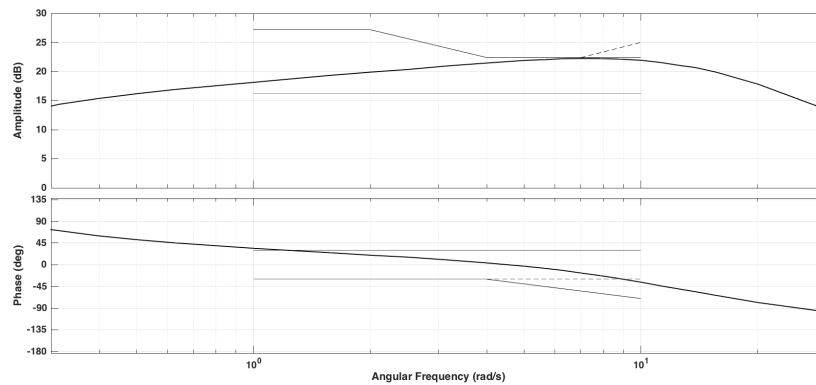
(a)
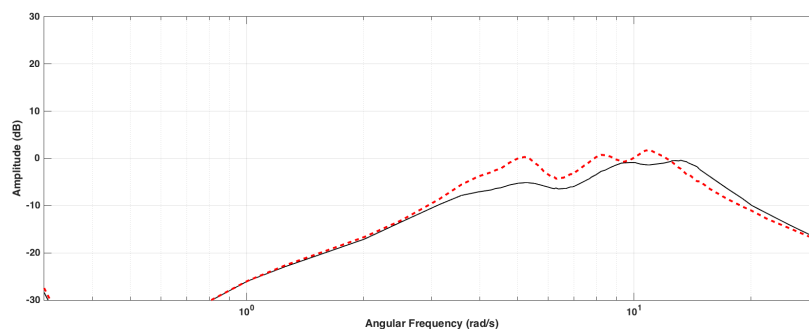
(b)

Fig. 6.7: PSS2Bs at bus 4063 are tuned according to the FIKS-method with tuning A. *(a)* FIKS-method. *(b)* NG-method. Solid: PSS connected and red dashed: PSS disconnected.

From the figure it is clear that the PSS2Bs are within the limits given by the FIKS-method. However, the PSS2Bs are improperly tuned according to the NG-method. This is due to that the amplitude response with PSS connected is over the amplitude response with PSS disconnected for angular frequencies above 12.4 rad/s.

Fig. 6.8 shows the amplitude response of the NG-method when the PSS2Bs are tuned according to the NG-method. It also shows the corresponding response of the FIKS-method when the PSS2Bs are tuned according to the NG-method. The values of the parameters of the PSS2Bs are shown in Table A.7 in Appendix A.
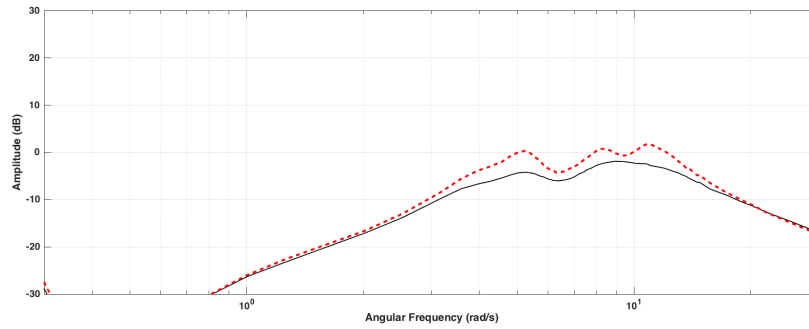
(a)
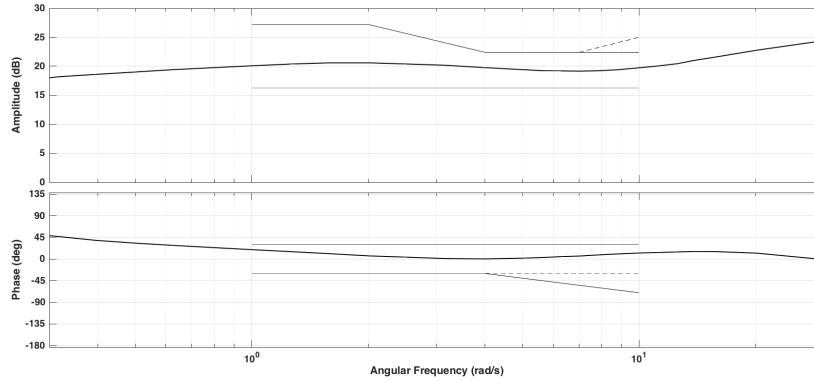
(b)

Fig. 6.8: PSS2Bs at bus 4063 are tuned according to the NG-method with tuning A. *(a)* NG-method. Solid: PSS connected and red dashed: PSS disconnected. *(b)* FIKS-method.

From the figure, tuning of the PSS2Bs according to the NG-method yields properly tuned PSS2Bs according to both evaluation methods. In order to make a fair comparison between the two evaluation methods, the amplitude characteristic in Fig. 6.7.(a) needs to be comparable to the amplitude characteristic in Fig. 6.8.(b) for angular frequencies in the range of 0.6 - 6.3 rad/s. The comparison of the amplitude characteristics shows that the two amplitude characteristics differ by a few decibels inside the relevant range of angular frequencies. This difference is acceptable.

Table 6.1 shows the lightly damped complex eigenvalues of the Nordic32-system when the PSS2Bs at bus 4063 are tuned according to each of the two evaluation methods. For purposes of comparison, the table also shows the lightly damped complex eigenvalues of the Nordic32-system when the PSS2Bs at bus 4063 are disconnected. The table only shows complex eigenvalues with imaginary parts in the range of 0.6 - 6.3 rad/s since these complex eigenvalues may represent inter-area modes of oscillation.

Table 6.1: Lightly damped complex eigenvalues when tuning the PSS2Bs at bus 4063 with tuning A

ID	No PSS		FIKS-Method		NG-Method	
	ω (rad/s)	ξ	ω (rad/s)	ξ	ω (rad/s)	ξ
O11	6.185	0.135	6.184	0.135	6.185	0.135
O12	5.795	0.150	5.804	0.153	5.802	0.152
O13	5.790	0.077	5.797	0.079	5.796	0.079
O14	5.381	0.101	5.449	0.172	5.393	0.151
O15	3.909	0.185	3.769	0.235	3.825	0.223

From the table, the most significant effect can be seen in the damping ratio of the complex eigenvalue O14 where tuning of the PSS2Bs according to the FIKS-method increases the damping ratio of the complex eigenvalue O14 by 70 % compared with PSS2Bs disconnected. For tuning of the PSS2Bs according to the NG-method, the increase in the damping ratio is 50 % compared with PSS2Bs disconnected. The second largest effect is seen in the damping ratio of O15 where tuning of the PSS2Bs according to the FIKS- and the NG-methods increases the damping ratio by 27 % and 21 %, respectively, compared with PSS2Bs disconnected.

The participation factors show that the SMs at bus 4063 are among the largest contributors to the complex eigenvalues O14 and O15; consequently, this explains the significant changes in the damping ratios of these complex eigenvalues. Furthermore, the SMs at bus 4063 contributes to a small extent to the complex eigenvalues O12 and O13 and explains the small increase in the damping ratios of these complex eigenvalues. Furthermore, the participation factors show that the SMs at bus 4063 does not contribute to the complex eigenvalue O11; hence, the damping ratio of this complex eigenvalue is unaffected.

Making a comparison between the responses of the FIKS-method shown in Figs. 6.7.(a) and 6.8.(b) it can be seen that the amplitude characteristic in Fig. 6.7.(a) is above the amplitude characteristic in Fig. 6.8.(b) at all angular oscillating frequencies of the complex eigenvalues shown in Table 6.1. Moreover, for the angular oscillating frequency of the complex eigenvalue O15 it can be seen that the phase characteristic in Fig. 6.7.(a) is above the phase characteristic in Fig. 6.8.(b). The opposite holds for the angular oscillating frequencies of the remaining complex eigenvalues O11 - O14.

Tuning the Power System Stabilizers with Tuning B

Fig. 6.9 shows the response of the FIKS-method when the PSS2Bs are tuned according to the FIKS-method. The figure also shows the corresponding amplitude response of the NG-method when the PSS2Bs are tuned according to the FIKS-method. The values of the parameters of the PSS2Bs are shown in Table A.8 in Appendix A.
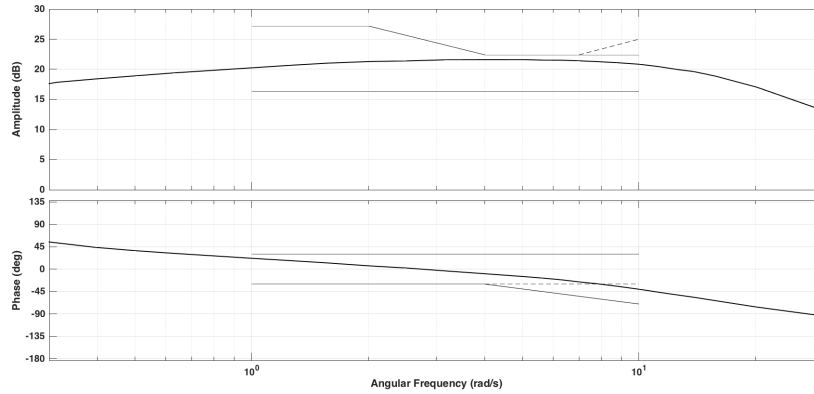
(a)
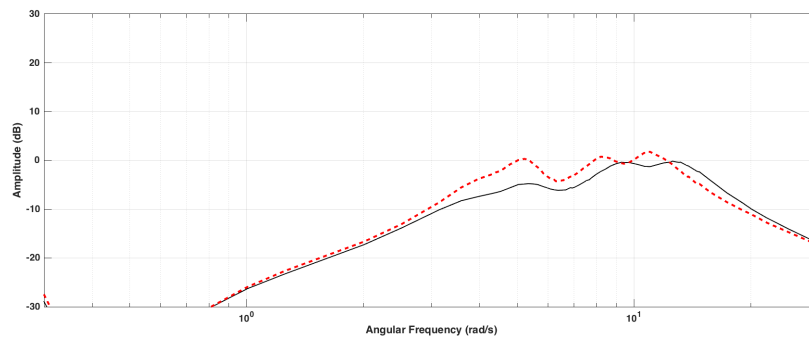
(b)

Fig. 6.9: PSS2Bs at bus 4063 are tuned according to the FIKS-method with tuning B. *(a)* FIKS-method. *(b)* NG-method. Solid: PSS connected and red dashed: PSS disconnected.

From the figure, it is clear that the response of the FIKS-method is inside the limits of the FIKS-method. Studying the amplitude response of the NG-method when the PSS2Bs are tuned according to the FIKS-method shows that the amplitude response of the NG-method with PSS2Bs connected is partly above the amplitude response of the NG-method with PSS2Bs disconnected; thus, the PSS2Bs are improperly tuned when evaluated with the NG-method. The amplitude response with PSS2Bs connected is above the amplitude response with PSS2Bs disconnected in the range of 9.2 - 9.7 rad/s as well as above 12.3 rad/s.

Fig. 6.10 shows the amplitude response of the NG-method when the PSS2Bs are tuned according to the NG-method. The figure also shows the response of the FIKS-method when the PSS2Bs are tuned according to the NG-method. The values of the parameters of the PSS2Bs are shown in Table A.8 in Appendix A.
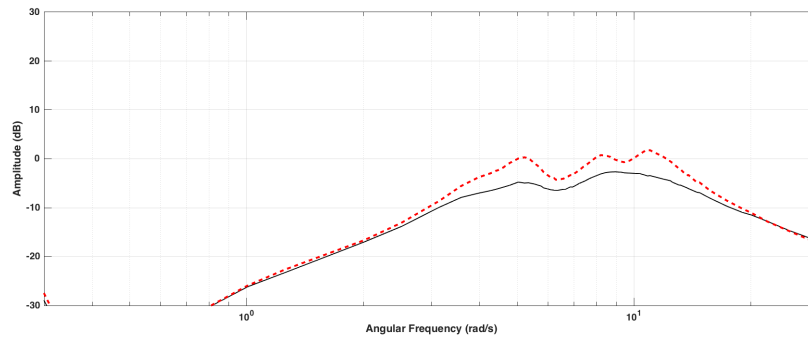
(a)
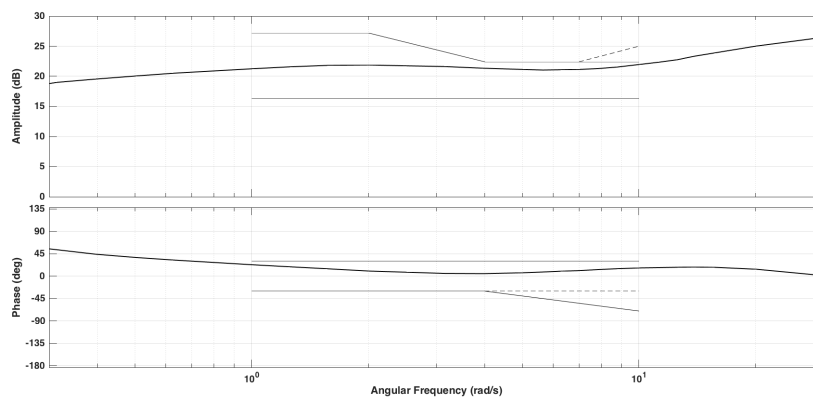
(b)

Fig. 6.10: PSS2Bs at bus 4063 are tuned according to the NG-method with tuning B. *(a)* NG-method. Solid: PSS connected and red dashed: PSS disconnected. *(b)* FIKS-method.

Studying Fig. 6.10, it is clear that the PSS2Bs are properly tuned when evaluated with both evaluation methods. Comparing the amplitude characteristics in Figs. 6.9.(a) and 6.10.(b), it can be seen that the two amplitude characteristics only differ by roughly 1 dB for angular frequencies in the range of 0.6 - 6.3 rad/s. Thus, the comparison between the two evaluation methods is fair.

Table 6.2 shows the lightly damped complex eigenvalues of the Nordic32-system when the PSS2Bs at bus 4063 are tuned according to each of the two evaluation methods as well as for disconnected PSS2B. Only complex eigenvalues with imaginary parts in the range of 0.6 - 6.3 rad/s are shown.

Table 6.2: Lightly damped complex eigenvalues when tuning the PSS2Bs at bus 4063 with tuning B

ID	No PSS ω (rad/s)	ξ	FIKS-Method ω (rad/s)	ξ	NG-Method ω (rad/s)	ξ
O11	6.185	0.135	6.184	0.135	6.185	0.135
O12	5.795	0.150	5.813	0.153	5.800	0.152
O13	5.790	0.077	5.799	0.079	5.795	0.079
O14	5.381	0.101	5.508	0.161	5.371	0.161
O15	3.909	0.185	3.828	0.236	3.800	0.229

The largest change in the damping ratio can be seen in the complex eigenvalue O14 where the damping ratio increases by 59 % for tuning of the PSS2Bs according to both evaluation methods. The second largest change in the damping ratio is seen in the complex eigenvalue O15. The damping ratio of the complex eigenvalue O15 increases by 28 % for tuning of the PSS2Bs according to the FIKS-method. When the PSS2Bs are tuned according to the NG-method, the damping ratio of the complex eigenvalue O15 increases by 24 %. For the complex eigenvalues O12 and O13, the increase in the damping ratios are in the neighborhood of 2 % for tuning of the PSS2Bs according to both evaluation methods. The damping ratio of the complex eigenvalue O11 is unaffected by the tuning of the PSS2Bs. The extent to which the damping ratios of the complex eigenvalues are affected can again be explained based on the participation factors. Here, the explanation presented in relation to Table 6.1 applies.

Studying the amplitude characteristics in Figs. 6.9.(a) and 6.10.(b) at the specific angular oscillating frequencies of the complex eigenvalues in Table 6.2, it can be seen that the amplitude characteristic in Fig. 6.9.(a) is slightly above the amplitude characteristic in Fig. 6.10.(b). This is true for all angular oscillating frequencies. Turning to the phase characteristics in Figs. 6.9.(a) and 6.10.(b) it can be seen that the phase characteristic in Fig. 6.10.(b) is above the phase characteristic in Fig. 6.9.(a) for all angular oscillating frequencies. The difference between the phase characteristics is smallest at the angular oscillating frequency of the complex eigenvalue O15. The difference increases with increasing angular oscillating frequency; consequently, it is largest at the angular oscillating frequency of the complex eigenvalue O11.

6.2.2 Replacing Synchronous Machine at Bus 4062

This section considers the case when the existing SM- and PSS-models at bus 4062 are replaced. The section comprises two parts: one for each of tunings A and B. The case where the PSS2B is tuned with tuning A is considered in the first part of this section. The case where the PSS2B is tuned with tuning B is considered in the second part of the section.

Tuning the Power System Stabilizer with Tuning A

Fig. 6.11 shows the response of the FIKS-method when the PSS2B is tuned according to the FIKS-method. The figure also shows the corresponding amplitude response of the NG-method when the PSS2B is tuned according to the FIKS-method. The values of the parameters of the PSS2B are shown in Table A.7 in Appendix A.
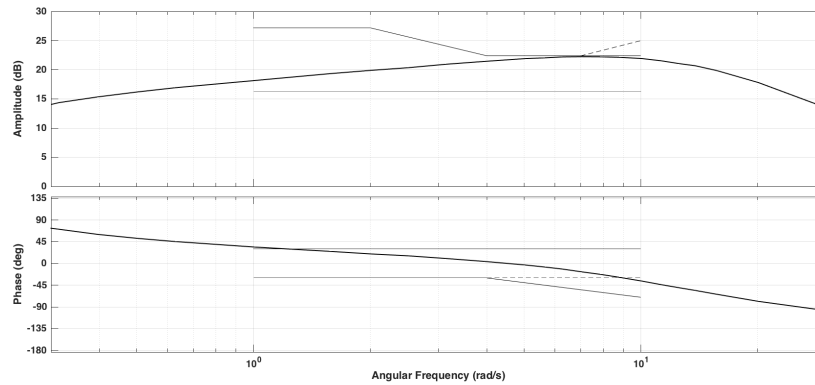

(a)
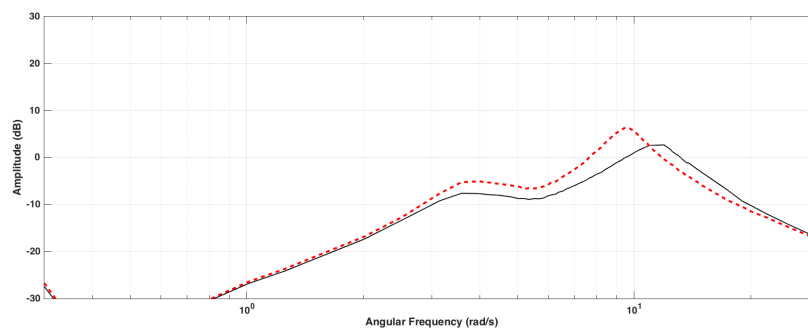
(b)

Fig. 6.11: PSS2B at bus 4062 is tuned according to the FIKS-method with tuning A. *(a)* FIKS-method. *(b)* NG-method. Solid: PSS connected and red dashed: PSS disconnected.

From the figure, it is clear that the PSS2B is properly tuned according to the FIKS-method. However, studying the amplitude response of the NG-method it can be seen that the PSS2B is improperly tuned according to the NG-method. This is due to the fact that the amplitude response with PSS connected is partly above the amplitude response with PSS disconnected. The crossing of the amplitude responses occurs at 11 rad/s.

Fig. 6.12 shows the amplitude response of the NG-method when the PSS2B is tuned according to the NG-method. The figure also shows the corresponding response of the FIKS-method. The values of the parameters of the PSS2B are shown in Table A.7 in Appendix A.

74
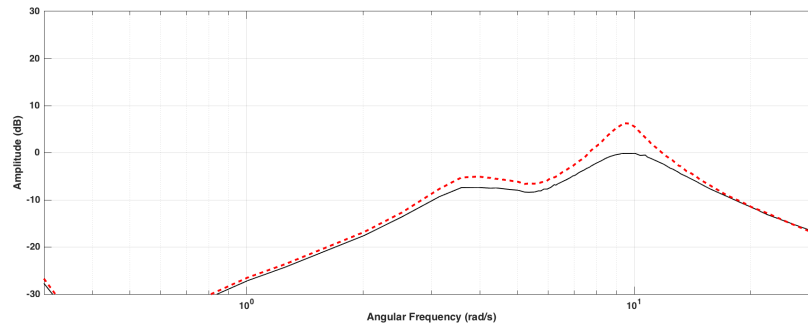
(a)
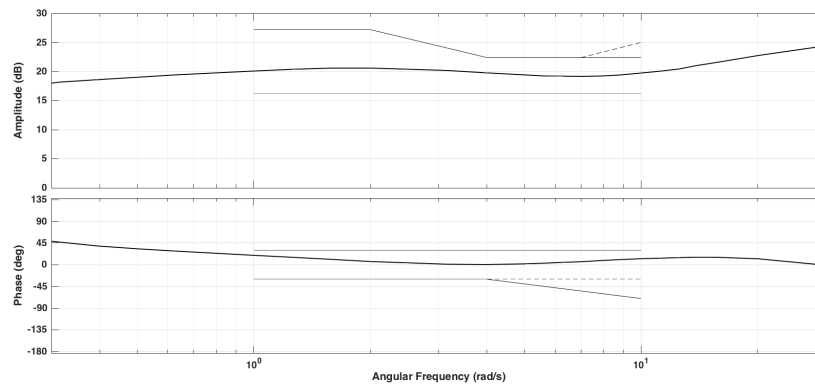
(b)

**Fig. 6.12:** PSS2B at bus 4062 is tuned according to the NG-method with tuning A. *(a)* NG-method. Solid: PSS connected and red dashed: PSS disconnected. *(b)* FIKS-method.

The figure shows that when the PSS2B is tuned with the NG-method it is also properly tuned when evaluated with the NG-method. In terms of the FIKS-method, the figure shows that when the PSS2B is tuned according to the NG-method it is also properly tuned when evaluated with the FIKS-method. Comparing the amplitude characteristic in Fig. 6.11.(a) with the amplitude characteristic in Fig. 6.12.(b), it is revealed that the difference between the amplitude characteristics is a few decibels for angular frequencies in the range of 0.6 - 6.3 rad/s. Thus, the comparison between the two evaluation methods is fair.

Table 6.3 shows the lightly damped complex eigenvalues of the Nordic32-system when the PSS2B at bus 4062 is tuned according to the FIKS-method. The table also shows the lightly damped complex eigenvalues of the Nordic32-system when the PSS2B is tuned according to the NG-method. For purposes of comparison, the table also shows the lightly damped complex eigenvalues of the Nordic32-system when the PSS2B at bus 4062 is disconnected. Only complex eigenvalues with imaginary parts in the range of 0.6 - 6.3 rad/s are considered.

Table 6.3: Lightly damped complex eigenvalues when tuning the PSS2B at bus 4062 with tuning A

ID	No PSS		FIKS-Method		NG-Method	
	ω (rad/s)	ξ	ω (rad/s)	ξ	ω (rad/s)	ξ
O21	6.184	0.135	6.184	0.135	6.184	0.135
O22	5.785	0.151	5.785	0.151	5.785	0.151
O23	5.784	0.080	5.784	0.080	5.784	0.080
O24	4.900	0.154	4.918	0.163	4.918	0.161
O25	3.694	0.169	3.642	0.199	3.656	0.195

The table shows that the damping ratios of the complex eigenvalues O21 - O23 are unaffected by tuning of the PSS2B according to both evaluation methods. However, the damping ratios of the complex eigenvalues O24 and O25 are affected by tuning of the PSS2B according to the two evaluation methods. The largest effect in terms of change in the damping ratio can be seen in the complex eigenvalue O25. Its damping ratio increases by 18 % when the PSS2B is tuned according to the FIKS-method compared with its damping ratio when the PSS2B is disconnected. When the PSS2B is tuned according to the NG-method, the damping ratio of complex eigenvalue O25 increases by 15 % compared with PSS2B disconnected. The increase in the damping ratio of the complex eigenvalue O24 is 6 % and 5 % for the FIKS- and the NG-methods, respectively, compared with the damping ratio when the PSS2B is disconnected.

The calculation of the participation factors shows that the SM at bus 4062 is one of many small contributors to the complex eigenvalues O24 and O25. The contribution to the complex eigenvalue O25 is larger than the contribution to the O24 complex eigenvalue, and this is also reflected in the larger increase in the damping ratio of the complex eigenvalue O25 compared with the increase in the damping ratio of complex eigenvalue O24. In addition, the participation factors show that the SM at bus 4062 does not contribute to the complex eigenvalues O21 - O23, and this is also revealed by the fact that the damping ratios of these complex eigenvalues are unaffected by the tuning of the PSS2B.

Tuning A considered in this part is the same as tuning A considered in the first part of Section 6.2.1. Hence, for the comparisons of the amplitude and phase characteristics in Figs. 6.11.(a) and 6.12.(b), the comparisons of the amplitude and phase characteristics in Figs. 6.7.(a) and 6.8.(b) applies. Thus, for further information the reader is referred to the first part in Section 6.2.1.

Tuning the Power System Stabilizer with Tuning B
Fig. 6.13 shows the response of the FIKS-method when the PSS2B is tuned according to the FIKS-mehtod. The figure also shows the amplitude response of the NG-method when the PSS2B is tuned to according to the FIKS-method. The values of the parameters of the PSS2B are shown in Table A.8 in Appendix A.
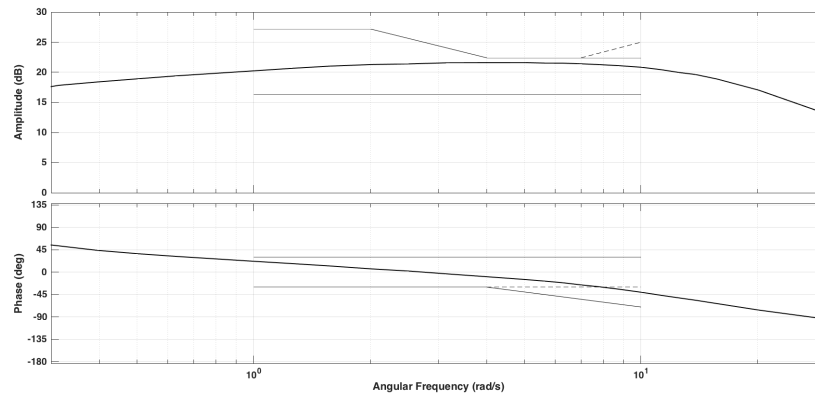
(a)
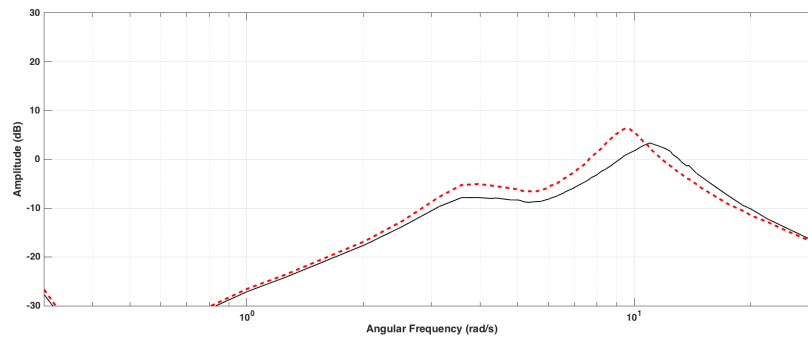
(b)

Fig. 6.13: PSS2B at bus 4062 is tuned according to the FIKS-method with tuning B. *(a)* FIKS-method. *(b)* NG-method. Solid: PSS connected and red dashed: PSS disconnected.

The figure shows that the response of the FIKS-method is inside the limits when the PSS2B is tuned according to the FIKS-method. However, in the case where the PSS2B is evaluated with the NG-method after being tuned according to the FIKS-method, it can be seen that the PSS2B is improperly tuned. This is due to the fact that the amplitude response of the NG-method with PSS2B connected is partly above the amplitude response of the NG-method with PSS2B disconnected. The amplitude response of the NG-method with PSS2B connected is above the amplitude response of the NG-method with PSS2B disconnected for angular frequencies above 10.7 rad/s.

Fig. 6.14 shows the amplitude response of the NG-method when the PSS2B is tuned according to the NG-method. In addition to this, the figure also shows the corresponding response of the FIKS-method when the PSS2B is tuned with the NG-method. The values of the parameters of the PSS2B are shown in Table A.8 in Appendix A.
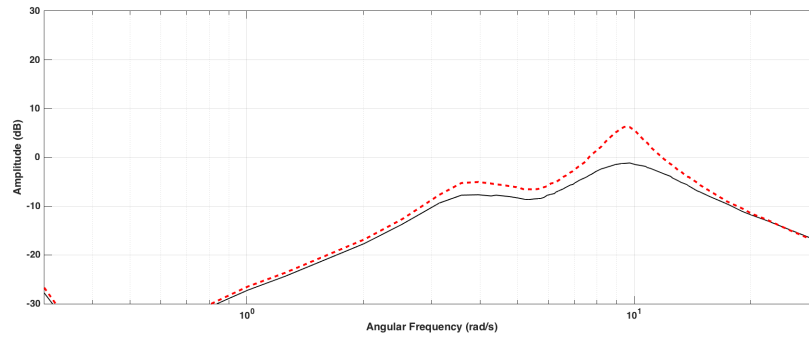
(a)
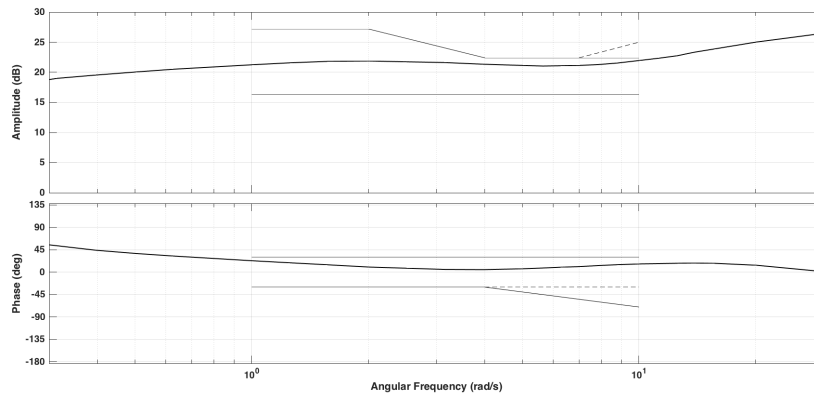
(b)

Fig. 6.14: PSS2B at bus 4062 is tuned according to the NG-method with tuning B. *(a)* NG-method. Solid: PSS connected and red dashed: PSS disconnected. *(b)* FIKS-method.

In terms of the NG-method, the figure shows that the amplitude response with PSS2B connected is below the amplitude response with PSS2B disconnected. Thus, the PSS2B is properly tuned according to the NG-method. In terms of the response of the FIKS-method when the PSS2B is tuned according to the NG-method, the figure shows that the PSS2B is properly tuned according to the FIKS-method. Comparing the amplitude characteristics in Figs. 6.13.(a) and 6.14.(b) it can be seen that the difference between the amplitude characteristics is in the range of 1 dB. Thus, this implies that the comparison between the two evaluation methods is fair.

Table 6.4 shows the lightly damped complex eigenvalues of the Nordic32-system when the PSS2B at bus 4062 is tuned according to the FIKS- and the NG-methods. For purposes of comparison, the table also shows the lightly damped complex eigenvalues of the Nordic32-system when the PSS2B at bus 4062 is disconnected. Table 6.4 only shows complex eigenvalues with imaginary parts in the range of 0.6 - 6.3 rad/s.

Table 6.4: Lightly damped complex eigenvalues when tuning the PSS2B at bus 4062 with tuning B

ID	No PSS		FIKS-Method		NG-Method	
	ω (rad/s)	ξ	ω (rad/s)	ξ	ω (rad/s)	ξ
O21	6.184	0.135	6.184	0.135	6.184	0.135
O22	5.785	0.151	5.785	0.151	5.785	0.151
O23	5.784	0.080	5.784	0.080	5.784	0.080
O24	4.900	0.154	4.918	0.163	4.918	0.163
O25	3.694	0.169	3.642	0.199	3.642	0.199

From the table it can be seen that the damping ratios of the complex eigenvalues O21 - O23 are unaffected by the tuning of the PSS2B. For tuning according to both the FIKS- and the NG-methods, the damping ratios of the complex eigenvalues O24 and O25 increase by 18 % and 6 %, respectively. The extent to which the SM at bus 4062 affects the damping ratios of the complex eigenvalues in the table can be explained based on the participation factors. The explanation given in relation to Table 6.3 applies, so the reader is referred there for future information regarding the participation factors.

Tuning B in this part is the same as tuning B in the second part of Section 6.2.1. Therefore, for comparisons of the amplitude and phase characteristics in Figs. 6.13.(a) and 6.14.(b), the reader is referred to the comparisons of the amplitude and phase characteristics in Figs. 6.9.(a) and 6.10.(b). These comparisons are presented in the second part of Section 6.2.1.

7
Discussion

The first section of this chapter discusses the results from the simulations of the linearized model of the SMIB-system. The following section discusses the results from the dynamic simulations of the SMIB- and multi-bus-systems. The third section provides some suggestions for future work based on the findings of the report. The chapter concludes with discussing the findings of the report in a somewhat wider perspective.

7.1 Linearized Simulations

From Sections 5.2 - 5.5, it is clear how changes in the values of the parameter of the simplified PSS2B affect the response obtained by the FIKS-method. In case of the more complex amplitude response obtained by the NG-method, the open-loop response characteristic taken from the voltage reference deviation to the PSS output is used to investigate the reasons behind the changes in the amplitude response of the NG-method. However, it is desirable to investigate if it is possible to directly relate the changes in the response of the FIKS-method to the changes in the amplitude response of the NG-method.

Studying the effects of varying the values of the parameters of the simplified PSS2B that are illustrated in Figs. 5.6 - 5.18, there seems to be a rough relation between the changes in the responses of the two evaluation methods. For the cases studied, a certain parameter variation that yields a new phase characteristic of the FIKS-method that is above the reference phase characteristic of the FIKS-method tends to reduce the amplitude response of the NG-method around the resonance peak. A certain parameter variation that yields a new phase characteristic of the FIKS-method that is below the reference phase characteristic of the FIKS-method tends to increase the amplitude response of the NG-method around the resonance peak. This is seen in the cases studied, and some illustrative examples are provided in Figs. 5.10, 5.12, 5.14, 5.17, and 5.18.

There are cases where the amplitude response of the NG-method is slightly decreased compared with the reference amplitude response even though the new phase characteristic obtained by the FIKS-method is slightly below the reference phase characteristic of the FIKS-method. Such cases can be found in Figs. 5.15 and 5.16. This is due to the well known fact that the gain of the PSS influences the damping provided by the PSS.

7.2 Dynamic Simulations

This section first discusses the verification of the linearized simulations. In the second section are the results from the dynamic simulations of the multi-bus power system discussed.

7.2.1 Verification of Linearized Simulations

Comparing Figs. 5.1 and 5.3 with Figs. 6.1 and 6.2 it is clear that the results from the dynamic simulations show comparable characteristics to the results from the linearized simulations. It is believed that the larger amount of inherent damping present in the dynamic model of the SMIB-system compared with the linearized model of the SMIB-system is mainly due to the differences in the layouts of the SMIB-systems. Including the damper windings in the model of the SM should have an influence on the inherent damping of the SMIB-system. This effect is accounted for in the used dynamic SM-model but not in the used linearized SM-model.

The differences in the inherent damping of the two SMIB-systems are visible when comparing Figs. 6.3 and 5.5, and it is the cause for the large differences in the amplitude responses around the resonance peaks with PSS disconnected. Furthermore, the doubling of the angular frequency where the resonance peak occurs in Fig. 6.3 compared with the angular frequency where the resonance peak occurs in Fig. 5.5 is also caused by the differences in the layouts of the SMIB-systems. This stated difference in terms of the amplitude response with PSS disconnected can also be seen when comparing Figs. 6.4.(b) and 6.5.(b) with Figs. 5.17.(b) and 5.18.(b).

In Figs. 6.5.(a) and 6.6.(a), the blue dotted responses showing the response of the FIKS-method with low amplitude characteristic yields a slightly reduced peak of the amplitude responses in Figs. 6.5.(b) and 6.6.(b) compared with the peak of the reference amplitude response. This is not seen Fig. 5.18.(b) where the the peak of the blue dotted amplitude response is increased slightly compared with the peak of the reference amplitude response. This represents a small difference between the results from the linearized and dynamic simulations; however, the findings of the linearized simulations are in large verified by the findings of the dynamic simulations.

7.2.2 Multi-Bus Power System Simulations

The amplitude and phase characteristics of the FIKS-method when the PSS2Bs are tuned according to the FIKS- and the NG-methods with tuning A can be seen in Figs. 6.7.(a) and 6.8.(b), respectively, and they can also be seen in Figs. 6.11.(a) and 6.12.(b). The comparison between the phase characteristics of the FIKS-method shown in Figs. 6.7.(a) and 6.8.(b) shows that the phase characteristic in Fig. 6.7.(a) is above the phase characteristic in Fig. 6.8.(b) for angular frequencies below 4 rad/s. The opposite is true for angular frequencies above 4 rad/s. Obviously, the same result is found if the phase characteristics in Figs. 6.11.(a) and 6.12.(b) are compared.

The same comparison can be performed between the phase characteristics of the FIKS-method when the PSS2Bs are tuned according to the FIKS- and the NG-methods with tuning B, which can be seen in Figs. 6.9.(a) and 6.10.(b). The same phase characteristics of the FIKS-method can be seen in Figs. 6.13.(a) and 6.14.(b). The comparison reveals that the phase characteristic in Fig. 6.10.(b) is slightly above the phase characteristic in Fig. 6.9.(a) for angular frequencies below 3 rad/s, and the difference increases as the angular frequency increases. Thus, the situation is the opposite compared with the phase characteristics in Figs. 6.7.(a) and 6.8.(b) where the PSS2Bs are tuned according to the FIKS- and the NG-methods with tuning A.

The fact that the order of the phase characteristics of the FIKS-method are the opposite when the PSS2Bs are tuned with tunings A and B as pointed out in the previous discussion is important. It is possible to vary the responses of the two evaluation methods in various ways and still make them appear inside the limits given by the two evaluation methods. This is especially true for the NG-method. The fact that the order of the phase characteristics is the opposite when the PSS2Bs are tuned according to tunings A and B shows that tunings A and B are not too similar. This adds robustness to the findings. Furthermore, in Sections 6.2.1 and 6.2.2 it is shown that the comparisons between the two evaluation methods are fair, and this adds trustworthiness to the findings in Section 6.2.

Tables 6.1 and 6.3 show the complex eigenvalues when the PSS2Bs at buses 4063 and 4062 are tuned according to both evaluation methods with tuning A. Studying the changes in the damping ratios of the complex eigenvalues in the tables it is clear that when the damping ratios change, tuning of the PSS2Bs according to the FIKS-method yields higher increase in the damping ratios than tuning of the PSS2Bs according to the NG-method does. This is true for all but one complex eigenvalue, namely the complex eigenvalue O13 in Table 6.1 where the increase in its damping ratio is the same for tuning of the PSS2Bs according to both evaluation methods.

Tables 6.2 and 6.4 show the complex eigenvalues when the PSS2Bs at buses 4063 and 4062 are tuned according to both evaluation methods with tuning B. The comparison between the damping ratios of the complex eigenvalues in Tables 6.2 and 6.4 reveal that tuning of the PSS2Bs according to both evaluation methods yield the same increase in the damping ratios. This is true for all complex eigenvalues except for the complex eigenvalues O12 and O15 in Table 6.2 where the increase in their damping ratios are larger when the PSS2Bs are tuned according to the FIKS-method compared with tuning of the PSS2Bs according to the NG-method.

To summarize the above, it is clear that when the damping ratios of the complex eigenvalues in Tables 6.1 - 6.4, tuning of the PSS2Bs according to the FIKS-method results in a larger increase in the damping ratios of the complex eigenvalues compared with tuning of the PSS2Bs according to the NG-method.

7.3 Future Work

This section discusses some suggestions for future work based on the findings of the study. The purpose of the suggestions for future work are threefold: 1) to further increase the understanding of the two evaluation methods and their relationship, 2) to further verify the results from the linearized simulations by dynamic simulations, and 3) to increase the generalizability of the findings of this study.

The linearized model of the SMIB-system is a widely recognized model, and it has been used in research previously. The model is sufficient for investigating basic concepts even though it does not properly account for the effects of damper windings other than through the damping factor K_D. The model shows reasonable and expected behavior during the simulations, but the model is very lightly damped. The coefficients $K_1, \ldots, K_6$ and the field circuit time constant are dependent on the current operating condition as well as the parameter values of the SM. In addition, the effects of magnetic saturation also affect the values of the coefficients and the field circuit time constant. This may affect the generalizability of the results obtained by the linearized simulations to some extent. Thus, a suggestion for future work is:

- Investigate how different operating conditions and/or how the effects of magnetic saturation affect the responses obtained by the two evaluation methods through further simulations of the linearized SMIB-system. In addition to this, it should also be investigated how different operation conditions and/or the inclusion of magnetic saturation affect the way in which changes in the response of the FIKS-method are reflected in the amplitude response of the NG-method.

The model of the excitation system and in particular the model of the PSS implemented into the linearized model of the SMIB-system and the dynamic models of the SMIB- and multi-bus power system are likely to affect the responses obtained by the two evaluation methods. This may further affect the generalizability of the results to some extent. Thus another suggestion for future work is:

- Through both linearized and dynamic simulations, investigate if, and also possibly how, different models of the excitation system and PSS affect the responses of the two evaluation methods. Subsequently, also investigate if and how different models of the excitation system and PSS affect how changes in the response of the FIKS-method are reflected in the amplitude response of the NG-method.

Figs. 5.17 and 5.18 illustrates how changes in the response of the FIKS-method are reflected in the amplitude response of the NG-method. This relation may be further investigated as pointed out previously; however, a more theoretical approach may be taken by trying to establish a mathematical relationship between the responses of the two evaluation methods. Thus, a third suggestion for future work is:

- Establish a mathematical relationship between the responses of the two evaluation methods. It is believed that this may be done by starting with obtaining the transfer function of the block diagram shown in Fig. 5.2; then, try to relate this transfer function to the transfer function of the open-loop system from voltage reference deviation to the PSS output. Finally, relate this to the closed-loop amplitude response of the NG-method.

The Nordic32-system is a power system model that mimics large parts of the Nordic power system, and the model has been used in various studies. The fact that the Nordic32-system mimics the Nordic power system is not very important; rather, the importance lies in the fact that the model captures many types of oscillation modes. Thus, the Nordic32-system is suitable for purposes of analyzing the stability performance of the PSS.

The analysis of the stability performance of the PSS is based on the comparison between the damping ratios of the complex eigenvalues of the Nordic32-system obtained with PSSs disconnected and PSSs connected. This makes sure that the changes in the damping ratios are only caused by the differences in PSS tuning, rather than being caused by the actual replacements of the existing SM- and PSS-models.

The above discussion suggests that the results from the dynamic simulations are reliable; however, they may not be fully generalizable to hold for any PSS in any SM. Hence, a suggestion for future work is:

- Model a real power system during operating conditions where measurements have shown that the FIKS- and the NG-methods do not agree. Then, the stability performance of the PSS is to be analyzed.

Tunings A and B show somewhat different characteristics, and it could be desirable to investigate the effect of increasing the differences in the characteristics even more. Therefore, it is suggested that:

- Varying the values of the parameters of the PSS2Bs in order to make the difference in the order of the phase characteristics of the FIKS-method obtained when the PSS2Bs are tuned with tunings A and B more pronounced when the PSS2Bs are evaluated with each of the two evaluation methods.

In this study, the PSS2Bs are tuned according to the two evaluation methods and the stability performance of the PSSs is then analyzed. To gain further understanding of the two evaluation methods, it would be possible to reverse this process. Thus, a final suggestion for future work is:

- Tune the PSSs for optimal stability performance by using eigenvalue-placement techniques. Then, the corresponding responses in terms of the responses obtained by the FIKS- and the NG-methods are to be studied.

7.4   Implications on Ethics and Sustainability

The possible disagreement between the two evaluation methods may imply that PSSs connected to the power system is not functioning properly. If this is the case, this may cause stability problems in the power system that may evolve into outages. If proper action is not taken, such a situation may lead to blackouts potentially paralyzing cities, regions, countries, or parts of continents. Such a situation may result in huge economical costs for the society and it may also cause harm to both people and the environment. The same risk can be identified in the case when new PSSs are to be connected to the power system since the stability performance of the PSS may be evaluated with an evaluation method that does not guarantee the proper functioning of the PSS. The nature of this problem is ethical, but the different parties may be unaware of the fact that their current evaluation method may not be performing as believed. It is believed that the problem can be partly or fully avoided if one of the two evaluation methods can be widely established as the better to use when evaluating the stability performance of a PSS.

The power system is facing the challenge of adapting to increasing energy demands worldwide. At the same time, the concern for the environment has brought about increasing demands on power generation where decreased usage of fossil fuels in power generation is demanded. Increased usage of RES is regarded as a feasible solution to the challenge of decreasing the usage of fossil fuels, and power system stability is one of the prerequisites for succeeding with the integration of RES. Thus, the PSS may have an important role in the process of ensuring the stability of the power system.

In the short term, the findings of this study primarily provides a basis for future studies. In the long term, the findings of this study together with the findings of future studies may broadly establish that one of the two evaluation methods is better to use when evaluating the stability performance of PSSs. Thus, in the long term, the implications of the findings of this study are believed to contribute towards the successful integration of RES. In addition to this, it is also believed that the findings of this study can contribute towards reducing the identified ethical problem.

Furthermore, additional implications of the findings of this study can be found in the long term and may go beyond the demand of decreasing the need for fossil fuels in power generation. The integration of RES brings additional positive effects in terms of sustainable development. Reduced usage of fossil fuels in power generation helps in managing the natural resources for future generations since today's demand on these resources may decrease. Moreover, increased usage of RES is believed to bring various job opportunities worldwide.

8
Conclusion

The simulations of the linearized model of the SMIB-system show that the change in amplitude response obtained with the NG-method is primarily related to the change in phase characteristic of the response obtained by the FIKS-method. It is shown that the new amplitude response of the NG-method decreases relative to its reference amplitude response when the new phase characteristic of the FIKS-method is above the reference phase characteristic of the FIKS-method. Moreover, the simulations also indicate that a change in the amplitude characteristic of the FIKS-method affects the change in the amplitude response of the NG-method.

The dynamic simulations support the findings of the linearized simulations in terms of how changes in the response of the FIKS-method are reflected in the amplitude response of the NG-method. Furthermore, for the simulated PSS locations where the PSS2Bs are tuned according to both evaluation methods with tunings A and B, the eigenvalue analysis shows that tuning of the PSS2Bs according to the FIKS-method generally yields higher increases in the damping ratios of the complex eigenvalues with imaginary parts in the range of $0.6 - 6.3$ rad/s compared with the increases in the damping ratios of the same complex eigenvalues when the PSS2Bs are tuned according to the NG-method. This infers that the stability performance of the PSS2Bs is better when the FIKS-method is utilized for tuning of the PSS2Bs. Consequently, this suggests that the FIKS-method should be used in front of the NG-method for purposes of evaluating the stability performance of a PSS.

In the short term, the findings of this study provides a basis for future studies. In the long term, the combined findings of this and future studies may broadly establish that one of the two evaluation methods is better to use when evaluating the stability performance of a PSS. It is recommended that future work is focused towards increasing the understanding of the two evaluation methods, and future work should also focus towards increasing the generalizability of the findings of this study. The former can be achieved through: further investigating how model changes affect the responses obtained by the two evaluation methods, and also by establishing a mathematical relationship between the responses obtained by the two evaluation methods. The latter can be achieved through the modeling and simulation of real power systems where measurements have shown that the two evaluation methods does not agree.

Bibliography

[1] J. D. McDonald, B. Wojszczyk, B. Flynn, and I. Voloh, "Distribution systems, substations, and integration of distributed generation", in *Electrical Transmission Systems and Smart Grids: Selected Entries from the Encyclopedia of Sustainability Science and Technology*, M. M. Begovic, Ed., New York, NY, USA: Springer, 2013, 7–68. [online]. Available: http://link.springer.com.proxy.lib.chalmers.se/book/10.1007%2F978-1-4614-5830-2.

[2] N. L. Panwar, S. C. Kaushik, and S. Kothari, "Role of renewable energy sources in environmental protection: A review", *Renewable Sustainable Energy Rev.*, vol. 15, no. 3, pp. 1513–1524, Apr. 2011. [online]. Available: http://www.sciencedirect.com.proxy.lib.chalmers.se/science/article/pii/S1364032110004065?np=y&npKey=857d09eaf75a318d9c99cacf7db62fc3fc6bfcdf30d25f7645a3c598e4ee6833.

[3] E. Ciapessoni, D. Cirio, A. Gatti, and A. Pitto, "Renewable power integration in sicily: Frequency stability issues and possible countermeasures", *In 2013 IREP Symp. Bulk Power Syst. Dynamics Control - IX Optimization, Security Control Emerging Power Grid*, pp. 1–7, [online]. Available: http://ieeexplore.ieee.org.proxy.lib.chalmers.se/stamp/stamp.jsp?arnumber=6629350.

[4] N. G. Hingorani and L. Gyugyi, *Understanding FACTS: Concepts and technology of flexible AC transmission systems*, 1st ed. Piscataway, NJ, USA: IEEE Press, 1999.

[5] F. Nieuwenhout, J. Dogger, and R. Kamphuis, "Electricity storage for distributed generation in the built environment", *In 2005 Int. Conf. Future Power Syst.*, pp. 1–5, [online]. Available: http://ieeexplore.ieee.org.proxy.lib.chalmers.se/document/1600473/.

[6] G. Andersson, *Modelling and Analysis of Electric Power Systems.* 2008. [online]. Available: http://www.123seminarsonly.com/Seminar-Reports/039/84968234-Modeling-and-Analysis-of-Electric-Power-Systems.pdf.

[7] H. Saadat, *Power System Analysis*, 3rd ed. Milwaukee, WI, USA: PSA Publishing, 2010.

[8] N. Magaji and B. Umar, "Application of power system stabilizer on stability studies", *Appl. Mech. Materials*, vol. 793, pp. 149–153, Sep. 2015. [online]. Available: http://search.proquest.com .proxy.lib.chalmers.se/docview/1716396 121?pq-origsite=summon.

[9] C. Concordia, "Steady-state stability of synchronous machines as affected by voltage-regulator characteristics", *Elect. Eng.*, vol. 63, no. 5, pp. 215–220, May 1944. [online]. Available: http://ieeexplore.ieee.org.proxy.lib.chalmers.se/ stamp/stamp.jsp?arnumber=6440257.

[10] E. Halyes and G. Raja, "Evaluation of methods for improving and testing power system stabilizers in reciprocating engines", Master's thesis, Dept. Energy and Environment, Chalmers Univ. Technol., Gothenburg, Sweden, 2016. [online]. Available: http://studentarbeten.chalmers.se/publication/243605-eval uation-of-methods-for-improving-and-testing-power-system-stabilizers-in-reciprocating-engines.

[11] Statnett, "Funksjonskrav i kraftsystemet," 2012. [online]. Available: http:// www.statnett.no/Global/Dokumenter/Kraftsystemet/Systemansvar/ FIKS%202012.pdf.

[12] National Grid, "The Grid Code," Issue 5, Revision 20, 2017. [online]. Available: http://www2.nationalgrid.com/UK/Industry-information/Electricity-codes/ Grid-code/The-Grid-code/.

[13] V. Keumarsi, M. Simab, and G. Shahgholian, "An integrated approach for optimal placement and tuning of power system stabilizer in multi-machine systems", *Int. J. Elect. Power Energy Syst.*, vol. 63, pp. 132–139, Dec. 2014. [online]. Available: http://www.sciencedirect.com.proxy.lib.chalmers.se/science/ article/pii/S0142061514003433?_rdoc=1&_fmt=high&_origin=gateway&_ docanchor=&md5=b8429449ccfc9c30159a5f9aeaa92ffb&ccp=y.

[14] L. H. Hassan, M. Moghavvemi, H. A. F. Haider, K. M. Muttaqi, and V. G. Ganapathy, "Optimization of power system stabilizers using participation factor and genetic algorithm", *Int. J. Elect. Power Energy Syst.*, vol. 55, pp. 668–679, Feb. 2014. [online]. Available: http://www.sciencedirect.com.proxy.lib. chalmers.se/science/article/pii/S0142061513004432?_rdoc=1&_fmt=high&_ origin=gateway&_docanchor=&md5=b8429449ccfc9c30159a5f9aeaa92ffb.

[15] A. Khodabakhshian and R. Hemmati, "Multi-machine power system stabilizer design by using cultural algorithms", *Int. J. Elect. Power Energy Syst.*, vol. 44, no. 1, pp. 571–580, Jan. 2013. [online]. Available: http://www.sciencedirect.com. proxy.lib.chalmers.se/science/article/pii/S0142061512004097.

[16] S. Tusun, I. Erceg, M. Mehmedović, and D. Sumina, "Decentralized synergetic power system stabilizer", *Elect. Eng.*, pp. 1–10, Jan. 2017. [online]. Available:

http://link.springer.com.proxy.lib.chalmers.se/article/10.1007%2Fs00202-016-0506-y.

[17]   I. Erceg, D. Sumina, S. Tusun, and M. Kutija, "Power system stabilizer based on pointwise min-norm control law", *Elect. Power Syst. Res.*, vol. 143, pp. 215–224, Feb. 2017. [online]. Available: http://www.sciencedirect.com.proxy.lib.chalmers.se/science/article/pii/S0378779616304114.

[18]   Z. Sun, N. Wang, D. Srinivasan, and Y. Bi, "Optimal tunning of type-2 fuzzy logic power system stabilizer based on differential evolution algorithm", *Int. J. Elect. Power Energy Syst.*, vol. 62, pp. 19–28, Nov. 2014. [online]. Available: http://www.sciencedirect.com.proxy.lib.chalmers.se/science/article/pii/S0142061514002063.

[19]   M. Farahani and S. Ganjefar, "Intelligent power system stabilizer design using adaptive fuzzy sliding mode controller", *Neurocomputing*, vol. 226, pp. 135–144, Feb. 2017. [online]. Available: http://www.sciencedirect.com.proxy.lib.chalmers.se/science/article/pii/S092523121631445X.

[20]   A. Andreoiu, K. Bhattacharya, and C. Canizares, "Pricing power system stabilisers using game theory", *IEEE Proc. Generation, Transmission Distribution*, vol. 152, no. 6, pp. 780–786, Nov. 2005. [online]. Available: http://ieeexplore.ieee.org.proxy.lib.chalmers.se/stamp/stamp.jsp?tp=&arnumber=1532095.

[21]   G. Hêmin, M. K. Sheikh-El-Eslami, and H. Seifi, "Power system stabilizer services pricing in an electricity market", *Elect. Power Components Syst.*, vol. 43, no. 18, pp. 2050–2058, Nov. 2015. [online]. Available: http://www-tandfonline-com.proxy.lib.chalmers.se/doi/pdf/10.1080/15325008.2015.1072860?needAccess=true.

[22]   G. J. W. Dudgeon, W. E. Leithead, A. Dyśko, J. O'Reilly, and J. R. McDonald, "The effective role of AVR and PSS in power systems: Frequency response analysis", *IEEE Trans. Power Syst.*, vol. 22, no. 2, pp. 1986–1994, Nov. 2007. [online]. Available: http://ieeexplore.ieee.org.proxy.lib.chalmers.se/document/4349073.

[23]   F. P. deMello and C. Concordia, "Concepts of synchronous machine stability as affected by excitation control", *AIEEE Trans. Power App. Syst.*, vol. PAS-88, no. 4, pp. 692–697, Apr. 1969. [online]. Available: http://ieeexplore.ieee.org.proxy.lib.chalmers.se/document/4073838/.

[24]   K. Bhattacharya, J. Nanda, and M. L. Kothari, "Optimization and performance analysis of conventional power system stabilizers", *Int. J. Elect. Power Energy Syst.*, vol. 19, no. 7, pp. 449–458, May 1997. [online]. Available: http://ac.els-cdn.com.proxy.lib.chalmers.se/S014206159700015X/1-s2.0-S0142061597000

15X-main.pdf?-tid=d693492e-f5f9-11e6-aad1-00000aab0f02&acdnat=14874365
87-8f5b933f6cb8435a4b2bb5907296afd.

[25] P. Kundur, *Power System Stability and Control*. Palo Alto, CA, USA: McGraw-Hill Professional, 1994.

[26] J. Machowski, J. W. Bialek, and J. R. Bumby, *Power System Dynamics: Stability and Control*, 2nd ed. Chichester, United Kingdom: John Wiley & Sons, Ltd., 2008. [online]. Available: http://library.books24x7.com.proxy.lib.chalmers.se/toc.aspx?site=Y7V97&bookid=36428.

[27] A. Hammer, "Analysis of IEEE power system stabilizer models", Master's thesis, Dept. Elect. Power Eng, Norwegian Univ. Sci. Technol., Trondheim, Norway, 2011. [online]. Available: https://daim.idi.ntnu.no/masteroppgaver/006/6022/masteroppgave.pdf.

[28] IEEE Guide for Identification, Testing and Evaluation of the Dynamic Performance Excitation Control Systems, IEEE Standard 421.2, 2014. [online]. Available: http://ieeexplore.ieee.org.proxy.lib.chalmers.se/servlet/opac?punumber=6889137.

[29] J. Paserba, J. Sanchez-Gasca, L. Wang, P. Kundur, E. Larsen, and C. Concordia, "Small-signal stability and power system oscillations", in *Power System Stability and Control*, L. L. Grigsby, Ed., Oxfordshire, United Kingdom: Taylor & Francis, 2012, pp. 10:1–10:24. [online]. Available: http://www.crcnetbase.com.proxy.lib.chalmers.se/isbn/9781439883211.

[30] M. J. Gibbard, P. Pourbeik, and D. J. Vowles, *Small-signal stability, control and dynamic performance of power systems*. Adelaide, Australia: University of Adelaide Press, 2015. [online]. Available: https://www.adelaide.edu.au/press/titles/small-signal/.

[31] P. Kundur, M.Klein, G. J. Rogers, and M. S. Zywno, "Application of power system stabilizers for enhancement of overall system stability", *IEEE Trans. Power Syst.*, vol. 4, no. 2, pp. 614–626, Apr. 1989. [online]. Available: http://ieeexplore.ieee.org.proxy.lib.chalmers.se/stamp/stamp.jsp?arnumber=193836.

[32] P. Kundur, "Power system stability", in *Power System Stability and Control*, L. L. Grigsby, Ed., Oxfordshire, United Kingdom: Taylor & Francis, 2012, pp. 8:1–8:12. [online]. Available: http://www.crcnetbase.com.proxy.lib.chalmers.se/isbn/9781439883211.

[33] S. Fetissi, D. Labed, and I. Labed, "The transient stability study of a synchronous generator based on the rotor angle stability", *Int. J. Elect. Comput. Eng.*, vol. 5, no. 6, pp. 1319–1327, Dec. 2015. [online]. Available: http://search.

proquest.com.proxy.lib.chalmers.se/docview/1732585414?pq-origsite=
summon.

[34] D. Mondal, A. Chakrabarti, and A. Sengupta, *Power System Small Signal Stability Analysis and Control*, 1st ed. Amsterdam, The Netherlands: Elsevier/AP, 2014. [online]. Available: http://www.sciencedirect.com.proxy.lib.chalmers.se/science/book/9780128005729.

[35] M. Eremia, M. Shahidehpour, and A. Berizzi, *Handbook of electrical power system dynamics: Modeling, stability, and control.* Piscataway, NJ, USA: Wiley-IEEE Press, 2013. [online]. Available: http://ieeexplore.ieee.org.proxy.lib.chalmers.se/xpl/bkabstractplus.jsp?bkn=6480471.

[36] V. E. Larsen and D. A. Swann, "Applying power system stabilizers. Part i: General concepts", *IEEE Power Eng. Rev.*, vol. PER-1, no. 6, pp. 62–63, Jun. 1981. [online]. Available: http://ieeexplore.ieee.org.proxy.lib.chalmers.se/stamp/stamp.jsp?arnumber=5511615.

[37] P. Jagadeesh and M. S. Veerraju, "Dynamic stability and analysis of SMIB system with power system stabilizers using different techniques", *I-Manager's J. Power Syst. Eng.*, vol. 3, no. 2, pp. 8–15, May 2015. [online]. Available: http://search.proquest.com.proxy.lib.chalmers.se/docview/1761089862?pq-origsite=summon.

[38] IEEE Recommended Practice for Excitation System Models for Power System Stability Studies, IEEE Standard 421.5, 2005. [online]. Available: https://standards.ieee.org/findstds/standard/421.5-2016.html.

[39] M. A. Hassouneh, L. Hsien-Chiarn, and E. H. Abed, "Washout filters in feedback control: Benefits, limitations and extensions", *In Proc. 2004 Amer. Control Conf.*, pp. 3950–3955, [online]. Available: http://ieeexplore.ieee.org.proxy.lib.chalmers.se/document/1383925/.

[40] E. Cheever, "Rules for Drawing Bode Diagrams," Swarthmore College, 2015. [online]. Available: http://lpsa.swarthmore.edu/Bode/BodeReviewRules.html.

[41] R. C. Dorf and J. A. Svoboda, *Introduction to Electric Circuits*, 8th ed. Chichester, United Kingdom: John Wiley & Sons, Ltd., 2011.

[42] F. Yahyaie, S. Arabi, and Z. Feng, "Effects of the ramp-tracking filter on overall compensation of power system stabilizers", *In 2016 IEEE Int. Conf. Power Syst. Technol. (POWERCON)*, pp. 1–6, [online]. Available: http://ieeexplore.ieee.org.proxy.lib.chalmers.se/stamp/stamp.jsp?arnumber=7754016.

[43] J. Morsali, R. Kazemzadeh, M. R. Azizian, and A. Parhizkar, "Introducing PID-based PSS2B stabilizer in coordination with TCSC damping controller to

improve power system dynamic stability", *In 2014 22nd Iranian Conf. Elect. Eng. (ICEE)*, pp. 836–841, [online]. Available: http://ieeexplore.ieee.org.proxy.lib.chalmers.se/document/6999652/.

[44] I. Kamwa, R. Grondin, and G. Trudel, "IEEE PSS2B versus PSS4B: The limits of performance of modern power system stabilizers", *IEEE Trans. Power Syst.*, vol. 20, no. 2, pp. 903–915, May 2005. [online]. Available: http://ieeexplore.ieee.org.proxy.lib.chalmers.se/stamp/stamp.jsp?arnumber=1425588.

[45] W. G. Heffron and R. A. Philips, "Effects of modern amplidyne voltage regulator in underexcited operation of large turbine generators", *AIEEE Trans. Power App. Syst.*, vol. PAS-71, no. 1, pp. 692–697, Aug. 1952. [online]. Available: http://ieeexplore.ieee.org.proxy.lib.chalmers.se/document/4498530/.

[46] Simpow User's Manual, 11th ed., STRI, 2008.

[47] D. Peppas, "Development and analysis of nordic32 power system model in powerfactory", Master's thesis, School Elect. Eng., Royal Inst. Technol., Stockholm, Sweden, 2008. [online]. Available: http://www.diva-portal.org/smash/get/diva2:609184/FULLTEXT01.pdf.

Appendix A

Values of the Parameters of the Linearized Model of Single-Machine Infinite Bus System

Table A.1 presents the values of the parameters of the SMIB-system in Figure 3.1.

Table A.1: Values of the parameters of the SMIB-system

Description	Parameter	Value	Unit
Amplitude of infinite bus voltage	$|\underline{E_B}|$	0.995	p.u.
Phase of infinite bus voltage	θ_B	0	rad
Amplitude of terminal voltage	$|\underline{V_t}|$	1	p.u.
Phase of terminal voltage	θ_t	0.471	rad
Line reactance	X_E	0.65	p.u.
Amplitude of internal voltage	$|E_f'|$	1.0759	p.u.
Phase of internal voltage	$\underline{\delta_t}$	0.673	rad
Amplitude of line current	$|\underline{I}|$	0.7165	p.u.
Phase of line current	ϕ	-0.246	rad
Active power	P_e	0.695	p.u.
Reactive power	Q_e	0.1745	p.u.

Table A.2 presents the values of the parameters of the transient SM-model.

Table A.2: Values of the parameters of the transient SM-model

Description	Parameter	Value	Unit
Rated rotor angular frequency	ω_0	314.16	electrical rad/s
Inertia constant	H	2.6000	$(\text{MW} \cdot \text{s})/\text{MVA}$
d-axis synchronous reactance	X_d	1.15	p.u.
q-axis synchronous reactance	X_q	1	p.u.
d-axis transient reactance	X_d'	0.31	p.u.
Leakage reactance	X_l	0.19	p.u.
Armature resistance	R_a	0.003	p.u.
d-axis open circuit transient time constant	T_{d0}'	8	s

Note: Per unit reactance values are equal to per unit inductance values.

Values of the Parameters of the Dynamic Models of Power Systems

The first section presents the values of the parameters of the dynamic model of the SMIB-system. The second section presents the values of the parameters of the dynamic model of the multi-bus power system.

Values of the Parameters of Single-Machine Infinite Bus System

Table A.3 presents parameter values of the SMIB-system defined in Section 4.1.

Table A.3: Values of the parameters of the SMIB-system

Values of the Base Parameters			
Description	**Parameter**	**Value**	**Unit**
Base power	S_B	120	MVA
Base frequency	f_B	50	Hz
Bus 1 base voltage	V_{B1}	10	kV
Bus 2 base voltage	V_{B2}	130	kV
Bus 3 base voltage	V_{B3}	130	kV
Values of the Parameters of the Power System			
Parameter	**Symbol**	**Value**	**Unit**
SM active power	P_e	100	MW
Bus 1 nominal voltage*	V_{N1}	10	kV
Bus 2 nominal voltage**	V_{N2}	130	kV
Bus 3 nominal voltage	V_{N3}	130	kV
Transformer short-circuit reactance	X_k	0.1	p.u.
Load active power	P_L	80	MW
Line resistance	R_L	0.0001	p.u./km
Line reactance	X_L	0.01	p.u./km
Line length	l	60	km
Short-circuit resistance	R_B	0.224	Ω
Short-circuit reactance	X_B	2.24	Ω
Infinite bus voltage	E_B	1	p.u.
Angle of infinite bus voltage	θ_B	0	rad

Notes: *Equal to nominal voltage of the SM and equal to the nominal voltage of the low-voltage side of the transformer. **Equal to the nominal voltage of the high-voltage side of the transformer.

Table A.4 presents the values of the parameters of the dynamic model of the SM.

Table A.4: Values of the parameters of the dynamic model of the SM

Description	Parameter	Value	Unit
Inertia constant	H	2.6	$(\text{MW} \cdot \text{s})/\text{MVA}$
d-axis synchronous reactance	X_d	1.15	p.u.
q-axis synchronous reactance	X_q	1	p.u.
d-axis transient reactance	X_d'	0.31	p.u.
q-axis transient reactance	X_q'	0.83	p.u.
d-axis subtransient reactance	X_d''	0.23	p.u.
q-axis subtransient reactance	X_q''	0.23	p.u.
Leakage reactance	X_l	0.19	p.u.
Armature resistance	R_a	0.003	p.u.
d-axis open-circuit transient time constant	T_{d0}'	8	s
q-axis open-circuit transient time constant	T_{q0}'	2	s
d-axis open-circuit transient time constant	T_{d0}''	0.05	s
q-axis open-circuit transient time constant	T_{q0}''	0.2	s

Tables A.5 and A.6 presents the values of the parameters of the turbine and governor models, respectively.

Table A.5: Values of the parameters of the turbine model

Description	Parameter	Value	Unit
Engine dead time	T_{T1}	0.1	s
Fuel valve time constant	T_{T2}	0.1	s

Table A.6: Values of the parameters of the governor model

Description	Parameter	Value	Unit
Governor gain	K_G	10	p.u./p.u.
Equivalent time constant	T_{G1}	0.1	s

Values of the Parameters of Multi-Bus Power System

Tables A.7 and A.8 give the values of the parameters of the PSS2Bs when the PSS2B is tuned according to tunings A and B. The tables show the values of the parameters of the PSS2B for tuning of the PSS2Bs according to both the FIKS- and the NG-methods.

Table A.7: Values of the parameters of the PSS2Bs when PSS2Bs are tuned with tuning A

FIKS-Method			NG-Method		
Parameter	Value	Unit	Parameter	Value	Unit
K_{S1}	7	p.u./p.u.	K_{S1}	9	p.u./p.u.
$T_{W1} - T_{W4}$	5	s	$T_{W1} - T_{W4}$	8	s
T_1	0.29	s	T_1	0.1	s
T_2	0.09	s	T_2	0.02	s
T_3	0.27	s	T_3	0.1	s
T_4	0.09	s	T_4	0.02	s
T_{10}	1	s	T_{10}	0.12	s
T_{11}	1	s	T_{11}	0.02	s

Table A.8: Values of the parameters of the PSS2Bs when PSS2Bs are tuned with tuning B

FIKS-Method			NG-Method		
Parameter	Value	Unit	Parameter	Value	Unit
K_{S1}	9	p.u./p.u.	K_{S1}	10.3	p.u./p.u.
$T_{W1} - T_{W4}$	7	s	$T_{W1} - T_{W4}$	7	s
T_1	0.08	s	T_1	0.1	s
T_2	0.05	s	T_2	0.035	s
T_3	0.22	s	T_3	0.1	s
T_4	0.1	s	T_4	0.01	s
T_{10}	0.22	s	T_{10}	0.15	s
T_{11}	0.1	s	T_{11}	0.02	s

Appendix B

Calculating K_1, K_2, K_3, K_4, K_5, K_6, and T_{fd}

It is assumed that the effect of magnetic saturation is neglected. Hence, K_{sd} and K_{sq} are put to one. The values of the following parameters are then calculated [25]:

$$L_{adu} = L_d - L_l \tag{B.1}$$

$$L_{aqu} = L_q - L_l \tag{B.2}$$

$$L_{ads} = K_{sd} L_{adu} \tag{B.3}$$

$$L_{aqs} = K_{sq} L_{aqu} \tag{B.4}$$

$$X_{ds} = K_{sd} L_{adu} + L_l \tag{B.5}$$

$$X_{qs} = K_{sq} L_{aqu} + L_l \tag{B.6}$$

$$L_{ds} = K_{sd} L_{adu} + L_l \tag{B.7}$$

$$L_{qs} = K_{sq} L_{aqu} + L_l \tag{B.8}$$

$$L_{fd} = \frac{L_{adu}(L_d' - L_l)}{L_{adu} + L_l - L_d'} \tag{B.9}$$

$$R_{fd} = \frac{L_{adu} + L_{fd}}{\omega_0 T_{d0}'} \tag{B.10}$$

$$\delta_i = \tan^{-1}\left(\frac{|\underline{I}|X_{qs}\cos\phi - |\underline{I}|R_a\sin\phi}{|\underline{E_t}| + |\underline{I}|R_a\cos\phi + |\underline{I}|X_{qs}\sin\phi}\right). \tag{B.11}$$

Expressing the terminal voltage of the SM, the infinite bus voltage, and the line current in the same rotating reference frame by the following equations [25]:

$$e_{d0} = |\underline{E_t}|\sin\delta_i \tag{B.12}$$

$$e_{q0} = |\underline{E_t}|\cos\delta_i \tag{B.13}$$

$$i_{d0} = |\underline{I}|\sin(\delta_i + \phi) \tag{B.14}$$

$$i_{q0} = |\underline{I}|\cos(\delta_i + \phi) \tag{B.15}$$

$$E_{Bd0} = e_{d0} - R_E i_{d0} + X_E i_{q0} \tag{B.16}$$

$$E_{Bq0} = e_{q0} - R_E i_{q0} - X_E i_{d0} \tag{B.17}$$

$$E_B = (E_{Bd0}^2 + E_{Bq0}^2)^{1/2} \tag{B.18}$$

$$\delta_0 = \tan^{-1}\left(\frac{E_{Bd0}}{E_{Bq0}}\right). \tag{B.19}$$

This allows for the calculation of the following parameters [25]:

$$i_{fd0} = \frac{e_{q0} + R_a i_{q0} + L_{ds} i_{d0}}{L_{ads}} \tag{B.20}$$

$$E_{fd0} = L_{adu} i_{fd0} \tag{B.21}$$

$$L'_{ads} = \frac{1}{\frac{1}{L_{ads}} + \frac{1}{L_{fd}}} \tag{B.22}$$

$$\Psi_{ad0} = L_{ads}(-i_{d0} + i_{fd0}) \tag{B.23}$$

$$\Psi_{aq0} = -L_{aqs} i_{iq0} \tag{B.24}$$

$$R_T = R_a + R_E \tag{B.25}$$

$$X_{Td} = X_E + L'_{ads} + L_l \tag{B.26}$$

$$X_{Tq} = X_E + L_{aqs} + L_l \tag{B.27}$$

$$D = R_T^2 + X_{Td} X_{Tq}. \tag{B.28}$$

After calculating the values of the parameters given by (B.1) - (B.28), the coefficients K_1 - K_4 are calculated by the following equations [25]:

$$K_1 = n_1(\Psi_{ad0} + L_{aqs} i_{d0}) - m_1(\Psi_{aq0} + L'_{ads} i_{q0}) \tag{B.29}$$

$$K_2 = n_2(\Psi_{ad0} + L_{aqs} i_{d0}) - m_2(\Psi_{aq0} + L'_{ads} i_{q0}) + \frac{L'_{ads}}{L_{fd}} i_{q0} \tag{B.30}$$

$$K_3 = \frac{L_{fd}^2}{L_{adu}(L_{fd} - L'_{ads} + m_2 L_{fd} L'_{ads})} \tag{B.31}$$

$$K_4 = \frac{m_1 L'_{ads} L_{adu}}{L_{fd}} \tag{B.32}$$

where m_1, m_2, n_1 and n_2 are equal to [25]:

$$m_1 = \frac{E_B(X_{Tq} \sin \delta_0 - R_T \cos \delta_0)}{D} \tag{B.33}$$

$$m_2 = \frac{X_{Tq}}{D} \frac{L_{ads}}{L_{ads} + L_{fd}} \tag{B.34}$$

$$n_1 = \frac{E_B(R_T \sin \delta_0 + X_{Td} \cos \delta_0)}{D} \tag{B.35}$$

$$n_2 = \frac{R_T}{D} \frac{L_{ads}}{L_{ads} + L_{fd}}. \tag{B.36}$$

The field circuit time constant is [25]

$$T_{fd} = \frac{L_{fd}^2}{\omega_0 R_{fd}(L_{fd} - L'_{ads} + m_2 L_{fd} L'_{ads})}. \tag{B.37}$$

The coefficients K_5 and K_6 are calculated by [25]:

VI

$$K_5 = \frac{e_{d0}}{|\underline{E_t}|}(-R_a m_1 + L_l n_1 + L_{aqs} n_1) + \frac{e_{q0}}{|\underline{E_t}|}(-R_a n_1 - L_l m_1 - L'_{ads} m_1) \quad \text{(B.38)}$$

$$K_6 = \frac{e_{d0}}{|\underline{E_t}|}(-R_a m_2 + L_l n_2 L_{aqs} n_2) + \frac{e_{q0}}{|\underline{E_t}|}\Big(-R_a n_2 - L_l m_2$$
$$+ L'_{ads}\big(\frac{1}{L_{fd}} - m_2\big)\Big). \quad \text{(B.39)}$$

Calculating $a_1, \ldots, a_5$ and $b_1, \ldots, b_6$

With $\Delta\Psi_{fd} = P(s)\Delta\delta_t$, it is possible to express (3.9) as follows:
$$\Delta T_e = K_1 \Delta\delta_t + K_2 P(s)\Delta\delta_t. \quad \text{(B.40)}$$
The equation for $P(s)$ is found after rewriting (3.18) and by inserting the equation of the transfer function of the brushless exciter and AVR that is given by (3.17); consequently, $P(s)$ can be written as:

$$P(s) = \frac{-K_3\left[K_4(1 + T_R s) + K_5\left(\frac{K_P K_d T_i T_d s^2 + (K_P K_d T_i + K_P K_d T_d)s + K_P K_d}{T_d T_{bex} T_i s^3 + (K_d T_{bex} T_i + T_i T_d)s^2 + K_d T_i s}\right)\right]}{T_R T_{fd} s^2 + (T_R + T_{fd})s + 1 + K_3 K_6\left(\frac{K_P K_d T_i T_d s^2 + (K_P K_d T_i + K_P K_d T_d)s + K_P K_d}{T_d T_{bex} T_i s^3 + (K_d T_{bex} T_i + T_i T_d)s^2 + K_d T_i s}\right)}\Delta\delta_t. \quad \text{(B.41)}$$

Reduction of the algebraic equation in (B.41) yields an equation for $P(s)$ that is on the form
$$P(s) = \frac{a_1 s^4 + a_2 s^3 + a_3 s^2 + a_4 s + a_5}{b_1 s^5 + b_2 s^4 + b_3 s^3 + b_4 s^2 + b_5 s + b_6}\Delta\delta_t \quad \text{(B.42)}$$
where the coefficients $a_1, \ldots, a_5$ and $b_1, \ldots, b_6$ are given by

$$a_1 = -K_3 K_4 T_R T_d T_{bex} T_i \quad \text{(B.43)}$$
$$a_2 = -K_3(K_4 T_d T_{bex} T_i + K_d T_{bex} T_i T_R + T_i T_d T_R) \quad \text{(B.44)}$$
$$a_3 = -K_3(K_4 K_d T_{bex} T_i + K_4 T_i T_d + K_d T_i T_R + K_5 K_P T_i T_d) \quad \text{(B.45)}$$
$$a_4 = -K_3(K_4 K_d T_i + K_5 K_P T_i K_d + K_5 K_P T_d) \quad \text{(B.46)}$$
$$a_5 = -K_3 K_5 K_P K_d \quad \text{(B.47)}$$
$$b_1 = T_R T_{fd} T_d T_{bex} T_i \quad \text{(B.48)}$$
$$b_2 = T_R T_{fd} K_d T_{bex} T_i + T_R T_{fd} T_i T_d + T_{fd} T_d T_{bex} T_i + T_R T_d T_{bex} T_i \quad \text{(B.49)}$$
$$b_3 = T_R T_{fd} K_d T_i + T_{fd} K_d T_{bex} T_i + T_i T_{fd} T_d + T_R K_d T_{bex} T_i$$
$$\quad + T_R T_{bex} T_d + T_d T_{bex} T_i \quad \text{(B.50)}$$
$$b_4 = T_{fd} K_d T_i + T_R K_d T_i + K_d T_{bex} T_i + T_i T_d + K_3 K_6 K_P T_i K_d T_d \quad \text{(B.51)}$$
$$b_5 = K_d T_i + K_3 K_6 K_P K_d T_i + K_3 K_6 K_P K_d T_d \quad \text{(B.52)}$$
$$b_6 = K_3 K_6 K_d K_P. \quad \text{(B.53)}$$
$$\quad \text{(B.54)}$$

VIII

Appendix C

Varying Time Constants of the Lead-Lag Filters

Table C.1 presents the values of the time constants of the lead-lag filters used when obtaining the result in Fig. 5.10.

Table C.1: Values of the time constants of the lead-lag filters

	T_1	T_2	T_3	T_4	T_{10}	T_{11}
$r_0 = 2.941$	0.1	0.034	0.15	0.051	0.15	0.051
$r = 5$	0.1	0.02	0.15	0.03	0.15	0.03
$r = 2$	0.1	0.05	0.15	0.075	0.15	0.075

Table C.2 presents the values of the time constants of the lead-lag filters used when obtaining the result in Fig. 5.12.

Table C.2: Values of the time constants of the lead-lag filters

	T_1	T_2	T_3	T_4	T_{10}	T_{11}
$r_0 = 2.941$	0.1	0.034	0.15	0.051	0.15	0.051
$r = 2.941$	0.2	0.068	0.3	0.102	0.3	0.102
$r = 5$	0.2	0.04	0.3	0.06	0.3	0.06
$r = 2$	0.2	0.1	0.3	0.15	0.3	0.15

Table C.3 presents the values of the time constants of the lead-lag filters used when obtaining the result in Fig. 5.14.

Table C.3: Values of the time constants of the lead-lag filters

	T_1	T_2	T_3	T_4	T_{10}	T_{11}
$r_0 = 2.941$	0.1	0.034	0.15	0.051	0.15	0.051
$r = 2.941$	0.05	0.017	0.075	0.0255	0.075	0.0255
$r = 5$	0.05	0.01	0.075	0.015	0.075	0.015
$r = 2$	0.05	0.025	0.075	0.0375	0.0375	0.075

Table C.4 presents the values of the time constants of the lead-lag filters used when obtaining the result in Fig. 5.15.

Table C.4: Values of the time constants of the lead-lag filters

	T_1	T_2	T_3	T_4	T_{10}	T_{11}
$r_0 = 2.941$	0.1	0.034	0.15	0.051	0.15	0.051
$r = 2.941$	0.05	0.017	0.15	0.051	0.3	0.102
$r = 5$	0.05	0.01	0.15	0.03	0.3	0.06
$r = 2$	0.05	0.025	0.15	0.075	0.3	0.15

Table C.5 presents the values of the time constants of the lead-lag filters used when obtaining the result in Fig. 5.16.

Table C.5: Values of the time constants of the lead-lag filters

	T_1	T_2	T_3	T_4	T_{10}	T_{11}
$r_{3,0} = 2.941$	0.1	0.034	0.15	0.051	0.15	0.051
$r_3 = 2.941$	0.05	0.017	0.15	0.051	0.3	0.102
$r_3 = 5$	0.05	0.017	0.15	0.051	0.3	0.06
$r_3 = 2$	0.05	0.017	0.15	0.051	0.3	0.15

Relations Between Responses of FIKS- and NG-Methods

Table C.6 gives the values of the parameters of the simplified PSS2B that are used when obtaining the results in Fig. 5.17.

Table C.6: Values of the parameters of the simplified PSS2B

	K_{S1}	T_{W1}	T_{W2}	T_1	T_2	T_3	T_4	T_{10}	T_{11}
Solid	10	7	7	0.1	0.034	0.15	0.051	0.15	0.051
Dashed	30	12	12	0.17	2	0.4	0.06	0.4	0.08
Blue dotted	19.5	12	12	0.17	2	0.4	0.06	0.4	0.08

Table C.7 gives the values of the parameters of the simplified PSS2B that are used when obtaining the results in Fig. 5.18.

Table C.7: Values of the parameters of the simplified PSS2B

	K_{S1}	T_{W1}	T_{W2}	T_1	T_2	T_3	T_4	T_{10}	T_{11}
Solid	10	7	7	0.1	0.034	0.15	0.051	0.15	0.051
Dashed	6.3	7	7	0.1	0.025	0.15	0.035	0.3	0.04
Blue dotted	4	7	7	0.1	0.025	0.15	0.035	0.3	0.04
Green dash-dotted	9	7	7	0.1	0.025	0.15	0.035	0.3	0.04

Table C.8 gives the values of the parameters of the PSS2B that are used when obtaining the results in Fig. 6.4.

Table C.8: Values of the parameters of the PSS2B

	K_{S1}	T_{W1}	T_{W2}	T_1	T_2	T_3	T_4	T_{10}	T_{11}
Solid	8	7	7	0.08	0.05	0.22	0.075	0.22	0.075
Dashed	35	14	14	0.1	2	0.4	0.063	0.4	0.063
Blue dotted	21	14	14	0.1	2	0.4	0.063	0.4	0.063

Table C.9 gives the values of the parameters of the PSS2B that are used when obtaining the results in Fig. 6.5.

Table C.9: Values of the parameters of the PSS2B

	K_{S1}	T_{W1}	T_{W2}	T_1	T_2	T_3	T_4	T_{10}	T_{11}
Solid	8	7	7	0.08	0.05	0.22	0.075	0.22	0.075
Dashed	5.5	7	7	0.05	0.031	0.2	0.07	0.35	0.05
Blue dotted	3.7	7	7	0.05	0.031	0.2	0.07	0.35	0.05
Green dash-dotted	8	7	7	0.05	0.031	0.2	0.07	0.35	0.05

Table C.10 gives the values of the parameters of the PSS2B that are used when obtaining the results in Fig. 6.6.

Table C.10: Values of the parameters of the PSS2B

	K_{S1}	T_{W1}	T_{W2}	T_1	T_2	T_3	T_4	T_{10}	T_{11}
Solid	8	7	7	0.08	0.05	0.22	0.075	0.22	0.075
Dashed	5.5	7	7	0.12	0.01	0.2	0.1	0.35	0.05
Blue dotted	3.7	7	7	0.12	0.01	0.2	0.1	0.35	0.05
Green dash-dotted	8	7	7	0.12	0.01	0.2	0.1	0.35	0.05